

## Water interactions with complex surfaces

Présentée le 10 juin 2020

à la Faculté des sciences et techniques de l'ingénieur  
Laboratoire des nanomatériaux supramoléculaires et interfaces - Chaire Constellium  
Programme doctoral en science et génie des matériaux

pour l'obtention du grade de Docteur ès Sciences

par

**Anna MURELLO**

Acceptée sur proposition du jury

Prof. K. Scrivener, présidente du jury  
Prof. F. Stellacci, directeur de thèse  
Prof. E. Dufresne, rapporteur  
Prof. S. Shimizu, rapporteur  
Prof. A. Radenovic, rapporteuse



# Acknowledgements

This thesis talks about surfaces: the visible part of every material, the part that is exposed to the interactions with the rest of the world. I believe the PhD thesis is “the surface” of the PhD. It is what is accessible to the rest of the world, what can be evaluated and judged. However, every surface hides a bulk and a PhD experience is much more than what is written in the thesis. The “bulk” of the PhD is composed of long discussions, even longer experiments, great challenges, unexpected excitements and supportive colleagues.

First of all, I would like to thank Francesco for giving me the opportunity to live this exciting experience and for pushing me to move out of my “comfort zone” and approach a variety of different topics. In Francesco’s attitude, I have always perceived trust in my capabilities and ideas. This trust has been crucial to keep my motivation high and fuel my commitment to different projects. Furthermore, I enjoyed the discussions I had with Francesco about my future career and I am particularly grateful for the way in which Francesco has supported my personal development.

Nothing of what has been presented in this thesis could be achieved without the support of the whole SuNMIL. I believe experimental work strongly benefits from interactions with colleagues: I thank the group for all the time we have spent together looking at data, troubleshooting, discussing possible experiments, looking for technical solutions... but also for all the time we spent together while having a coffee or chatting over lunch. I have enjoyed the cultural mixture of SuNMIL and I have learnt so much from the other members of the group.

The results presented in this thesis have been achieved in strong collaboration with many colleagues from several institutions: a big thanks goes to Dr. Zhi Luo. He was my guide at the beginning of my PhD: he thought me how to stay focused on results, how to follow inspiration, how to deal with collaborators and so on. His advice has been very precious. All the data presented in Chapter 6 have been collected working side by side with him and also the project presented in Chapter 7 took inspiration from his preliminary data.

I am also deeply grateful to Dr. David Wilkins: his modeling work allowed us to unravel some of the mysteries of wetting at the nanoscale (Chapter 6). His patience and calm are impressive and were of great help when we were struggling to interpret our data.

A lot of other people was of great technical help for the measurements and the interpretation of results presented in Chapter 6: Filip Kovacik, Dr. Halil Okur, Dr. Nikolay Smolentsev, Dr. Nikolaos Nianias, Dr. Quy Ong, Prof. Sylvie Roke and Prof. Michele Ceriotti.

The expertise of Dr. Yang Ye in the synthesis of gold nanoparticles and in the collection and interpretation of SAXS data has been instrumental for the development of Chapter 7. The measurements described in this chapter were performed with the precious help of Ting Mao, Zexiang Brady Han, Dr. Nicolò Razza and Dr. Sandor Balog. I acknowledge all of them for sharing their thoughts and expertise with me.

A special thanks goes to all the bachelor and master students I am being working with during my PhD. I have really appreciated the time I spent with them in the lab and their questions helped me a lot in understanding my own projects.

Finally, let me thank a special collaborator, with whom discussions used to continue over dinner. He has followed my progress from a very particular perspective, caring for my results both professionally and personally. The fact that a PhD is a stressful time is a very well-known phenomenon and ups are often followed by downs. My downs have been sometimes very deep and I have managed to climb out of them only because of Antimo’s support. His tenderness and love made this PhD happen.





# Abstract

The solvent accessible surface area of proteins is very complex, mainly because it is composed of domains with different degrees of affinity for water. The domains nature and arrangement determine both the interactions of the proteins with water (and therefore the water structure around the protein) as well as the interactions with other particles in suspension (other proteins or other macromolecules). Both these interactions are fundamental to determine the functionality of the proteins. To date, a theoretical model able to predict the wetting properties of proteins has yet to be developed.

The goal of this thesis is to improve our understanding of the wetting properties of this kind of complex surfaces. In order to simplify the interpretation of the results a model system has been used: gold nanoparticles protected by a shell composed of a binary mixture of hydrophobic/hydrophilic ligands. These nanoparticles resemble proteins because of their overall size as well as the size of the hydrophilic and hydrophobic domains exposed on their surface. The advantages of working with nanoparticles include the fact that they are stable over a larger range of conditions and that the properties of the ligand shell can be designed and tuned depending on the research question.

In this thesis we show that the arrangement of the hydrophobic and hydrophilic domains is responsible for the interaction between the particles and the surrounding solvent (especially water). Indeed, we show that both the water structure and interfacial energy vary significantly between identical particles that differ only in the domain arrangement. A new predictive model is proposed. This model considers, for every molecule in the ligand shell, the contributions of its first-nearest neighbors as a descriptor to determine the wetting properties of the surface. The experiments and theoretical model proposed here provide a starting point to develop a comprehensive understanding of complex interfaces as well as for the engineering of synthetic ones.

The interparticle interactions in water are also been characterized. It is shown that there exists the possibility to screen hydrophobic attraction by adding small molecules to the suspension. This stabilization technique seems to be relevant to maintain the stability of biological fluids. An example of the application of this stabilization technique to food science is also presented here.

In addition to these studies, an innovative technique to measure the surface energy at the nanoscale is presented here, based on the measurement of the adhesion force between an atomic force microscopy tip and a sample.

## Keywords

Water structure, wetting properties, hydrophobic interactions, atomic force microscopy, small angle X-rays scattering

# Sommario

L'area superficiale accessibile al solvente è molto complessa nel caso delle proteine, prevalentemente perché composta da domini con diversi gradi di affinità per l'acqua. La natura e l'organizzazione dei domini determinano sia le interazioni delle proteine con l'acqua (e quindi la struttura dell'acqua intorno alle proteine) sia le interazioni con altre particelle in sospensione (siano esse altre proteine o altre macromolecole). Entrambe queste interazioni sono fondamentali per la funzionalità delle proteine. Ad oggi, un modello teorico in grado di predire le proprietà di bagnabilità delle proteine non è ancora stato sviluppato.

Lo scopo di questa tesi è migliorare la comprensione delle proprietà di bagnabilità di questo tipo di superfici complesse. Per semplificare l'interpretazione dei risultati abbiamo utilizzato un sistema modello: nanoparticelle d'oro rivestite da un guscio composto da una miscela binaria di leganti idrofilici ed idrofobici. Queste nanoparticelle assomigliano a proteine per quanto riguarda la loro dimensione e la grandezza dei domini idrofilici ed idrofobici esposti sulla superficie. I vantaggi di lavorare con nanoparticelle includono il fatto che esse sono stabili in una vasta gamma di condizioni e che le proprietà del guscio di leganti possono essere progettate e regolate a seconda dello scopo della ricerca.

In questa tesi mostriamo che l'organizzazione dei domini idrofilici ed idrofobici è determinante per l'interazione tra le particelle e il solvente (in particolare nel caso dell'acqua). Infatti, mostriamo che sia la struttura dell'acqua che l'energia d'interfaccia differiscono significativamente nel caso di due particelle identiche, differenti solo per l'organizzazione dei domini. Proponiamo un nuovo modello predittivo che considera, per ogni molecola nel guscio di leganti, il contributo dei suoi primi vicini come un descrittore per determinare le proprietà di bagnabilità della superficie. Gli esperimenti e il modello teorico qui proposto forniscono un punto di partenza per lo sviluppo di una comprensione globale delle interfacce complesse e per lo sviluppo di interfacce sintetiche.

Inoltre, abbiamo caratterizzato le interazioni tra particelle in acqua. Mostriamo come esista la possibilità di schermare l'attrazione idrofobica aggiungendo piccole molecole alla sospensione. Questa tecnica di stabilizzazione sembra essere rivelante per mantenere la stabilità dei fluidi biologici. In questa tesi, viene anche discusso un esempio di applicazione di questa tecnica di stabilizzazione nell'ambito delle scienze alimentari.

In aggiunta a questi studi, viene presentata una tecnica innovativa per la misura dell'energia d'interfaccia alla nanoscala, basata sulla misura della forza di adesione tra un campione e una punta in un microscopio a forza atomica.

## Parole chiave

Struttura dell'acqua, proprietà di bagnabilità, interazioni idrofobiche, microscopio a forza atomica, *scattering* di raggi X a basso angolo

# Contents

<b>Acknowledgements.....</b>	<b>i</b>
<b>Abstract .....</b>	<b>iii</b>
<b>Keywords .....</b>	<b>iii</b>
<b>Sommario.....</b>	<b>iv</b>
<b>Parole chiave.....</b>	<b>iv</b>
<b>Contents.....</b>	<b>v</b>
<b>List of Figures .....</b>	<b>vii</b>
<b>Chapter 1    Structure of the thesis .....</b>	<b>1</b>
<b>Chapter 2    Introduction .....</b>	<b>3</b>
2.1    Water .....	3
2.1.1    Hydrophobes .....	4
2.1.2    Hydrophiles.....	4
2.2    Surfaces .....	5
2.3    Solid-liquid interfaces.....	6
2.4    Interactions between particles and surfaces in a medium .....	8
2.4.1    Electrical double layer .....	8
2.4.2    DLVO theory.....	9
2.4.3    Solvation forces.....	10
<b>Chapter 3    Introduction to gold nanoparticles .....</b>	<b>13</b>
<b>Chapter 4    Main techniques used .....</b>	<b>17</b>
4.1    Contact angle .....	17
4.2    Atomic force microscopy (AFM) .....	18
4.2.1    Force curves and force maps .....	19
4.2.2    Small amplitude modulation atomic force microscopy (SAM-AFM).....	20
4.2.3    Development of a method to evaluate the tip quality.....	22
4.3    Sum Frequency generation spectroscopy (SFG) .....	25
4.4    Ultraviolet-visible spectroscopy (UV-vis) .....	27
4.5    Small angle x-rays scattering (SAXS) .....	28

4.6	Dynamic light scattering (DLS) .....	30
<b>Chapter 5</b>	<b>Measurements of surface energy through AFM force curves .....</b>	<b>33</b>
5.1	The goal of this project.....	33
5.2	State of the art.....	34
5.3	Proposed approach .....	34
5.4	Protocol .....	35
5.5	Applications and limitations .....	36
<b>Chapter 6</b>	<b>Determination and evaluation of the non-additivity in wetting of molecularly heterogeneous surfaces .....</b>	<b>39</b>
6.1	Cassie equation and its limitations .....	39
6.1.1	Computational studies of water-solid interfaces at the nanoscale .....	39
6.1.2	Experimental studies of water-solid interfaces at the nanoscale.....	41
6.1.3	The goal of this project.....	42
6.2	A model system to study the effects of chemical heterogeneity on interfacial properties	43
6.3	Experimental measurements of the water structure .....	45
6.3.1	Control measurements on additional sets of nanoparticles .....	48
6.4	Computational study of the interfacial properties .....	49
6.5	Development of a new model .....	50
6.6	Conclusions and outlook .....	53
<b>Chapter 7</b>	<b>Understanding and screening hydrophobic interactions .....</b>	<b>55</b>
7.1	Introduction .....	55
7.2	Effect of the addition of small molecules on hydrophobic interactions .....	57
7.2.1	Stabilizing molecules .....	59
7.2.2	Molecules without any effect on the interactions.....	61
7.2.3	Destabilizing molecules .....	62
7.2.4	Mixtures of molecules .....	63
7.3	Examples of applications to food science .....	64
7.4	Conclusions and outlook .....	65
7.5	Materials and methods .....	65
<b>Chapter 8</b>	<b>Conclusions and outlook .....</b>	<b>67</b>
<b>References</b>	<b>.....</b>	<b>69</b>
<b>List of publications</b>	<b>.....</b>	<b>82</b>
<b>Curriculum Vitae</b>	<b>.....</b>	<b>83</b>

## List of Figures

- Figure 1 **Radial distribution functions** Typical RDF for simple fluids: (a) hard spheres, (b) Lennard-Jones potential. (c) Partial RDFs for water at 298 K. Adapted from references 2 and 11, with permission. .... 3
- Figure 2 **Liquid density profiles at interfaces.** (a) Vapor-liquid interface.  $\rho_{\infty}$  is the bulk liquid density and  $\lambda_0$  is the width of the interface. (b) Liquid density profile at an isolated solid-liquid interface.  $\rho_s(\infty)$  is the “contact” density at the surface. (c) Three-dimensional atomic force microscopy visualization of the first hydration layers at the water-mica interface. (a, b) are reproduced from reference 12, with permission, (c) is reproduced from reference 23, with permission. .... 6
- Figure 3 **Schematic representation of the water ordering in the first hydration layer of a solid-liquid interface.** In the case of a negatively charged surface (hydrophilic) the water molecules are forced to orient with one of the two  $H^+$  pointing toward the surface. This severely restricts the way the first layer of water molecules can orient. On the contrary, on a hydrophobic surface, the molecules reorient in order to minimize the number of H-bonds lost, without any restriction on the charge pointing toward the surface. Adapted from reference 12, with permission. .... 6
- Figure 4 **Contact angle:** it is the angle formed by a drop on the surface, at the triple line (where the liquid, the solid and the vapour meet). .... 8
- Figure 5 **Distribution of ions near a negatively charged surface.** An accumulation of counterions and a depletion of co-ions take place, shown graphically for a 1:1 electrolyte, where  $\rho_{\infty}$  is the electrolyte concentration in the bulk. The OHP is the plane beyond which the ions follow the Boltzmann distribution. Figure reproduced from reference 12, with permission. .... 9
- Figure 6 **DLVO theory.** Schematic representation of the energy vs distance profile. The DLVO total interaction is the sum of the electrostatic repulsion (double-layer) and of the VdW attraction and it depends on the surface charge density ( $\sigma$ ). Figure reproduced from reference 12, with permission. .... 10
- Figure 7 **Schematic representation of the two extreme cases for ligand morphology:** randomly mixed and Janus ligand shell. .... 13
- Figure 8 **Characterization of gold nanoparticles** (a) TEM image and histogram of the distribution of the size of the nanoparticles obtained by analysing multiple images. (b) SAXS spectrum of a diluted solution of nanoparticles. By fitting the spectrum, as described in section 4.5, the size of the particles can be obtained. In the case of spherical nanoparticles, the first minimum corresponds to  $9/d$ , where  $d$  is the diameter of the particles. (c) SANS spectra of the same batch of nanoparticles recorded in two different solvents (tetrahydrofuran- $d_8$ , circles, and chloroform- $d$ , triangles). The continuous lines show the fitting obtained with the Monte Carlo method. (d) NMR spectra, before and after iodine etching. In this example the peaks between 1 and 3 ppm correspond to the ligand (in this case 11-mercaptoundecane-1-sulfonate). Before etching (top) the peaks

look very broad because the ligand is attached to the nanoparticles. The absence of sharp peaks confirms the absence of free ligands. After etching the peaks of the ligands are much sharper. In the case of a ligand shell composed of a mixture of ligands, their relative ratio can be calculated from the integral of the intensity of the peaks. The peaks visible above 3 ppm are associated to the solvent. (e) TGA results, where the step and the plateau are clearly recognizable..... 14

Figure 9 **Zisman plot for a low-density polyethylene film**. The value of the surface tension of the highest surface tension liquid that completely wets the solid (cross) can be estimated by linear fitting the dependence of  $\cos\theta$  as a function of the surface tension of the solvents that do not wet completely the surface. Data replotted from reference 49. .... 17

Figure 10 **Schematic representation of the structure of the AFM**: a laser beam is focused on the back of the cantilever and reflected to the photodiode. By knowing the position of the reflection spot the feedback loop can move the piezoelectric stage (PZT scanner) and track the morphology of the surface (Image obtained from [https://upload.wikimedia.org/wikipedia/commons/archive/7/7c/20150821155945%21Atomic\\_force\\_microscope\\_block\\_diagram.svg](https://upload.wikimedia.org/wikipedia/commons/archive/7/7c/20150821155945%21Atomic_force_microscope_block_diagram.svg)). .... 18

Figure 11 **AFM force curves**. The red curve refers to the approach of the tip to the surface, the blue one to the retraction of the tip from the surface. On the left-hand side the deflection of the cantilever is plotted over time. If the sensitivity and spring constant of the cantilever are known, the force exerted on the cantilever can be calculated. The force exerted on the cantilever as a function of the position of the cantilever is shown on the right-hand side. The position is marked as 0 at the point of contact. The jump into contact is visible in the approach curve. The peak in the retraction curve is the force of adhesion ( $\sim 4$  nm in this case). .... 19

Figure 12 (A) Example of application of the proposed method. Three force curves collected to check the tip status before and after measuring a pair of samples. The tip did not change while scanning the first sample, but it was damaged while scanning the second sample. (B) Force curve collected on Au(111). An oscillatory signal is recorded due to the interference of the reflection of the laser beam from the cantilever and from the reflective substrate..... 22

Figure 13 (A) Test of the reproducibility of the proposed method: average of a series of 70 force curves on mica, a good overimposition of trace and retrace is shown. The variation over 70 force curves (the standard deviation of the data) is comparable with the variation on a single force curve. The first and the last force curves collected are reported for comparison, showing a good reproducibility of the measurement. (B) Example of a reference embedded in the sample. A triangular substrate and a rectangular substrate are stuck close to each other, in order to allow the movement of the cantilever from one side to the other (with no need to unmount the setup). The size of the gap between the two substrates is smaller than 100 micrometers, as measured by an optical microscope. 23

Figure 14 **Effect of alkyl chain disorder on SFG signal**. Surface disorder increases from (a) to (d). The peaks associated to the vibrations of the  $\text{CH}_3$  are indicated with r, while the

peaks associated to the CH<sub>2</sub> stretch are indicated with d (+ refers to symmetric stretching, - to antisymmetric stretching and FR to the Fermi resonance). In a very well packed self-assembled monolayer only the CH<sub>3</sub> peaks appear because all the contributions from the CH<sub>2</sub> cancel out (locally centro-symmetric environment), due to the high symmetry of the system. By increasing the disorder of the self-assembled monolayer, the CH<sub>2</sub> peak starts to appear. The ratio of the CH<sub>2</sub> / CH<sub>3</sub> peaks provides some information about the degree of order in the monolayer. In the limit of a totally disordered monolayer, the conformation of the ligands is essentially random and all resonances processes are inactive. Figure adapted from reference 71, with permission..... 25

Figure 15 **Representative spectrum of the D<sub>2</sub>O-air interface.** Three peaks are recognizable, respectively associated, from left to right, to strongly hydrogen bonded water, weakly hydrogen bonded water and free O-D (not hydrogen bonded). Adapted from reference 81, with permission. .... 26

Figure 16 **Representative UV-Vis spectra collected during the precipitation of nanoparticles.** HBr was added to negatively charged particles (diameter 4.0±0.6 nm). Precipitation was observed, while recording the spectra at different time intervals. Due to the presence of aggregates the overall slope of the spectrum decreases and a shift of the SPR peak is observed. Due to precipitation the absorbance decreases. .... 27

Figure 17 **Introduction to SAXS measurements.** (a) Schematics of the setup. (b) Effect of polydispersity of the nanoparticles on the collected spectra (normalized at low  $q$ , for clarity). Spectra simulated using the software SASFit<sup>81-82</sup>, for nanoparticles having a radius following a gaussian distribution around  $10 \pm \sigma$  nm. (c) Effect of the interactions between the nanoparticles on the collected spectra. Experimental spectra collected on gold nanoparticles having a ligand shell composed of 11-mercaptoundecane-1-sulfonate (negatively charged). The addition of salt results in a different DLVO potential and therefore a different interaction between the nanoparticles..... 28

Figure 18 **DLS measurements.** Three examples of DLS data. Smaller particles (red curve) diffuse faster, as visible by the correlation curve. The green curve is an example of a sample containing multiple populations. On the right-hand side the difference between the size distribution based on the scattering intensity and on the number is shown. The fact that larger particles scatter light more efficiently is the reason for the difference between the two plots. The number distribution should be used to calculate the relative ration between the different populations. As an example, in the green curve the micrometric particles scatter a lot of light, but their number is very little..... 30

Figure 19 **Summary of the data from Pietak *et al.*<sup>90</sup>** The relationship between the contact angle (left) or the surface energy (right) and the force of adhesion measured by AFM. The data is modeled by decomposing the force into two components: one due to the meniscus and the other one due to DMT adhesion arising from intermolecular attractions. Figures adapted from reference 90, with permission..... 34

Figure 20 **Visual evaluation of the quality of the linear fit for all the experiments performed with more than three reference samples.** Different measurements (corresponding to different tips being used) are plotted with different colors. For each

experiment the  $\gamma S$  vs  $Fadh$  curve has been fitted linearly. The obtained angular coefficient and intercept have been used to predict the expected force of adhesion, knowing the surface energy of the sample. If the assumption of linearity is correct all the points should sit on the dotted line in this plot. In fact, almost all the experimental error bars overlap with the dotted line, confirming the validity of the fit. The plot is also showing the effect of the tip on the measurement: in total six reference samples have been used. All of them have been measured in the experiment reported in grey, a subset of them has been measured in the other cases. In the blue case, the force is systematically higher than in the other cases. This can be due, for example, to a less sharp tip, which has a larger surface of contact. .... 36

Figure 21 **Measurement of the surface energy of a multicomponent system.** Two images have been obtained with a different set of parameters in order to have the same average deformation in the two cases on the two different components. The applied force is different in the two cases, the color-scales are the same (the difference between black and white is reported on the bottom-right corner of each image). Lower force is needed to measure the component on the left of each image, since it is softer. .... 37

Figure 22 **TEM images of the nanoparticles** before (A) and after (B) annealing. Based on the counting of more than 500 nanoparticles, the distributions of the core diameter are found to be  $5.1 \pm 0.6$  nm and  $5.2 \pm 0.7$  nm for nanoparticles before and after annealing, respectively. Figure reused from reference 1, with permission..... 43

Figure 23 **Characterization of the MPA-OT nanoparticles.** In all plots the blue and red lines refer, respectively, to nanoparticles before and after annealing. Note that for all measurements but SANS the two curves practically overlap with each other. (A) SAXS data on both nanoparticles measured using ethanol as solvent. A fit, assuming a Gaussian distribution of the size, gives a core diameter of  $4.9 \pm 0.6$  nm. (B) NMR spectra of the ligands detached from the core via an iodine decomposition. The measured ligand ratio is approximately MPA:OT = 55:45. (C) TGA plots for both particles showing that the ligand density is unaffected by annealing. Note that in TGA the experimental error is considered to be larger than 5%. (D) Fourier transformed infrared spectroscopy (FTIR) measurements taken from nanoparticle films in attenuated total reflection mode. The spectra show that MPA ligands are mainly deprotonated on both nanoparticles. (E) SANS spectra of nanoparticles taken in tetrahydrofuran-d<sub>8</sub>. The overlap in the low- $q$  region (below  $0.083 \text{ \AA}^{-1}$  corresponding to the overall size of the nanoparticles in real space, as indicated by the vertical line) shows that the two nanoparticles have the same radius of gyration. The scattering at higher  $q$  range is the only characterization that shows a significant difference for the two nanoparticles, indicating a difference in the shape of nanoparticles (i.e. patchiness of the ligand shell). (F) Low-resolution models for the nanoparticles obtained by fitting the curves shown in D and the ones collected in chloroform-d (dots are the experimental measures, and lines are the fits). In the SANS model, the blue beads stand for OT ligands while the green ones are MPA ligands. We should point out that the nanoparticles characterized in A, D and E are coated with OT and a deuterated version of MPA, for technical requirements of the techniques used. These nanoparticles are identical



to the ones described in the other panels. Figure reused from reference 1, with permission. .... 44

Figure 24 **SFG spectra for the nanoparticles (CH region)**. The amplitude ratio of the symmetric methylene ( $\sim 2850\text{ cm}^{-1}$ ) and the symmetric methyl ( $\sim 2880\text{ cm}^{-1}$ ) stretch vibrational modes are significantly different for the patchy and stripe-like particles. 45

Figure 25 **SFG characterization of the interfacial water structure**. (A) Schematic of the SFG setup. The IR and visible beam are focused on the same spot of the sample. The SFG signal is generated. (B-E) SFG spectra in the water region, as recorded in four different measurements (Blue: patchy nanoparticles, red: stripe-like nanoparticles) and associated amplitude ratio of the peaks due to the strong H-bond and the weak H-bond (insets). To avoid any error from laser fluctuations on different days, we choose to report our data separately. We calculated the peak to peak ratio error of the SFG scattering setup on 10 spectra of different samples of sodium dodecylsulfonate stabilized hexadecane nano-emulsions and the deviation from spectrum to spectrum is less than 10 %. This value is used as an error for the values reported on the graph. We have never observed an increase in the ratio of the H-bonds peaks for the annealed sample. The fact that during one experiment (D) we did not observe any difference between the two sets of nanoparticles can be explained by the fact that annealing may not have worked perfectly on that occasion. Since in the formation of the film it is likely that similar nanoparticles will assemble together, it is possible that in this case the laser was focused on an area composed of nanoparticles that were not affected by annealing. All the spectra have been normalized on the peak at  $\sim 2350\text{ cm}^{-1}$  to facilitate the visual comparison. Figures adapted from reference 1, with permission. .... 46

Figure 26  **$W_{SL}$  for the two sets of nanoparticles**, as measured by two independent techniques. The measurements show significant differences. The dotted line represents the additive average for the  $W_{SL}$  of the two mono-ligand nanoparticles measured using contact angle. The grey band is the error in the measurement of the additive average. .... 47

Figure 27 **Representative SAM-AFM images** (from left to right: height, amplitude and phase channels) collected on patchy nanoparticles (top) and on stripe-like nanoparticles (bottom). Circles indicate single particles that have been used for the calculation of  $W_{SL}$ . The value of the free phase of oscillation was  $95^\circ$  for the image on top and  $76^\circ$  for the one on the bottom. Figure reused from reference 1, with permission. .... 47

Figure 28 **Additional SFG measurements**. The spectra collected on the frequencies associated to the molecular vibrations of water (left) show a clear difference between the particles before and after annealing. The spectra collected on the CH region (right) show that the morphology of the ligand shell is different before and after annealing (the ligands being more disordered after annealing). An additional measurement has been performed on these nanoparticles: the CH spectra has been collected also in the dry state, showing that the ligands get more disordered when water is added (both before and after annealing). All the water spectra have been normalized on the peak at  $\sim 2350\text{ (1/cm)}$  to facilitate the visual comparison. The same has been done for the peak at  $\sim 2850\text{ (1/cm)}$  in the CH case. .... 48

Figure 29 **Molecular dynamic simulations of self-assembled monolayers together with water.** The four simulated surfaces are shown on the left-hand side (red: oxygen, grey: carbon, white: hydrogen). The two surfaces on the top resemble the patchy nanoparticles, while the two on the bottom the stripe-like ones. On the right-hand side the excesses for  $\mu$  and  $\rho$  are plotted. It is clear that the time-averaged structure of interfacial water is influenced by the patchiness..... 49

Figure 30 **Molecular dynamics simulations of water on trench configurations.** (A) Water density in a cut across trenches of varying size. Ligands occupy the black area of the pictures (shorter ligands are MPA, longer ligands are OT). (B) Cross-section of the density of water on a cut across the center of the trench. The thickness of each trench is mentioned in the legend (number of molecules). It is visible that, both for MPA trenches and OT trenches, the one-molecule thick trench shows a different density, while starting from trenches composed of two molecules the density on the center of the trench is almost constant. Figure adapted from reference 1, with permission. .... 50

Figure 31 **Nearest-neighbor model.** (A) Classification scheme: patterns 1 and 2 are equivalent by rotational symmetry, with an MPA molecule at the center, surrounded by 2 other MPA molecules next to each other; pattern 3 has an OT molecule at the center with 5 other OT molecules surrounding it; pattern 4 has an MPA molecule surrounded by 6 other MPA molecules, and does not contribute to the excess term. (B) Surface excess  $\Delta\rho$  and  $\Delta\mu$  of the patchy and stripe-like surfaces as calculated from molecular dynamic simulations (MD, continuous line) and by summing the contributions of the nearest neighbors obtained by the linear regression model (NN, dotted line), for the four surfaces. .... 51

Figure 32 **Re-analysis of the saturation concentration of similar MPA-OT nanoparticles** as previously reported<sup>40</sup>. The solvents are classified into three categories depending on whether the nanoparticles show monotonic dependence of the saturation concentration on the ligand shell composition. The solvents are then ordered according to their effective volume ( $V_{\text{eff}}$ ). In general, solvents that show non-monotonic saturation concentration have smaller  $V_{\text{eff}}$ , while solvents that show a monotonic trend for the saturation concentration have larger  $V_{\text{eff}}$ . Figures adapted from reference 1, with permission. 53

Figure 33 **Experimental validation of the proposed model.** (A)  $W_{\text{SL}}$  values of the patchy (blue) and stripe-like (red) nanoparticles in various solvents. The green shadings indicate solvents in which the  $W_{\text{SL}}$  shows significant differences (Student's t test assuming equal variances,  $P = 0.05$ ) for the 2 nanoparticles. The grey shadings indicate that the null hypothesis ("the 2 nanoparticles have the same work of adhesion") cannot be rejected. (The solvents used are: water (H<sub>2</sub>O), formamide (FA), ethylene glycol (EG), dimethyl sulfoxide (DMSO), glycerol (GLY), isopropanol (IPA), chloroform (CHCl<sub>3</sub>), dichlorobenzene (DCB), perfluorohexane (PFH), perfluorodecalin (PFD), 4-Cyano-4'-n-pentylbiphenyl (5CB) and hexadecane (C16).) (B) Dependence of the differences in  $W_{\text{SL}}$  for the two films on the effective volume of the solvent molecules. The color of the points is the same as the one of the shadings in (B) and relates to the significance of the differences in  $W_{\text{SL}}$ . Figures adapted from reference 1, with permission..... 53

**Figure 34 Representative SAXS spectra of nanoparticles in water** (A) Effect of ligand composition. Different nanoparticles having the same gold core but a different ligand shell. The ligands in the shell are MUS and OT. The OT percent for each batch is shown in the legend. Particles with 12 % OT show repulsive interaction analogous to the all-MUS ones. Increasing the hydrophobic content (OT) results in less repulsion and more attraction. At the limit of 43% OT, fractal aggregation is observed (aggregates of multiple sizes are present in the sample, as indicated by the linearity of the spectrum in the low- $q$  region). (B) Effect of the concentration of nanoparticles. Spectra have been collected on the same batch of nanoparticles (28% OT, core diameter  $3.8 \pm 0.5$  nm) at different concentrations. Increasing the concentration, the peak at low  $q$  moves to higher  $q$  values, because the particles get closer in real space. .... 57

**Figure 35 Results on water-ethanol mixtures.** (A) Effect of the addition of ethanol (10% and 20%) on different MUS:OT nanoparticles. The OT concentration in the ligand shell is labelled in the legend. The plots should be compared to the ones collected in water (Figure 34). Addition of ethanol results in reduced attraction between nanoparticles. (B) Effect of ethanol addition on MUS:brOT nanoparticles (13% brOT, core diameter  $4.3 \pm 0.6$  nm). Also in this case, the addition of ethanol reduces the interparticle attraction. .... 59

**Figure 36 Effect of addition of proline on interparticle interactions.** (A) Effect of addition of proline on different MUS:OT nanoparticles. The OT concentration in the ligand shell is labelled in the legend. The plots should be compared to the ones collected in water (Figure 34) and in water-ethanol mixtures (Figure 35). (B) Effect of proline addition on MUS:brOT nanoparticles (13% brOT, core diameter  $4.3 \pm 0.6$  nm). Also in this case the addition of proline reduces the interparticle attraction. .... 60

**Figure 37 Effect of addition of four different amino acids on interparticle interactions.** The case of MUS:OT nanoparticles and all-MUS nanoparticles are reported. In both cases proline and glycine have a stabilizing effect, while arginine and glutamic acid destabilize the suspension. The two batches of nanoparticles are not directly comparable in this case, because the size and polydispersity are different: the core diameter is  $4.0 \pm 0.6$  nm in the mixed ligand case and  $3.1 \pm 0.3$  nm in the mono-ligand case. .... 60

**Figure 38 Effect of the addition of two molecules with no effect on interparticle interactions.** (A) Addition of glycerol does not alter the interparticle interactions in the case of MUS:OT nanoparticles (OT  $\sim 40$  %). (B) Addition of DMSO does not significantly alter the interparticle interactions (tested both on MUS:OT and MUS:brOT nanoparticles). In both the cases the small shift in the water spectra is due to a wrong calibration of the sample-detector distance, which results in an error in the calculation of  $q$ . This experimental error does not affect the overall shape of the spectrum. .... 61

**Figure 39 Time evolution of the surface plasmon resonance for suspensions of nanoparticles upon addition of acids.** The wavelength associated to the maximum absorbance is plotted as a function of time. .... 62

**Figure 40 Effect of mixtures of molecules on the stability of suspensions of nanoparticles.** (A) SAXS spectra obtained after addition of proline, glutamic acid and a combination of both. The flattening of the spectrum in the low- $q$  region may indicate that

the particles are in a non-interaction regime (ideal gas state). (B) Restabilization effect due to addition of proline and glycine to aggregated nanoparticles (aggregation induced by glutamic acid). For technical requirements of the machines, the concentrations of nanoparticles used in A and B are different: 20 mg/ml in the SAXS case and 0.2 mg/ml in the UV-vis case..... 63

Figure 41 **Stabilization effect of proline on mixtures of saliva and pea protein.** DLS results on mixtures of saliva, pea protein (pp) and proline. Aggregation is visible in the pp+saliva mixture. On the contrary, pp+saliva+proline shows similar size as the pp and pp+proline samples. The size distribution for saliva is not affected by the addition of proline. As clearly visible in the pictures, 70 minutes after preparation of the samples, precipitation is evident in the pp+saliva sample, while only a small gradient in the color is visible in the case of pp+saliva+proline, indicating higher stability of this suspension. .... 64

# Chapter 1     Structure of the thesis

This thesis is divided into two main parts: the introductory chapters (2, 3 and 4) and the chapters describing new results (5, 6 and 7). More in detail, the structure of the thesis is described below.

In Chapter 2 the reader is introduced to the water structure, including the concepts of hydrophilicity and hydrophobicity. Surfaces and solid-liquid interfaces are introduced. The main physical properties associated to an interface are discussed. The interactions between particles and surfaces in a medium are described, starting from the classical DLVO theory and including solvation forces.

In Chapter 3 a short introduction to gold nanoparticles is provided. Only the concepts strictly relevant for the understanding of this thesis are described. The basic characterization techniques are also briefly introduced.

In Chapter 4 the main experimental techniques used in this thesis are introduced. The theory behind the measurements and some practical information about data collection and analysis are provided. In the case of atomic force microscopy, a method I have developed to characterize the quality of the tip is also discussed in this chapter.

In Chapter 5 a new method to measure the surface energy at the nanoscale through atomic force microscopy force curves is introduced. This method was developed during an internship to the chemical company BASF (Germany).

In Chapter 6 results on the non-additivity of interfacial properties for complex surfaces are presented. This effect was measured on gold nanoparticles and a new predictive model has been developed. These results have been reported on a paper appeared in the Proceedings of the National Academy of Science (PNAS) in 2019.<sup>1</sup>

In Chapter 7 new preliminary results on the possibility to use small molecules to solubilize suspensions of nanoparticles are presented. An example of applications to food science is described.

In Chapter 8 the overall conclusions of the thesis are summarized, together with an overview of possible further developments of the projects.



# Chapter 2 Introduction

## 2.1 Water

How can we describe water? Transparent, odorless, tasteless, but also ubiquitous, fundamental for life, poorly understood. A large number of technical reviews<sup>2-4</sup>, websites<sup>5-7</sup> and books addressed to the general public<sup>8-10</sup> describe the unusual properties of water and the reasons for which water is considered to be so interesting. All of them were summarized by Philip Ball in a short, remarkable, sentence: “water is not like other liquids, but neither it is wholly different”.<sup>2</sup>

In fact, in a simple liquid, molecules can be represented as particles that interact via a spherically symmetric potential. Hence, for a simple ideal liquid interacting through the Lennard-Jones potential ( $V(r) \sim (\sigma/r)^{12} - (\sigma/r)^6$ , where  $\sigma$  is the molecular diameter) the radial distribution function (RDF)  $g(r)$  is not very different from that of a “hard-sphere” fluid, in which the particles experience no intermolecular force until they touch. In both cases the RDF is oscillatory with a first prominent peak at  $r = \sigma$  and subsequent peaks at separations multiples of the intermolecular distance that decay rapidly

until the density reaches the one of the bulk liquid (Figure 1 a-b). These repulsive interactions create a dense random packing of the particles, characterized by a short-range ordering in the liquid. The inclusion of an attractive potential (without which no liquid-gas transition takes place) modifies only slightly the RDF.

In the case of water, the RDF is still oscillatory but one needs to define a series of partial  $g_{XY}(r)$  because there are two types of atoms in the molecules (H and O). In this case  $g_{XY}(r)$  indicates the probability of finding atom  $Y$  at a distance  $r$  from atom  $X$ . The partial RDFs for water, as determined by neutron scattering, are reported in Fig. 1c.<sup>2,11</sup> Even if the features in Fig. 1c look qualitatively similar to the ones in Figure 1a and b, their origin is different: they arise from the hydrogen bonds. The first peak in the  $g_{OO}(r)$  is at about  $1.4 \sigma$ , showing that the molecules are not as packed as the particles in a simple liquid would be. This is due to the fact that hydrogen bonds are attractive and directional: they bind water molecules into specific spatial orientations (the H atom involved in a bond sits roughly on the axis between the two oxygen atoms). As described by Israelachvili<sup>12</sup>, “the hydrogen bonding interaction is no more than a particularly strong type of directional dipole-dipole interaction”. However, there is yet no simple, accurate and predictive model for the interaction potential. The result of this interaction is that the intermolecular  $O \cdots H$  distance is only  $0.176$

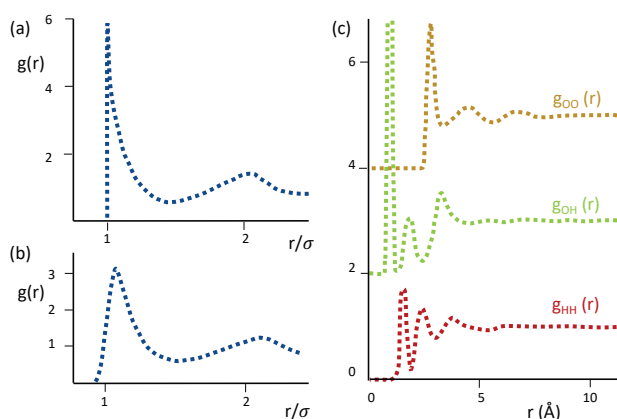


Figure 1 **Radial distribution functions** Typical RDF for simple fluids: (a) hard spheres, (b) Lennard-Jones potential. (c) Partial RDFs for water at 298 K. Adapted from references 2 and 11, with permission.

nm long, smaller than the 0.26 nm expected from the sum of the two Van der Waals radii, but larger than the covalent distance (0.1 nm).<sup>12</sup> Also, the strength of these bonds (between 10 and 40 KJ/mol or 5-10  $k_B T$  per bond at 298 K) lies between the one of Van der Waals interactions ( $\sim 1$  KJ/mol) and the one of ionic or covalent bonds ( $\sim 500$  KJ/mol).<sup>12</sup>

Each water molecule can be involved in up to four hydrogen bonds. The formation of these bonds plays therefore a crucial role in the determination of the behavior of water. For example, thanks to H-bonds water is capable of forming 3D structures in solids and to have a much longer short-range order in liquids, when compared to substances in which no H-bonds can be formed.<sup>12</sup> However, it should be stressed that the average lifetime of H-bonds in liquid water is 1 ps<sup>13</sup>, so although there exists an extended three dimensional network in the liquid, there is no long-lived single bond. While in ice the water molecules are tetrahedrally coordinated, in the liquid the molecules are mobile: not all the H-bonding sites are occupied at the same time and the average number of H-bonds per molecule falls to about 3.5. A smaller number of H-bonds per molecule allows the molecules to get closer to each other, resulting in liquid being denser than ice.

### 2.1.1 Hydrophobes

The strong propensity of water to form H-bonds influences its interactions with apolar molecules that are not capable of forming such bonds. When water molecules are placed in close vicinity to apolar molecules, they try to minimize the number of H-bonds lost because of the presence of those molecules. If the apolar solute is not too large it is possible for the water molecules to rearrange around it without giving up any H-bond. Even in the case of larger solutes, the main effect of bringing together water molecules and apolar ones is the reorientation of the former so that they can participate in as much H-bonds as possible. To do this, the H-bonds may have to bend from their favored linear configuration. As a result, depending on the size and shape of the inert solutes, the water molecules can reach a coordination of 4 (thereof the name of “iceberg model”), with lower enthalpy than in bulk liquid.<sup>2,14</sup> This phenomenon is known as *hydrophobic solvation*. Practically, if the solute is small enough the water density around it will increase because water molecules are localized as to maintain the H-bonds. In contrast, larger solutes (larger than 1 nm) are “dewetted” or “dry”, meaning that the water density is lower around them and the first hydration layer sits at a larger distance from the surface<sup>15,16</sup>. At present, there is no simple theory for this kind of solvent-solute interaction, however it is well known that this restructuring of water is entropically very unfavorable, since it disrupts the existing water structure and it imposes a new and more ordered one<sup>12</sup>. As a result, apolar substances are not miscible with water (a phenomenon called *hydrophobic effect*) and are named *hydrophobic substances*.

It should be noted that the “iceberg model” has been questioned by a number of studies<sup>2,14</sup>. In particular one of the most relevant alternatives is the one proposed by Garde and coworkers. According to this theory, the propensity of cavity formation on a surface is the best indicator of hydrophobicity of the surface itself.<sup>17</sup>

### 2.1.2 Hydrophiles

Oppositely to hydrophobes, hydrophiles are molecules that prefer to be in contact with water rather than with each other. In fact, as a polar species, water can engage in Coulombic interactions with ions, charged molecules and polar solutes. According to the traditional picture, water molecules surround cations with their oxygen atoms pointing towards the ions and vice versa for anions.<sup>2</sup> Smaller ions create a more intense electric field, thereof they are more hydrated than larger ions (they show a larger *hydrated radius*). The *hydration number* (number of water molecules bounded to an ion) normally oscillates between 4 and 6,



however very small ions, such as  $\text{Be}^{2+}$ , have a smaller hydration number because they are too small to simultaneously host more than four water molecules. Cations are generally more solvated than anions because of their smaller size, and, divalent cations are more solvated than monovalent ones because of their charge density. Small divalent and especially trivalent cations have a weak, but well defined, second hydration shell.<sup>12</sup> As a result, the time needed for a change in the orientation of a water molecule (comparable with the H-bond lifetime) is strongly affected by the presence of ions: the exchange of a water molecule in the first hydration shell of an ion can require hours.

Besides charged groups, some uncharged and even nonpolar molecules can be hydrophilic if they have the right geometry and if they contain atoms able to do H-bonds with water, such as the oxygen atom in the alcohol group or the nitrogen atom in the amines.<sup>12</sup>

## 2.2 Surfaces

According to the Cambridge dictionary, “the surface is the outside part (of anything)”, or as Sylvie Roke wrote in her PhD thesis, it “is the end of a bulk”.<sup>18</sup> The simplicity of the definition hides the complexity of the science of this particular part of every existing material, to the point that Wolfgang Pauli used to say that God made the bulk, while the surface was invented by the devil.<sup>19,20</sup> The diabolic nature of the surface comes from the fact that it shares its border with the external world.<sup>19</sup> While every molecule in the bulk is surrounded by other molecules of the same material, at the surface the molecules are exposed to the environment: this exposure changes the structure of the material itself.

The simplest example is that of a crystal: in an ideal, infinite crystal each individual atom in the bulk is at the position associated to its crystal structure, due to the forces exerted on it by all the other atoms. If a surface is introduced (by terminating the crystal) the forces on the atoms at the surface are altered and therefore the equilibrium position of the atoms is not the same as in the bulk. This phenomenon is called *surface reconstruction*.<sup>21</sup>

The creation of a surface in a material requires a certain amount of energy, corresponding to the energy needed to break the intermolecular bonds during the formation of the surface itself. *Surface energy* is defined as the free energy change associated to the creation of one-unit area of the surface and it is indicated with  $\gamma$ .<sup>12,21</sup> Surface energy is always a positive number: otherwise the surface would tend to expand indefinitely.<sup>12</sup>

It should be noticed that, for historical reasons, the surface energy of a liquid is often referred to as *surface tension* (and reported equivalently either in units of energy/unit area or force/unit length).<sup>12</sup>

Due to the presence of the H-bonds, the surface tension of water (72.8 mN/m at 20 °C) is higher than the one of most of the liquids, as shown from the examples reported in the following table<sup>22</sup>:

Solvent	Surface energy (mN/m)
water	72.8
glycerol	63.4
ethylene glycol	47.7
acetone	23.3
ethanol	23.7
toluene	28.4
chloroform	27.5

## 2.3 Solid-liquid interfaces

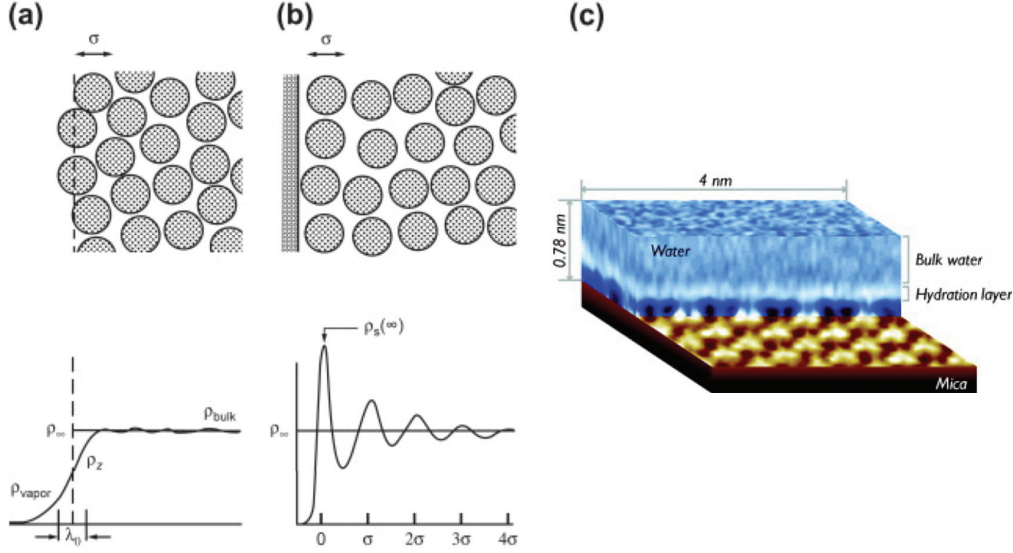


Figure 2 **Liquid density profiles at interfaces.** (a) Vapor-liquid interface.  $\rho_\infty$  is the bulk liquid density and  $\lambda_0$  is the width of the interface. (b) Liquid density profile at an isolated solid-liquid interface.  $\rho_s(\infty)$  is the “contact” density at the surface. (c) Three-dimensional atomic force microscopy visualization of the first hydration layers at the water-mica interface. (a, b) are reproduced from reference 12, with permission, (c) is reproduced from reference 23, with permission.

When two surfaces approach each other closer than a few nanometers they interact. As for the case in which the surface is created, the atoms (or molecules) at the surface will feel a different environment than the ones in the bulk and will react to it, reaching a new arrangement. In particular, we will focus here on the case in which a liquid is placed in contact with a solid: the rearrangement will take place almost exclusively in the liquid, because the bonds in the solid are much stronger. With the name *interface* we refer to the area in which the solid and the liquid interact and the structure of the liquid is affected by the presence of the solid and therefore different from the bulk.

Analogously to the case of the surface energy, an *interfacial energy* can be defined<sup>12</sup>, which is the free energy needed to expand the interface by one unit area and it is normally indicated as  $\gamma_{ij}$  (where  $i$  and  $j$  are the two materials composing the interface). The values of the interfacial energies are always positive: if they were to be negative the interface would expand indefinitely and it would eventually disappear (the two substances would be miscible).

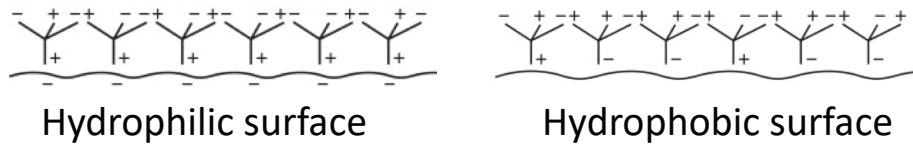


Figure 3 **Schematic representation of the water ordering in the first hydration layer of a solid-liquid interface.** In the case of a negatively charged surface (hydrophilic) the water molecules are forced to orient with one of the two  $H^+$  pointing toward the surface. This severely restricts the way the first layer of water molecules can orient. On the contrary, on a hydrophobic surface, the molecules reorient in order to minimize the number of H-bonds lost, without any restriction on the charge pointing toward the surface. Adapted from reference 12, with permission.

Another quantity associated to an interface is the *work of adhesion*<sup>12</sup>: the free energy change to separate unit areas of two surfaces from contact to infinity in a vacuum, normally indicated as  $W_{ij}$  (where  $i$  and  $j$  are the two materials composing the interface). The work of adhesion is always positive since all media attract each other in a vacuum.

Since the process of creating a unit area of a surface is equivalent to that of separating two half-unit areas of the material, from the definitions of surface energy and work of adhesion it follows that:

$$\gamma_1 = W_{11}.$$

Also, the process of creating a unit area of an interface is equivalent to creating two-unit areas of the two surfaces and bringing them into contact, thereof:

$$\gamma_{12} = \gamma_1 + \gamma_2 - W_{12} = \frac{1}{2}W_{11} + \frac{1}{2}W_{22} - W_{12}.$$

Once these definitions have been understood, it is easy to derive the work of adhesion of medium 1 and 2, when immersed into 3 (i.e. two solids in contact in a liquid)<sup>12</sup>: in fact, while separating 1 and 2, a unit area of the interface 1-2 is lost while a unit area of each of the interfaces 1-3 and 2-3 is created. The total value of  $W_{123}$  can be either positive or negative, depending on whether there is attraction or repulsion between 1 and 2 when immersed in 3:

$$W_{123} = \gamma_{13} + \gamma_{23} - \gamma_{12}.$$

Besides these thermodynamic considerations, what happens at the molecular scale in a solid-liquid interface? The symmetry of the bulk liquid is broken at the interface because of the interaction with the solid. The presence of the solid constrains the motion of the molecules in the liquid at the interface, lowering their degrees of freedom and forcing them to stay at a favored distance from the surface. At such distance, the density of molecules is higher than in the bulk. The liquid density oscillates when moving away from the surface, with the intensity of the peaks getting lower and lower until the density stabilizes to the bulk value (as visible in Figure 2<sup>23</sup>). By looking at the profile of the oscillations of the density it is possible to identify the *solvation layers* (*hydration layers* in the case of water), which are due to the fact that the liquid is structured at the interface.

In the case of water, the nature of the surface plays a major role in determining the position of the first hydration layer. At a hydrophilic surface (composed of molecules capable of forming H-bonds) the water molecules are forced to orient in a certain direction with one of the two hydrogens pointing towards the surface. This severely limits the way in which the first hydration layer is formed and its distance from the surface. The same limitation is not present on a hydrophobic surface (Figure 3).<sup>12</sup> The result is that the first hydration layer sits closer to the surface in the hydrophilic case.

In the hydrophilic case the surface has a higher work of adhesion: more energy is needed to separate the water from it, because of the formation of the hydrogen bonds. This phenomenon is visible macroscopically from the fact that water spreads on hydrophilic surfaces much more than on hydrophobic ones. It follows that two drops with the same volume of the same liquid, always have the same shape when deposited on

the same surface. In particular, one can measure the angle formed by the drop on the surface, at equilibrium (Figure 4). This angle is called *contact angle*<sup>12</sup> and, for small drops, it is independent from the volume of the drop. As Young and Doupré showed<sup>12</sup>, by using a thermodynamic approach, the contact angle  $\theta$  and the work of adhesion are linked in the following way (S: solid and L: liquid):

$$W_{SL} = \gamma_L(1 + \cos \theta).$$

Surfaces with a contact angle smaller than  $90^\circ$  are called *wetting-surfaces* (hydrophilic in the case of water), while surfaces with a contact angle larger than  $90^\circ$  are called *non-wetting surfaces* (hydrophobic in the case of water). On the other side, when talking about a specific surface, *wetting liquids* and *non-wetting liquids* can be defined, depending on the contact angle they form with the surface (respectively lower and higher than  $90^\circ$ ).<sup>24</sup>

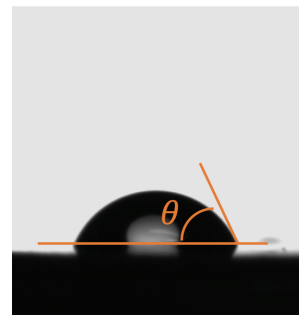


Figure 4 **Contact angle**: it is the angle formed by a drop on the surface, at the triple line (where the liquid, the solid and the vapour meet).

## 2.4 Interactions between particles and surfaces in a medium

The interactions between colloids and those between surfaces can be treated within the same theoretical framework: in both cases the H-bond rearrangement in the water molecules at the interface takes place in a different way than around smaller molecules because of geometrical constraints (see section 2.1). In fact, the classical theories for colloidal interactions, described in the following paragraphs, are appropriate only for particles with a diameter in the range of the micrometers. On the contrary, it is well known that they are not sufficiently accurate to predict the interactions in the cases of nanoparticles with a diameter below 20 nm, because the particles and the molecules of the media have a similar size in this case.<sup>25</sup> Because of this similarity, the discreteness of the solvent and its fluctuations around the nanoparticles play an important role in the determination of electrostatic, van der Waals and hydrophobic interactions, which are found to be nonadditive at this scale. However, a new model able to predict these non-additive effects has not been proposed yet and the classical colloidal theories are still in use to describe the interactions between nanoparticles.

### 2.4.1 Electrical double layer

Many surfaces are charged when immersed in liquids. The charging of a surface can happen in different ways, for example ionization or dissociation of surface groups and absorption or binding of ions from the solution can happen. Whatever the charging mechanism, the final surface charge is balanced by oppositely charged counter-ions. Some of them are bound to the surface, within the so-called *Stern layer*, others form a charged, dynamic, region called *diffuse electric double-layer*.<sup>12</sup> These two concepts are important both in the case of surfaces immersed in an electrolyte solution and in the case of liquids in which the only ions that are present are the counterions.

Figure 5 schematically shows the distribution of the ions at the interface. The concentration of counterions at the surface depends only on the surface charge density and on the concentration of counterions in the bulk, while the concentration of counterions in the double layer follows the Boltzmann distribution (it decreases monotonically when increasing the distance from the surface).<sup>12</sup>

For low surface potentials (below 25 mV) the distance at which counterions fully screen the charge of the surface is called Debye length ( $\kappa^{-1}$ ) and can be calculated by knowing the valency of the ions, their concentration and the dielectric constant of the medium.

The Debye length does not depend on the properties of the surface, while it is strongly affected by the properties of the solution (in particular by the valency of the ions). Divalent ions are much more effective than monovalent ions in screening the charge. In the following table  $\kappa^{-1}$  is reported in the case of different concentrations of NaCl and CaCl<sub>2</sub> in water. Longer  $\kappa^{-1}$  is present in solutions with less salt: the screening of the electrostatic repulsion is limited in these cases.

		Salt concentration		
		0	0.1 mM	1 M
Salt	NaCl	960 nm	30.4 nm	0.3 nm
	CaCl <sub>2</sub>	960 nm	17.6 nm	0.2 nm

The presence of a very large (but finite)  $\kappa^{-1}$  in pure water is due to the dissociation of water molecules into H<sub>3</sub>O<sup>+</sup> and OH<sup>-</sup>.

#### 2.4.2 DLVO theory

How do charged surfaces interact in a medium? The simplest model available is the DLVO theory (established in the forties by Derjaguin, Landau, Verwey and Overbeek).<sup>26</sup>

This theory considers two kinds of interactions: the Van der Waals (VdW) attraction and the electrostatic repulsion.

VdW interaction is due to dipole-dipole (permanent or induced) interactions in the material and is therefore short-ranged and attractive. Its potential is largely independent from the electrolyte concentration and pH and can be considered as fixed in a first approximation. It always exceeds the double-layer (electrostatic) repulsion at small enough distances.

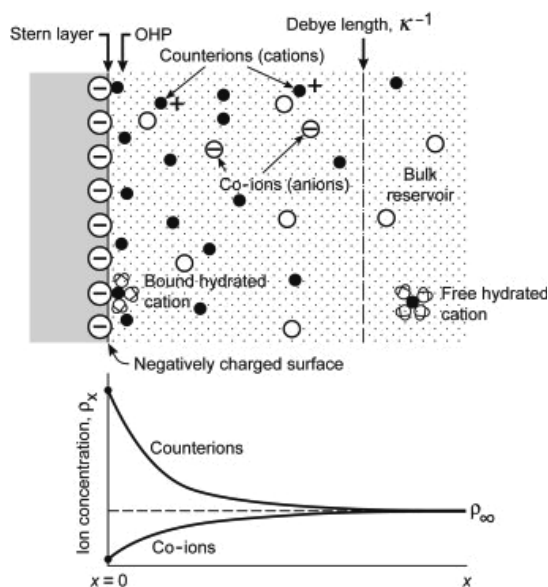


Figure 5 **Distribution of ions near a negatively charged surface.** An accumulation of counterions and a depletion of co-ions take place, shown graphically for a 1:1 electrolyte, where  $\rho_\infty$  is the electrolyte concentration in the bulk. The OHP is the plane beyond which the ions follow the Boltzmann distribution. Figure reproduced from reference 12, with permission.

The combination of VdW interactions and electrostatic repulsion gives rise to the potential shown in Figure 6. At short ranges the VdW attraction is always predominant, creating a primary minimum corresponding to the two surfaces being in contact. Depending on the electrolyte concentration and the surface potential (that affect the double layer) different cases are possible for the long-range effects. Let us start from the case in which the surfaces are highly charged and immersed in a diluted electrolyte: a strong long-range repulsion is present, with an energy barrier preventing the aggregation. If the electrolyte is more concentrated a secondary minimum can appear (separated from the first one by an energy barrier). Even if the thermodynamic equilibrium is still the contact condition, this colloidal system can be kinetically stable when the particles are located in the secondary minimum. For surfaces of lower charge density, the energy barrier gets lower, leading to aggregation (unstable colloidal suspension). As the surface potential approaches zero, the interaction curve approaches the pure VdW curve and the two surfaces attract each other at all separations.

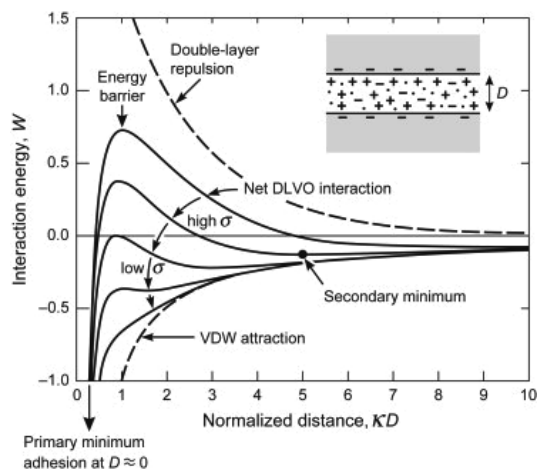


Figure 6 **DLVO theory**. Schematic representation of the energy vs distance profile. The DLVO total interaction is the sum of the electrostatic repulsion (double-layer) and of the VdW attraction and it depends on the surface charge density ( $\sigma$ ). Figure reproduced from reference 12, with permission.

### 2.4.3 Solvation forces

One of the key assumptions of DLVO theory is that the surfaces interact relatively weakly with the molecules of the dispersion medium.<sup>26</sup> Consequently, interaction between particles is mainly due to dispersion forces and electrostatic repulsion. In most cases the presence of the medium is not negligible and due to its presence additional contributions to the overall interparticle interactions arise, which are normally referred to as solvation forces. Their phenomenology is controversial and even more their theoretical description.<sup>12</sup> Below, the main theories about non-DLVO interactions between hydrophobic and hydrophilic surfaces immersed in water will be reviewed. The origins of the solvation forces are still unknown, but there is some agreement on the fact that they are supposed to be surface forces rather than body forces (only the surface is involved in the interaction, with no effect from the molecules of the bulk).<sup>12</sup>

Empirically, it is sometimes observed that hydrophilic surfaces repel each other. The decay of this hydration repulsion seems to follow an exponential law (with a decay length of about 1 nm). However, it should be stressed that this phenomenon is not always observed: the interactions between smooth mica surfaces (hydrophilic) in a diluted electrolyte solution follow the DLVO theory and deviations are observed only in the case of higher salt concentrations.<sup>2,12</sup> The origin of this repulsion force is still under debate and may either come from the structuring of the liquid at the interface (see section 2.3) or from the properties of the surface itself.<sup>2</sup>

On the contrary, it has been consistently observed that hydrophobic surfaces attract each other in a liquid much more than what is expected from VdW interactions (and much more than they attract in vacuum).<sup>2,12,27</sup> Three main models are available to describe this kind of interaction, but no agreement exists on which is the best one.

The first possible explanation for the hydrophobic attraction considers the water structure at the interface. The liquid immediately adjacent to the hydrophobic surface is considered to be more vapor-like than liquid-like, and the mechanism for the interaction is the depletion.<sup>12,28</sup> The predicted interaction potential is a decaying oscillatory force over-imposed to a monotonic attraction, but its range is shorter than the predicted one.

An alternative explanation for the hydrophobic forces is based on electrostatic models. It has been suggested that, because of the water orientation at the interface and because of the longer relaxation time for H-bonds near to hydrophobic molecules, a dipole can be induced at a hydrophobic surface. In this framework, long-range attraction between surfaces would arise from induced dipole-dipole interactions.<sup>2,12,29,30</sup>

Another reasonable explanation for the long-range hydrophobic attraction invokes the formation of vapor bridges. In fact, hydrophobic surfaces are prone to pick up nanoscopic air bubbles, that can bridge together two surfaces when they get closer, creating a strong attractive capillary force. This explanation agrees with a certain number of studies that suggest that long-range (above 10 nm) hydrophobic interactions disappear in degassed water. However, it is not clear whether this would be the case also for interactions with a decay length below 10 nm. It has been suggested that the two hydrophobic interactions with different length-scales (above and below tens of nanometers) may have different origins (the shortest one being the relevant one for the folding and aggregation of proteins).<sup>2,12</sup>

Whatever the right explanation for the hydrophobic interaction, it is clear that there is no simple way to relate the nature of a hydrophobic molecule and the attraction between hydrophobic surfaces. The cross-over between small molecules and large surfaces is believed to happen more or less at 1 nm.<sup>15,27,31</sup>





## Chapter 3 Introduction to gold nanoparticles

According to the definition of the European Commission, a nanomaterial is “a natural, incidental or manufactured material containing particles, in an unbound state or as an aggregate or as an agglomerate and where, for 50 % or more of the particles in the number size distribution, one or more external dimensions is in the size range 1 nm - 100 nm.”<sup>32</sup>

Different nanomaterials are normally named depending on their shape, so that it is easy to distinguish nanoribbons, nanowires, nanotubes, and so on. In this context the term *nanoparticle* is normally used to refer to spherical objects, having a diameter between 1 and 100 nm. They can be composed of different materials that, together with their size, are crucial in the determination of their properties.

Nanoparticles are not always composed of a single material: core-shell nanoparticles have an inner core and an outer shell composed of different materials. Both the materials will have a key role in the determination of the properties of the system. This is the case for the gold nanoparticles used in this thesis: the gold core is surrounded by a shell composed of thiolated molecules.

This kind of gold nanoparticles has been studied and characterized in detail over the last 30 years.<sup>33–39</sup> One of their advantages is that the ligand shell can be designed<sup>35–37</sup>: not only different ligands can be attached on the surface in order to modify its charge, degree of hydrophobicity and solubility in different solvents, but also mixtures of ligands can be used. Depending on the molecules used and on the protocol for the preparation, different arrangements are possible for the ligands, giving rise to different shell morphologies. The two extreme morphologies for a ligand shell composed of two ligands are the *Janus* and the *randomly mixed* (Figure 7). In the case of a Janus nanoparticle, protected by ligands A and B, the surface

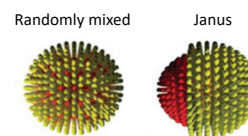
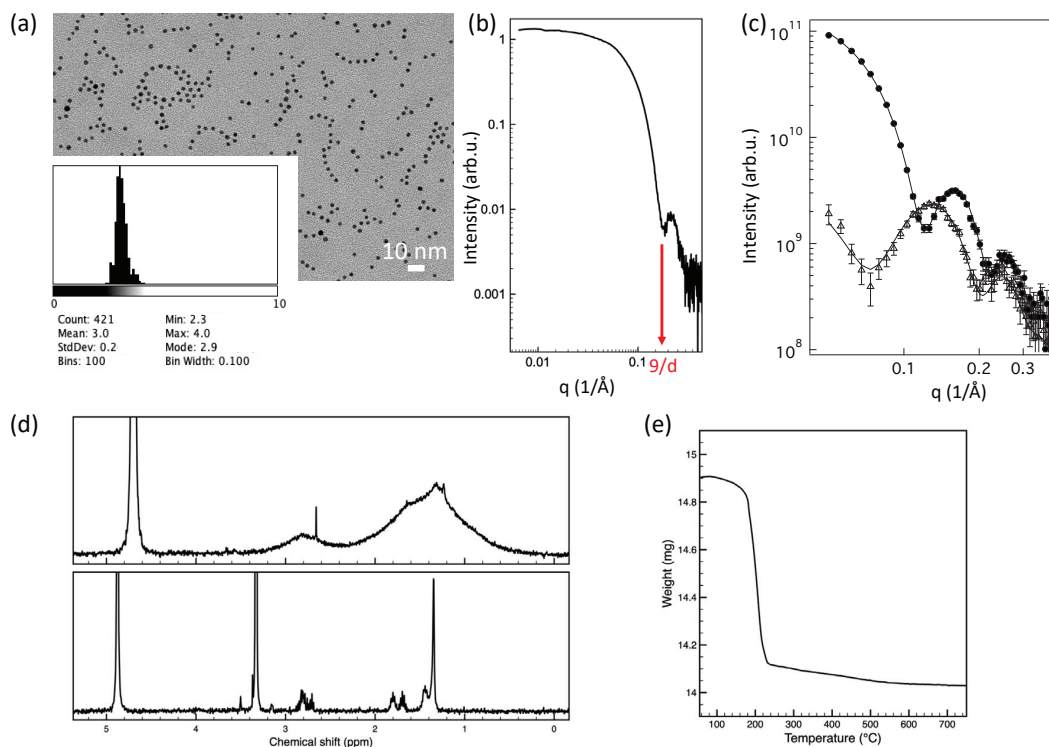


Figure 7 **Schematic representation of the two extreme cases for ligand morphology: randomly mixed and Janus ligand shell.**

of the nanoparticle is divided into two areas: one totally covered by ligand A and the other one covered by ligand B. The two ligands do not mix. Reversely, in the case of a randomly mixed ligand-shell the distribution of the ligands is random and it is equally probable to find ligand B next to ligand A or next to another ligand B. In between the two extreme cases, a variety of *patchy* conformations for the ligand shell exist. In this case patches composed of ligand A are surrounded by ligand B and vice versa. The size and shape of these patches can be tuned by choosing the ligands involved and/or the synthesis procedure.

In fact, the self-assembly of thiolated ligands on the surface of gold nanoparticles is mainly affected by the difference in length of the ligands used: specifically, the tendency toward separation between the ligands driven by free energy minimization is modified by a significant increase in tail conformational entropy that arises when long ligands are surrounded by shorter ones (the same is valid in the case of ligands with a different degree of bulkiness). The curvature of the surface of the nanoparticles plays a large role on the self-assembly of the monolayer allowing for the formation of smaller patches than on flat gold.<sup>38,39</sup>



**Figure 8 Characterization of gold nanoparticles** (a) TEM image and histogram of the distribution of the size of the nanoparticles obtained by analysing multiple images. (b) SAXS spectrum of a diluted solution of nanoparticles. By fitting the spectrum, as described in section 4.5, the size of the particles can be obtained. In the case of spherical nanoparticles, the first minimum corresponds to  $9/d$ , where  $d$  is the diameter of the particles. (c) SANS spectra of the same batch of nanoparticles recorded in two different solvents (tetrahydrofuran-d<sub>8</sub>, circles, and chloroform-d, triangles). The continuous lines show the fitting obtained with the Monte Carlo method. (d) NMR spectra, before and after iodine etching. In this example the peaks between 1 and 3 ppm correspond to the ligand (in this case 11-mercaptoundecane-1-sulfonate). Before etching (top) the peaks look very broad because the ligand is attached to the nanoparticles. The absence of sharp peaks confirms the absence of free ligands. After etching the peaks of the ligands are much sharper. In the case of a ligand shell composed of a mixture of ligands, their relative ratio can be calculated from the integral of the intensity of the peaks. The peaks visible above 3 ppm are associated to the solvent. (e) TGA results, where the step and the plateau are clearly recognizable.

Thanks to their size range and surface properties, this kind of nanoparticles have been used in several studies, addressing a variety of topics: fundamental problems in nanoscience<sup>40,41</sup>, interactions with biological samples<sup>42–44</sup>, the possibility to use them as sensors<sup>45</sup> and so on.

A freshly synthesized batch of nanoparticles needs to be characterized before being used. Different characterization techniques may be used, depending on what needs to be known (Figure 8). Here a summary of the most commonly-used techniques and their relevance is reported:

- **Transmission electron microscopy** (TEM, Figure 8a): since the contrast in electron microscopy comes from the differences in electron density on the imaging plane, TEM is a very suitable technique to image the highly electron dense gold core of the nanoparticles. In fact, TEM images can be used as a fast way to inspect the shape and size of the gold core. A series of images needs to be collected in order to have significant statistics for the size of nanoparticles. The average size (together with its standard deviation) can be easily computed from the size distribution of the imaged nanoparticles.

- **Small angle X-rays scattering** (SAXS, Figure 8b): this is another technique that, thanks to the high electron density of gold, can be used to measure the average size of the core of the nanoparticles. The setup and its applications (also beyond the measurement of the gold core) will be discussed in detail in section 4.4.
- **Nuclear magnetic resonance spectroscopy** (NMR, Figure 8d): this technique is useful to characterize the purity of the nanoparticles and the ligand ratio on the ligand shell. For every batch of nanoparticles two sets of data are collected. The first spectrum is collected on the whole nanoparticles in order to check for the absence of free ligands, potentially remained from the synthesis procedure. Once the cleanness of the nanoparticles is confirmed, the gold core is etched (with iodine) and another spectrum is collected, from which the ligands in the ligand shell can be characterized and their relative ratio can be calculated.<sup>46,47</sup>
- **Thermogravimetric analysis** (TGA, Figure 8e): this is an experimental technique that measures the change in mass of a sample as a function of temperature in a controlled atmosphere. The thermogravimetric analyzer used for TGA experiments consists of a high-precision thermo-balance, which is connected to a holder inside a temperature-controlled furnace. The result of a thermogravimetric measurement is displayed as a mass versus temperature curve<sup>48</sup>. When increasing the temperature of the core-shell nanoparticle the weight of the particles is constant until a critical temperature at which the ligands desorb from the surface, showing a clear step in the TGA curve. After the step, at higher temperatures, the weight plateaus to the value associated to the gold core. The quantification of the step height gives information on the ligand density on the surface of the nanoparticles.
- **Small angle neutron scattering** (SANS, Figure 8c): this is an advanced characterization technique for the ligand shell of nanoparticles.<sup>35</sup> In fact, three-dimensional models of the core and of the ligand shell can be obtained by simultaneously fitting two SANS spectra.<sup>35</sup> The two spectra need to be collected in two solvents having a different contrast in neutron scattering.<sup>35</sup> Also, in order to be able to distinguish two different ligands in the ligands shell and generate a map of their arrangement, the two of them need to have a different contrast, this is why one of them needs to be deuterated.<sup>35</sup> The fitting is performed using an ab initio reconstruction method (based on a Monte Carlo algorithm).<sup>35</sup> Since this technique requires access to a neutron source it cannot be performed routinely.



# Chapter 4 Main techniques used

## 4.1 Contact angle

The concept of static contact angle has been defined in section 2.3. Its measurement enables the quantification of the work of adhesion of the liquid to the sample thanks to the Young-Dupré equation, if the surface tension of the liquid is known (section 2.3).

The setup for the measurement is simple: it is composed of a stage, on which the sample can be mounted, and a needle to release the liquid (in volumes in the range of the microliters). A camera allows to take a side-view picture of the drop on the sample. Image analysis allows for the estimation of the contact angle, through the identification of the baseline (the line where the liquid and the solid meet) and the tangent of the droplet edge at the triple line (where the three phases meet).

A series of contact angle measurements can be used to estimate the surface energy of a solid sample.<sup>49</sup> The simplest method is based on the Zisman theory<sup>50</sup>: Zisman defined the surface energy of a solid to be equal to the surface tension of the highest surface tension liquid that completely wets the solid, with a contact angle  $\theta = 0^\circ$ . The measurement is performed by measuring the contact angle of a series of solvents: the solvents with low surface tension show a contact angle of  $0^\circ$ , while, starting from a critical value of the surface tension, the contact angle is different from  $0^\circ$ . The surface tension of the highest surface tension liquid that completely wets the surface can be easily extrapolated, as shown in Figure 9. This theory works best for non-polar surfaces and becomes inadequate if the surface is even marginally polar. In fact, this one-parameter model does not consider specific liquid/solid interactions.

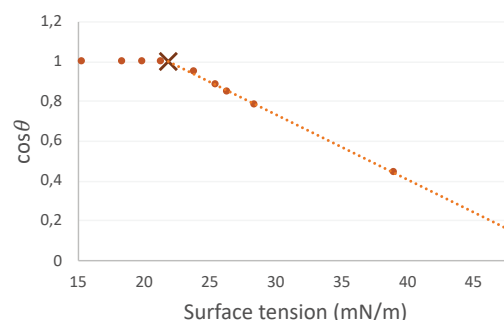


Figure 9 **Zisman plot for a low-density polyethylene film.** The value of the surface tension of the highest surface tension liquid that completely wets the solid (cross) can be estimated by linear fitting the dependence of  $\cos \theta$  as a function of the surface tension of the solvents that do not wet completely the surface. Data replotted from reference 49.

To overcome this problem, Owens and Wendt developed a two-parameters model to consider the polar interactions between the liquid and the solid.<sup>51</sup> The model assumes that the surface energy of a material is composed of two components: the polar ( $\gamma^P$ ) and the dispersive one ( $\gamma^D$ ). For most of the solvents the values of the polar and dispersive components of the surface tension can be found tabulated.<sup>49,52</sup> Owens and Wendt discovered that, if the contact angle is measured with a series of solvents, the following relation holds:

$$\frac{\gamma_L(\cos \theta + 1)}{2\sqrt{\gamma_L^D}} = \sqrt{\gamma_S^P} \sqrt{\frac{\gamma_L^P}{\gamma_L^D}} + \sqrt{\gamma_S^D}$$

where L and S refer respectively to the liquid and the solid. By fitting the linear relation between  $\frac{\gamma_L(\cos\theta+1)}{2\sqrt{\gamma_L^D}}$  and  $\sqrt{\frac{\gamma_L^P}{\gamma_L^D}}$  it is possible to obtain the expected values for  $\gamma_S^P$  and  $\gamma_S^D$ . The sum of the two corresponds to the total surface energy of the sample.

## 4.2 Atomic force microscopy (AFM)

Atomic force microscopy is a scanning probe microscopy (SPM) technique: images of surfaces are formed using a physical probe (tip) that scans the specimen. To form images, the tip is scanned over the surface and a value is recorded at discrete intervals (which value depends on the type of SPM and the mode of operation). These recorded values are displayed as a false color image.

In general, in an atomic force microscope the tip is glued to a cantilever, on the back of which a laser is focused. Thanks to the reflection of the laser the deflection of the cantilever can be tracked and therefore the interactions of the tip with the surface can be detected (Figure 10). When working in contact mode (the simplest mode) the tip is touching the surface all the time during the scan and the cantilever is therefore deflected. The deflection can be measured by the position of the reflected laser beam (on the photodetector). A feedback loop is operated to actuate a piezoelectric motor (located either on the sample stage or on the cantilever holder) to tune the tip-sample distance and maintain the deflection constant during the scanning. In this way the morphology of the surface can be reconstructed.

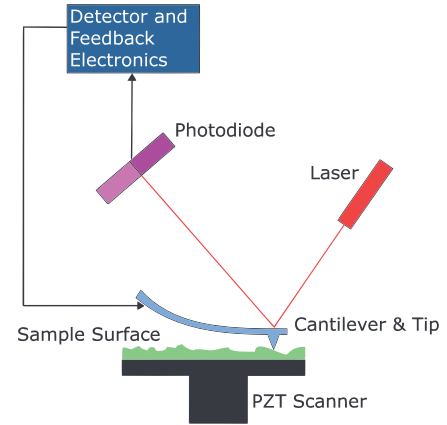


Figure 10 **Schematic representation of the structure of the AFM:** a laser beam is focused on the back of the cantilever and reflected to the photodiode. By knowing the position of the reflection spot the feedback loop can move the piezoelectric stage (PZT scanner) and track the morphology of the surface (Image obtained from [https://upload.wikimedia.org/wikipedia/commons/archive/7/7c/20150821155945%21Atomic\\_force\\_microscope\\_block\\_diagram.svg](https://upload.wikimedia.org/wikipedia/commons/archive/7/7c/20150821155945%21Atomic_force_microscope_block_diagram.svg))

The contact mode has been the first one to be invented (1986)<sup>53</sup> and it is the one with the easiest principle of operation. However, it presents the big disadvantage that, being the tip always in touch with the sample, it can be damaged very easily and vice versa the sample can be damaged by the scanning. As a result, many imaging artifacts can occur and the resolution is relatively low.

On the contrary, non-contact measurements performed in liquid guarantee a much higher resolution (sub-nanometric). This type of measurement is typically performed by oscillating the tip over the surface, close to its resonance frequency. In the vicinity of the surface the oscillations are affected by its presence: a feedback loop operates to keep the amplitude (amplitude modulation mode, AM) or frequency (frequency modulation mode, FM) constant. Basically, the surface is tracked by measuring the tip-sample interactions through the shift in the resonance frequency, rather than by reading the deflection of the cantilever. These modes are much gentler because the tip is oscillating on the surface, rather than touching it all the time, resulting in images with higher resolution and fewer artifacts. A specific way to operate in amplitude modulation mode is discussed in detail in section 4.2.2.

In the next section (4.2.1), instead, the concept of force curve is discussed, together with the possibility of mapping tip-sample interactions.

#### 4.2.1 Force curves and force maps

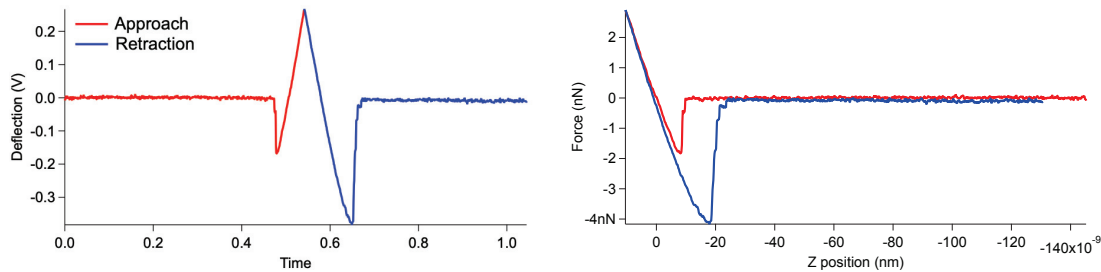


Figure 11 **AFM force curves**. The red curve refers to the approach of the tip to the surface, the blue one to the retraction of the tip from the surface. On the left-hand side the deflection of the cantilever is plotted over time. If the sensitivity and spring constant of the cantilever are known, the force exerted on the cantilever can be calculated. The force exerted on the cantilever as a function of the position of the cantilever is shown on the right-hand side. The position is marked as 0 at the point of contact. The jump into contact is visible in the approach curve. The peak in the retraction curve is the force of adhesion ( $\sim 4$  nm in this case).

Force curves are a common technique in AFM to measure the interactions between the tip and the sample.<sup>54</sup> The simplest way to record a force curve is to approach the tip to the surface until a certain deflection (*setpoint*) is obtained and move it back afterwards (Figure 11). If the sensitivity and the spring constant of the cantilever are known, from the deflection it is possible to calculate the force exerted on the cantilever during the tip-sample interaction. In fact, the most common way to display force curves is by plotting the force as a function of the position of the cantilever.

From this kind of curves it is possible to measure the response of a sample to an applied force. Depending on the sample and on the properties of interest, the setpoint value can be set on a different physical property (i.e. instead of a maximum value for the deflection, it is possible to set, for example, a maximum force or a maximum indentation).

In general, the common features to all force curves (plotted as force vs cantilever position, see Figure 11) are the following:

- *Non-contact region*: when the tip is far from the surface no force acts on the cantilever, as a result a flat line is visible in the force curve.
- *Jump into contact*: while the tip is approaching the sample, an attractive force appears that brings the tip in contact with the surface. A small, negative, peak in the force is associated to this “jump”.
- *Contact region*: when the tip touches the surface, positive values of the force are recorded (because the surface pushes against the tip). Depending on the mechanical properties of the material the response can be linear (elastic material) or not. In the case of a non-elastic material the approach and retraction curves do not overlap in the contact region.
- *Force of adhesion*: it is the difference between the force in the non-contact area and the negative peak in the retraction curve. This peak is due to the attractive interactions between the sample and the tip.

- *Deformation*: the deformation of the sample due to the interaction with the tip can be read in the force curve as the distance between the point of contact (at which the force starts to be positive) and the point at which the maximum force is achieved. It is zero for an ideal non-deformable sample and increases for softer samples.

As in the case of AFM images, that can be performed in the static (contact mode) and dynamic modes, also in the case of force curves both options are available: in the dynamic case, the cantilever is driven to oscillate during the approach and the retraction so that the amplitude and the phase of the oscillation are recorded, together with the deflection, as a function of the distance from the surface.<sup>55–57</sup> All the additional data recorded provide information about the tip-sample interactions.

It should be clear at this point that by analyzing force curves many different phenomena can be probed, among others: the mechanical properties of the surface<sup>58</sup>, the interfacial-liquid structure<sup>59,60</sup>, protein unfolding<sup>61,62</sup> and cell adhesion.<sup>63</sup> The force curves for each of these phenomena show specific features: different data analysis techniques are applied to each different case.

Force curves can be collected on a grid of points in order to map the interaction of interest, such as the force of adhesion or the deformation of the sample. The data collected in this way are called *force maps*. If good resolution is needed, the collection of a force map can require a long time (even hours) since a whole force curve needs to be collected for every pixel. Besides the time limitations, this approach is problematic because thermal drift is always observed for a sample mounted on an AFM stage. Because of thermal drift, if the collection of an image requires a long time (exactly how long depends on the scan size and the drifting speed) the image will be distorted and not realistic. For this reason, many AFM-producing companies invested in the development of faster ways to record the same information. The most popular, commercially available, solutions in this context are the PeakForce mode from Bruker and the Fast Force Mapping Mode from Asylum. In these modes, force curves can be collected at high frequencies (in the kHz range, depending on the manufacturer) and they can be analyzed either online or offline to get a high-resolution map of the tip-sample interactions (and therefore of the mechanical properties of the sample).

#### 4.2.2 Small amplitude modulation atomic force microscopy (SAM-AFM)

When imaging in amplitude modulation mode, the oscillation of the tip is sinusoidal. The cantilever is driven to oscillate with an amplitude  $A_0$  (free amplitude) when far away from the surface. As the tip approaches the sample the amplitude decreases until it reaches the chosen setpoint value ( $A$ ), which is kept constant while scanning the surface. On the contrary, the phase shift ( $\Delta\varphi$ ) between the phases of the driving wave ( $\varphi_0$ ) and of tip oscillation ( $\varphi$ ) is allowed to vary freely. The ratio  $A/A_0$  is important because it provides an indication of the imaging conditions: an high ratio corresponds to soft imaging conditions (less perturbative) while a lower ratio corresponds to harsher conditions.<sup>64</sup>

In the case of small amplitude modulation (SAM-AFM), the images are collected in amplitude modulation mode in liquid, with amplitudes smaller than the depth of the solvation region and a harmonic oscillation of the tip. In this case the structure and properties of the liquid are probed instead of those of the surface, as described below.<sup>64–66</sup>

Images collected in SAM-AFM can be used to calculate the work of adhesion of the solvent to the surface. In fact, the energy dissipated by the cantilever in one cycle of oscillation is strongly affected by the structure of the interfacial liquid: since a liquid with strong affinity for the surface is more ordered and less mobile at the



interface than in the bulk, it takes more energy for a vibrating AFM tip to displace interfacial liquid molecules than bulk molecules. If all the energy dissipation takes place in the interfacial liquid (no dissipation takes place in the sample), the amount of energy dissipated by the tip in one cycle of oscillation correlates with the work of adhesion of the liquid to the surface.<sup>65</sup> The measurement is therefore very sensitive to local variations in the properties of the interfacial liquid at the nanoscale.<sup>64–66</sup>

As shown by Vöitchovsky *et al.*<sup>41,65</sup>, the work of adhesion can be estimated with the following equation:

$$W_{SL} = a + b \left[ \frac{AA_0 \left( \cos \Delta\varphi - \frac{A}{A_0} \right)}{1 - e^{-\frac{\alpha A}{2}}} \right]^2,$$

where  $\alpha$  is the exponential decay length of the density of work of adhesion at the solid-liquid interface (typically a few molecular diameters) and  $a$  and  $b$  are two constants.  $a$  and  $b$  are affected by the mechanical properties of the cantilever and of the tip (specifically the spring constant and quality factor of the cantilever and the radius and work of adhesion of the tip).  $A$ ,  $A_0$  and  $\Delta\varphi$  are recorded during the measurement: the values of the working amplitude ( $A$ , corresponding to the value of the setpoint amplitude) and of the phase ( $\varphi$ ) are obtained from the respective channels in high resolution images while the value of the free amplitude needs to be measured immediately after the collection of high-resolution images by keeping the driving amplitude constant and moving the tip away from the surface, in order to measure the amplitude of oscillation in bulk water ( $A_0$ ). In the same way the value of the phase while oscillating in the bulk ( $\varphi_0$ ) needs to be checked and  $\Delta\varphi = \varphi_0 - \varphi$  needs to be calculated. On the other side, an estimation of the value of  $\alpha$  can be obtained from the molecular diameter ( $\sigma = 2.8 \text{ \AA}$  in the case of water): in general, one can assume that  $\alpha = \frac{3}{2\sigma}$ .<sup>65</sup>

This method does not provide an absolute measurement for the work of adhesion, but only a relative one:  $a$  and  $b$  need to be calibrated through the measurement of contact angle on reference samples. In fact, since the energy dissipation is calculated with respect to the oscillation of the cantilever in the bulk liquid, the intercept of the calibration line, which corresponding to  $A = A_0$  and  $\Delta\varphi = 0$ , is always given by the surface tension of the imaging liquid. Only one reference sample is therefore needed for the calibration.<sup>1</sup>

It should be emphasized that this approach is valid only if the liquid forms a well-defined solvation landscape on the surface (a wetting liquid is used) and if sub-nanometer resolution can be achieved.<sup>66</sup> Other important assumptions of the model include the fact that the interface is fully located in the liquid, the restructuring of the liquid at the interface fully accounts for the interfacial energy, the solid surface is locally flat compared to the tip, which is assumed to be parabolic, and the lateral motion of the tip is negligible compared to the vertical one.<sup>65</sup>

While performing this kind of measurements on different samples the status of the tip needs to be as constant as possible. In fact, it plays a large role in the determination of the measured value of phase shift observed and so of the proportionality factor  $b$ . A variation of the radius or of the work of adhesion of the tip is difficult to detect but can change significantly the measured value of the phase shift. Quantitative data can only be obtained if the unmodified status of the tip is confirmed. Smoothing of tip asperities and absorption of contaminants may change both the radius and the work of adhesion of the tip.

### 4.2.3 Development of a method to evaluate the tip quality

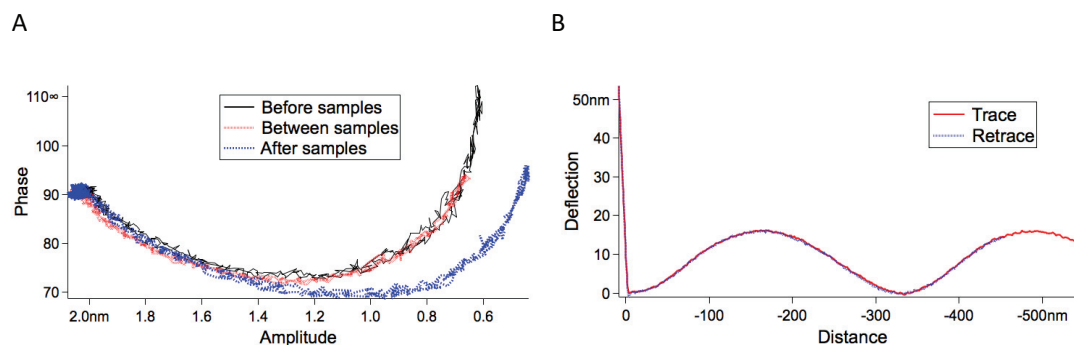


Figure 12 (A) Example of application of the proposed method. Three force curves collected to check the tip status before and after measuring a pair of samples. The tip did not change while scanning the first sample, but it was damaged while scanning the second sample. (B) Force curve collected on Au(111). An oscillatory signal is recorded due to the interference of the reflection of the laser beam from the cantilever and from the reflective substrate.

To the best of my knowledge, the only methods presented in literature to quickly check, during the measurement, the quality of the tip, focus on its sharpness<sup>67–70</sup>, but no method is described to check the global interaction between the sample, the liquid and the tip, taking into account also the possible contamination of the tip. The measurement of the thermal spectrum of the cantilever gives a general overview on the quality of the cantilever<sup>66</sup> but very often small modifications of the tip are not immediately recognizable in a thermal spectrum.

I have developed a method, based on the collection of dynamic force curves, to check the global interactions of the tip with the sample and the liquid, to perform precise quantitative small amplitude modulation AFM in liquid and compare the results obtained on different samples. This method does not allow for the quantification of the radius and work of adhesion, but allows to check that the tip-liquid-sample interactions are not changing over time. It is based on the collection of dynamic force curves on a reference sample, to check the dependence of the phase shift from the amplitude and infer if and how much the tip has changed. In this case, the ideal representation of the force curve is the one that shows the phase as a function of the amplitude of the oscillation. When far away from the surface, if the cantilever is oscillating at his resonance frequency, the phase is 90° and the amplitude corresponds to the free amplitude. When the tip interacts with the surface both the amplitude and the phase decrease.

The protocol to check the tip status is composed of the following steps:

1. A series of force curves is collected on a reference sample. The range of free amplitudes tested is slightly larger than the range used during the measurement, in order to check all the possible interactions. Normally the best imaging parameters are not known before imaging a new sample: a test performed on a larger range of free amplitudes allows to change a wider range of parameters while scanning the sample. The trigger point should be selected as small as possible (to decrease the risk of tip damage), but high enough to see the contact region. The curve length should be selected long enough to show the interaction of the tip with the sample (adhesion) and to guarantee an ending point far away from the surface. However, there is no need to collect very long force curves, which may decrease the stability of the measurement. I found that when working with small amplitude on a clean reference sample, a curve length of 20 nm is generally a good compromise.

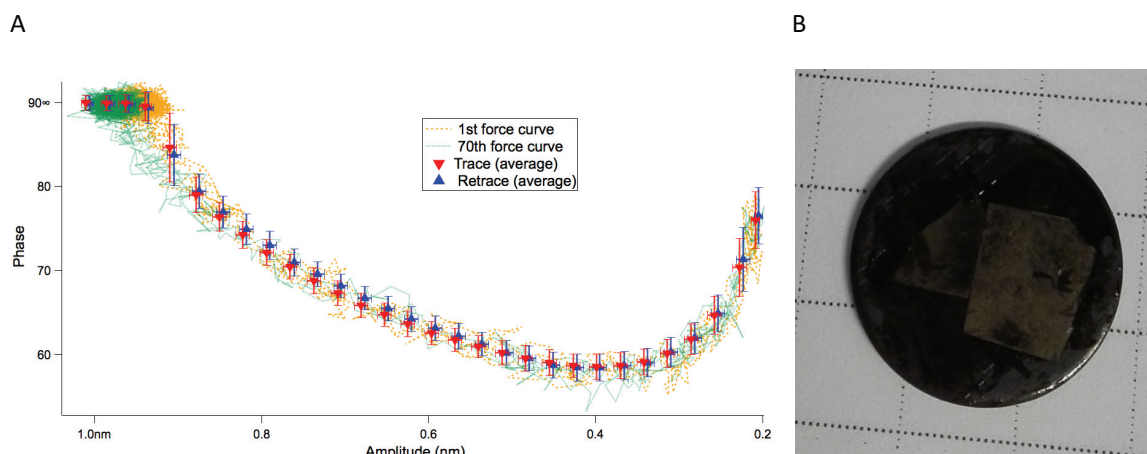


Figure 13 (A) Test of the reproducibility of the proposed method: average of a series of 70 force curves on mica, a good superimposition of trace and retrace is shown. The variation over 70 force curves (the standard deviation of the data) is comparable with the variation on a single force curve. The first and the last force curves collected are reported for comparison, showing a good reproducibility of the measurement. (B) Example of a reference embedded in the sample. A triangular substrate and a rectangular substrate are stuck close to each other, in order to allow the movement of the cantilever from one side to the other (with no need to unmount the setup). The size of the gap between the two substrates is smaller than 100 micrometers, as measured by an optical microscope.

2. The relevant sample is imaged.
3. A series of force curves is collected on the reference sample, paying attention to use the same parameters used at point 1. Superimposition of the force curves collected in point 3 to those collected in point 1 (Figure 12A) allows for an immediate detection of tip variation.
4. Iteration of points 2 and 3 up to the end of the measurement.

The reference sample used should have a work of adhesion constant at the nanometer scale and must be flat. Because of this, crystals that can be exfoliated are good candidates. Reversely, I found that highly reflective substrates, such as Au(111), do not work well as reference samples. In fact, in force curves collected on those substrates an interference between the signal reflected from the cantilever and the signal reflected from the substrate takes place, resulting in a wavy appearance of the deflection curve (Figure 12B). This effect can be minimized by adjusting the position of the laser spot to the center of the cantilever (in order to minimize the reflection from the substrate) and depends on the width of the cantilever with respect to the laser spot. In any case, in our setup, it is not possible to remove it completely. As a result, the setpoint required to collect a force curve on Au(111) is larger than on mica and the risk of damaging the tip is higher.

An example of the application of this test is reported Figure 12A. Three force curves collected on freshly cleaved mica are presented, two samples were scanned between them. It is immediately visible that the third force curve differs from the previous two. This means that while the measurements on the first sample did not change the tip, the measurements on the second sample induced a modification on the tip. Depending on the  $A/A_0$  ratio that is used to scan the relevant sample, and on the precision needed on the measurement, one can decide whether the tip can still be used or not and if the data obtained on the second sample can be considered or should be neglected. In the presented example, the interactions of the tip are not affected down to a setpoint of roughly 1.4 nm.

The significance of the test performed here can be understood by checking Figure 13A. In this case 70 force curves have been collected on a sample and the variability between them is negligible, confirming the validity of the previously described test to verify the unmodified status of the tip.

One of the advantages of this test is that it is relatively quick to perform. The time needed to mount the reference sample, collect a series of force curves and remount back the relevant sample is less than 30 minutes, but it can be decreased even more by including the reference on the actual sample (an example of sample preparation in this case is reported in Figure 13B). In this case, if the AFM is combined with an optical camera the cantilever can be quickly moved from the relevant sample to the reference, without need to unmount the sample. It is important to notice that in this case particular attention should be taken in order to avoid cross contamination of the reference sample.

It is important to consider that force curves on a flat surface do not probe eventual lateral interactions coming from the side of the tip. Therefore, the test of tip status is valid only if the sample of interest is flat, relatively to the tip.

## MATERIALS AND METHODS

To develop this testing procedure all the AFM data were acquired on freshly cleaved mica on a Cypher ES (Asylum). Force curve acquisition was carried out in dynamic mode in ultrapure water, generally putting a trigger on the deflection at a value between 1 and 3 nm. The tip velocity was generally 40 nm/s. The cantilever was oscillated piezoacoustically at its resonance frequency. Temperature was kept constant at 25°C.

Olympus RC800PSA cantilevers (lever number 3, nominal spring constant  $k$  0.76 N/m) were used. Their sensitivity was evaluated from force curves and the spring constant was measured from their thermal spectra.

### 4.3 Sum Frequency generation spectroscopy (SFG)

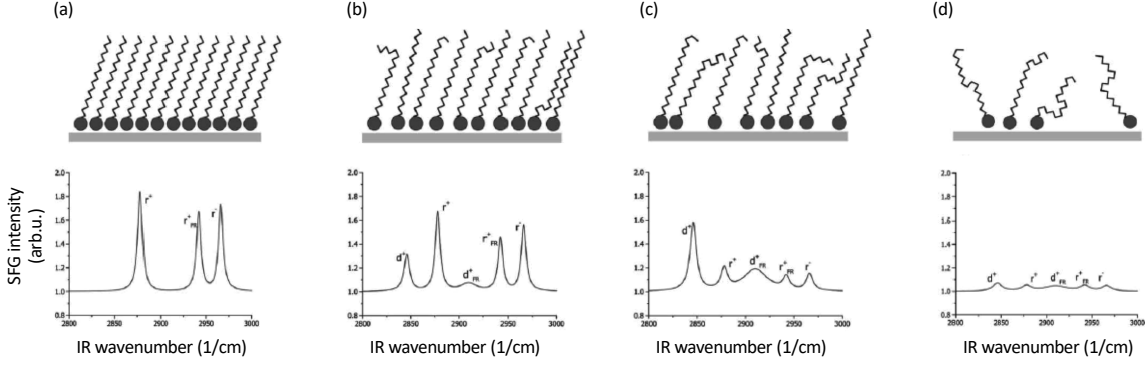


Figure 14 **Effect of alkyl chain disorder on SFG signal.** Surface disorder increases from (a) to (d). The peaks associated to the vibrations of the CH<sub>3</sub> are indicated with r, while the peaks associated to the CH<sub>2</sub> stretch are indicated with d (+ refers to symmetric stretching, - to antisymmetric stretching and FR to the Fermi resonance). In a very well packed self-assembled monolayer only the CH<sub>3</sub> peaks appear because all the contributions from the CH<sub>2</sub> cancel out (locally centro-symmetric environment), due to the high symmetry of the system. By increasing the disorder of the self-assembled monolayer, the CH<sub>2</sub> peak starts to appear. The ratio of the CH<sub>2</sub> / CH<sub>3</sub> peaks provides some information about the degree of order in the monolayer. In the limit of a totally disordered monolayer, the conformation of the ligands is essentially random and all resonances processes are inactive. Figure adapted from reference 71, with permission.

Sum frequency generation spectroscopy is a vibrational spectroscopy technique that is used to probe surfaces and interfaces.<sup>71,72</sup> A brief introduction to the theory is reported in the next paragraphs.

In general, when light propagates through an optical medium, the oscillating electromagnetic field  $\mathbf{E}$  exerts a polarizing force on all the electrons in the medium. The resulting polarization  $\mathbf{P}$  can be expanded in powers of  $\mathbf{E}$  as:

$$\mathbf{P} = \epsilon_0(\chi\mathbf{E} + \chi^{(2)}\mathbf{E}\mathbf{E} + \chi^{(3)}\mathbf{E}\mathbf{E}\mathbf{E} + \dots)$$

where  $\chi$  is the linear susceptibility and  $\chi^{(2)}, \chi^{(3)}, \dots, \chi^{(n)}$  are higher order susceptibility tensors.

In the case of two incident beams ( $\mathbf{E}_1$  and  $\mathbf{E}_2$ , oscillating over time with frequencies  $\omega_1$  and  $\omega_2$ ), the electromagnetic field of the total beam can be expressed as:

$$\mathbf{E} = \mathbf{E}_1 \cos \omega_1 t + \mathbf{E}_2 \cos \omega_2 t.$$

By substituting this electric field into the expression for the polarizability one finds that, the second order response can be decomposed into several new fields: a direct current field (i.e., no frequency dependence), two fields with frequencies  $2\omega_1$  and  $2\omega_2$  (second harmonic generation, SHG), a field with frequency  $\omega_1 - \omega_2$  (difference frequency generation, DFG), and a field with frequency  $\omega_1 + \omega_2$  (sum frequency generation, SFG).

The second order susceptibility  $\chi^{(2)}$  is a 27 components tensor. However, depending on the symmetries of the system, only a subset of these components is different from zero. In the case of a centrosymmetric medium, one expects:

$$P(E) = \epsilon_0(\chi E + \chi^{(2)}EE + \dots) = -P(-E) = -\epsilon_0(-\chi E + \chi^{(2)}EE + \dots)$$

The only possibility to fulfill this equation is that, for all terms of even order  $\chi^{(i)} = -\chi^{(i)}$ . Second order optical processes are therefore not allowed in centrosymmetric systems. This phenomenon implies the well-known surface selectivity of SFG: even in the cases in which the bulk is centrosymmetric (as in a liquid), at the surface the symmetry is broken and therefore the SFG signal recorded comes only from the surface layers (or from the interface) even in the case of a laser focused on a spot much larger than the interface itself.

Besides this, the selection rules for SFG are the combination of the selection rules for Raman transitions and for infrared transitions. In other words, during the molecular vibration, the changes in both the dipole moment and the polarizability must be different from zero.

In practice, in the experimental setup a visible beam and an infrared beam are focused on the same spot on the sample: the detector is set to measure the SFG beam, which has a frequency that is the sum of the two incident frequencies and travels in a direction given by the sum of the wavevectors of the incident beams.

SFG spectroscopy has been widely used to characterize alkyl chains adsorbed on surfaces.<sup>71,73–75</sup> In fact, the interpretation of the SFG spectrum for a linear alkyl chain is relatively simple, as explained in the detailed review by Lambert *et al.*<sup>71</sup> and schematically shown in Figure 14.

Because of the surface sensitivity of SFG, this technique has been successfully used to characterize the water structure at air-liquid and solid-liquid interfaces.<sup>76–81</sup> In this case three peaks can be detected (Figure 15). One of them (at the highest frequency) is associated to the stretch of the oxygen-hydrogen bond, in absence of hydrogen bonds. The other two, broader, peaks, are normally interpreted as associated to two kinds of hydrogen bonded water, involved in stronger or weaker hydrogen bonds.

In practice, in many setups, it is not possible to measure the full range of the water spectrum in a single measurement because a wide range of IR frequencies needs to be used for the incident beam. As a consequence, several spectra need to be collected, each centered at a different IR frequency, and combined together in order to get the final water spectrum. The procedure to combine the spectra is described in detail by Smolentsev *et al.*<sup>80</sup>

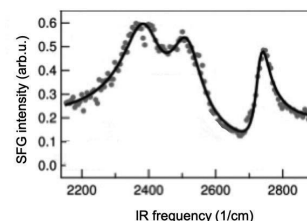


Figure 15 **Representative spectrum of the D<sub>2</sub>O-air interface.** Three peaks are recognizable, respectively associated, from left to right, to strongly hydrogen bonded water, weakly hydrogen bonded water and free O-D (not hydrogen bonded). Adapted from reference 81, with permission.

#### 4.4 Ultraviolet-visible spectroscopy (UV-vis)

UV-vis spectroscopy refers to absorption spectroscopy in the UV and visible spectral regions. It is a useful technique to characterize gold nanoparticles because of their surface plasmon resonance (SPR). In fact, at a specific wavelength of incident light, collective oscillations of electrons in the gold core of the nanoparticles cause the SPR, resulting in strong absorption of light. The particular wavelength of light at which this happens is strongly dependent on the nanoparticle size, shape, surface and aggregation state. SPR is responsible for the red colour of gold nanoparticles allowing for a visual inspection of the quality of the samples: in fact, changes in the size or aggregation state of gold nanoparticles can immediately be recognized by a difference in the colour of their suspensions. UV-vis spectroscopy allows for a quantification of this phenomenon, with the advantage of being a cheap, non-destructive and fast technique.

Typically, the UV-vis spectrum of spherical non-aggregated gold nanoparticles shows a broad band around 520 nm, due to the SPR, on top of the decay due to Rayleigh scattering ( $\propto \lambda^{-4}$ ). It has been shown that it is possible to calculate the size of the nanoparticles from the UV-vis spectrum, for particles having a diameter between 4 and 25 nm (with larger particles showing SPR at higher  $\lambda$ ).<sup>82</sup>

UV-vis spectroscopy can also be used as a way to detect the concentration ( $c$ ) of diluted solutions, using Lambert-Beer law:

$$A = \varepsilon Lc$$

where  $A$  is the measured absorbance,  $\varepsilon$  is the dielectric constant of the medium and  $L$  is length of the optical path in the medium. In the case of concentrated solutions, in which solute-solute interactions can take place, the linear dependence is not valid anymore. However, the dependence is always monotonic: a decrease in absorbance is always associated to a decrease in concentration.

From what has been discussed above, one can conclude that in the case of a precipitating sample of gold nanoparticles, a shift of the SPR to higher  $\lambda$  is observed (due to aggregation) together with a decrease of the absorbance (due to precipitation and therefore reduced concentration in the supernatant). The scattering profile also changes because of the size of the aggregates. An example of data recorded during aggregation is shown in Figure 16.

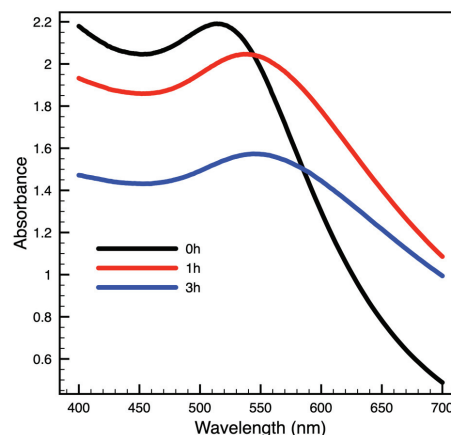


Figure 16 **Representative UV-Vis spectra collected during the precipitation of nanoparticles.** HBr was added to negatively charged particles (diameter  $4.0 \pm 0.6$  nm). Precipitation was observed, while recording the spectra at different time intervals. Due to the presence of aggregates the overall slope of the spectrum decreases and a shift of the SPR peak is observed. Due to precipitation the absorbance decreases.

## 4.5 Small angle x-rays scattering (SAXS)

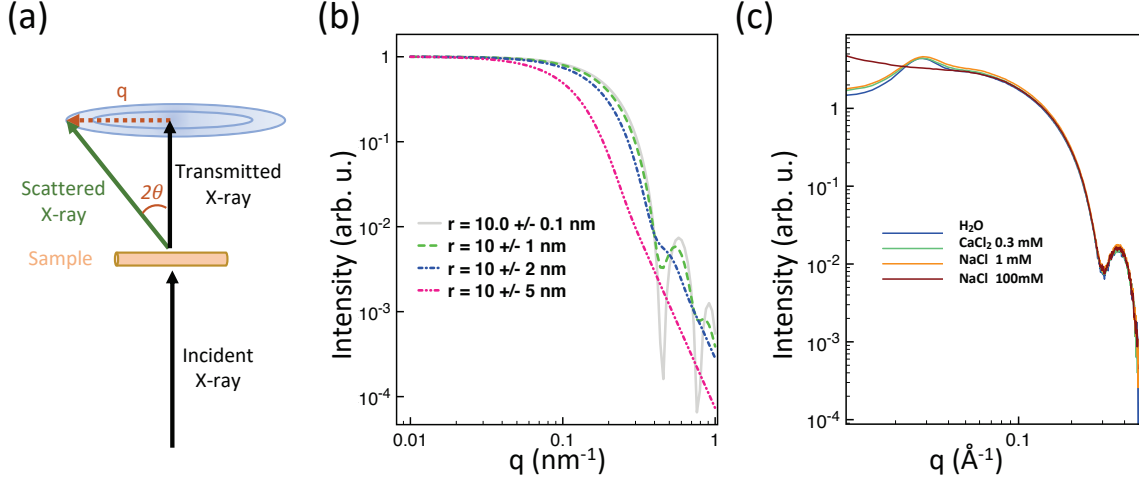


Figure 17 **Introduction to SAXS measurements.** (a) Schematics of the setup. (b) Effect of polydispersity of the nanoparticles on the collected spectra (normalized at low  $q$ , for clarity). Spectra simulated using the software SASFit<sup>81-82</sup>, for nanoparticles having a radius following a gaussian distribution around  $10 \pm \sigma$  nm. (c) Effect of the interactions between the nanoparticles on the collected spectra. Experimental spectra collected on gold nanoparticles having a ligand shell composed of 11-mercaptoundecane-1-sulfonate (negatively charged). The addition of salt results in a different DLVO potential and therefore a different interaction between the nanoparticles.

SAXS is a broadly used non-destructive technique to characterize nanoscale density differences in a sample (either liquid, solid, or in the gas state).<sup>83,84</sup> The elastic scattering of X-rays by the sample is measured at small angles (Figure 17a). SAXS is typically capable of delivering structural and periodicity information in the range between 1 and 100 nm. The scattering intensity is normally plotted as a function of the magnitude of the scattering vector  $q$ , which can be directly calculated from the scattering angle  $\theta$ , knowing the wavelength  $\lambda$  of the incident beam:

$$q = 4\pi \frac{\sin \theta}{\lambda}.$$

When performing scattering measurements for a suspension of nanoparticles, the scattering intensity  $I(q)$  represents the spherically averaged Fourier transform of the autocorrelation function ( $\gamma(r)$ ) of the electron density of the particles:

$$I(q) = \langle FT(\gamma(r)) \rangle$$

and it can be obtained by spherically averaging the scattering pattern recorded on the detector.

As a consequence, in the case of non-interacting particles (dilute solution) the expected scattering profile can be calculated knowing the shape of the particles (and their number  $N$ , which acts simply as a multiplying factor) and vice versa the spectrum can be fitted to evaluate the size of particles of a given shape.<sup>85-87</sup> Figure 17b shows the effect of polydispersity on the spectrum of spherical nanoparticles: the characteristic features of the monodisperse sample become less and less visible when the standard deviation of the radius of the particles increases. In the case of monodispersed spherical particles, it has been shown that there is no need



to fit the full spectrum because the diameter of the particles can be obtained, to a good approximation, by calculating  $9/r$ , where  $r$  is the position of the first minimum (as anticipated in Figure 8).<sup>85</sup>

In the case of interacting particles, their spatial distribution in the sample is not random and therefore the spectrum is affected. It is common to consider the spectrum of interacting particles as composed of two terms: the *form factor* ( $F(q)$ ) and the *structure factor* ( $S(q)$ ):

$$I(q) = N F(q) S(q).$$

The form factor is the one describing the shape (and eventually internal structure) of the particles and coincides with the spectrum of non-interacting particles. On the other side, the structure factor refers to the spatial organization of the particles and therefore it can be used to gain information regarding the interparticle interactions. An example is shown in Figure 17c. The scattering of the same, negatively charged, nanoparticles has been measured in ultrapure water and in the presence of salts (it should be stressed that, because of the presence of charged ligands on the surface of the nanoparticles, the counterions are always present, even in the sample dispersed in pure water). The spectrum collected in water shows the signatures of repulsive interaction (positive slope at low  $q$  followed by a peak, due to a conserved interparticle distance). The negative charge of the nanoparticles can be screened by the addition of ions, which decrease the Debye length. As described in section 2.4.2 the values of the Debye length are determined by the valency of the ions. The table containing the list of the values of the Debye length for different concentrations of salts presented in section 2.4.2 is reported here for clarity:

		Salt concentration		
		0	0.1 mM	1 M
Salt	NaCl	960 nm	30.4 nm	0.3 nm
	CaCl <sub>2</sub>	960 nm	17.6 nm	0.2 nm

In agreement with these numbers, the repulsion is less visible in the spectra in the presence of increasing concentrations of salts. Also, 1 mM NaCl and 0.3 mM CaCl<sub>2</sub> show a very similar screening efficiency, in agreement with the predicted value for the Debye length. If the interaction between the particles changes from repulsive to attractive the slope at low  $q$  becomes negative.

In practice, when analyzing the spectrum of particles dispersed in a solvent, they are normally inserted in a capillary to perform the measurement. In this case, to get information about the particles from the spectrum, it is important to remove the contribution to the scattering from the solvent and the capillary. This can be performed easily by simply subtracting the spectrum of the capillary containing only the solvent from the spectrum of the suspension of nanoparticles.<sup>84</sup>

In the case of gold nanoparticles protected by a ligand shell introduced in Chapter 3, the electron density of the gold core is much higher than the one of the ligand shell, which is, instead, comparable to the one of water. Hence, the scattering from the ligand shell is negligible and the form factor is determined by the gold core.

## 4.6 Dynamic light scattering (DLS)

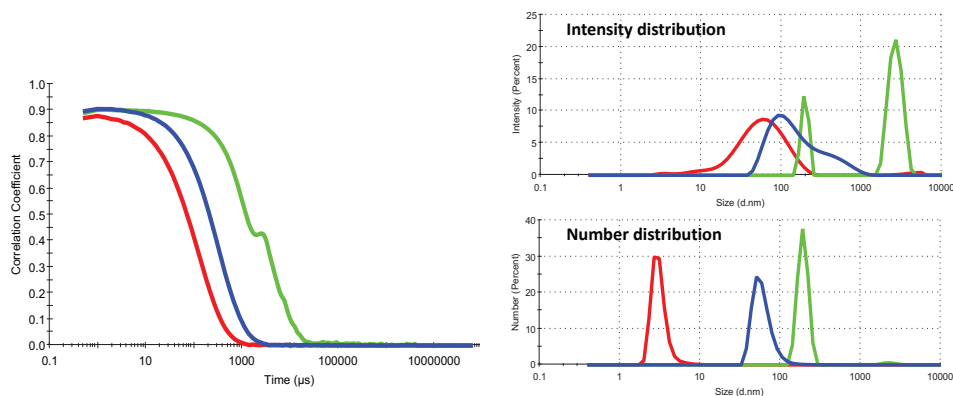


Figure 18 **DLS measurements**. Three examples of DLS data. Smaller particles (red curve) diffuse faster, as visible by the correlation curve. The green curve is an example of a sample containing multiple populations. On the right-hand side the difference between the size distribution based on the scattering intensity and on the number is shown. The fact that larger particles scatter light more efficiently is the reason for the difference between the two plots. The number distribution should be used to calculate the relative ration between the different populations. As an example, in the green curve the micrometric particles scatter a lot of light, but their number is very little.

Dynamic light scattering is a broadly used technique in colloid science to characterize the size of particles and, eventually, their aggregation. It measures the average *hydrodynamic diameter* ( $d_H$ ) of particles in suspension<sup>88,89</sup>, which is defined as the diameter of a sphere that has the same diffusion coefficient as the particle of interest. It is affected by the structures on the surface of the particles, as well as by the presence of ions in solution, since they influence the Debye length (see section 2.4).

Considering that the particles in suspension follow a Brownian motion,  $d_H$  can be calculated by the Stokes-Einstein equation:

$$d_H = \frac{k_B T}{3\pi\eta D}$$

where  $k_B$  is the Boltzmann constant,  $T$  is the absolute temperature,  $\eta$  is the viscosity coefficient and  $D$  is the diffusion coefficient. In a DLS experiment  $d_H$  is derived from a measurement of  $D$ .

In practice, a laser beam is shined through a sample (suspension of particles) and the scattering at a defined angle is measured over time: fluctuations in the scattering intensity, due to Brownian motion, are recorded. Fluctuations are faster in the case of particles that diffuse faster. The autocorrelation function for the fluctuations is calculated, as shown in Figure 18. The correlation is 1 at time 0 and decreases over time, depending on the size of the scattering particles: smaller particles diffuse faster, showing a correlation that decreases at shorter times. In the case of monodispersed particles the correlation drops all of a sudden, while the slope is lower in the case of polydisperse samples.

From the autocorrelation function, the diffusion coefficient can be obtained (knowing the refractive index of the solvent) and the hydrodynamic diameter of the particles can be calculated through the Stokes-Einstein equation, if the viscosity coefficient of the solvent is known. This result is based on the intensity of the light

scattered by particles. Mie theory of light scattering from a sphere predicts that bigger particles scatter more light than smaller particles: the analysis described above is therefore particularly sensitive to the presence of the largest particles in the sample and the distribution can be strongly affected by the presence of dust particles, which normally have a size in the micron range. To solve this problem, if the refractive index and the absorption coefficient of the particles are known the number size distribution can be calculated, by assuming that all particles are spherical and have a homogeneous density. This procedure can be particularly useful in the case of heterogeneous samples: the number distribution allows for the quantification of the number of particles for each  $d_H$ , unbiased by the scattering efficiency. A comparison between the intensity distribution and the number distribution is shown in Figure 18.



# Chapter 5 Measurements of surface energy through AFM force curves

## 5.1 The goal of this project

The ability to map the wettability at the microscale (or even nanoscale) would be beneficial for the optimization of many industrial processes. The ideal quantity to measure, in this case, is the surface energy of the material, since this quantity does not depend on the properties of the solvent used to wet the surface (see section 2.2). However, information somehow similar can be obtained by a map of the work of adhesion of a liquid to a surface, if the properties of the liquid are known (see section 2.3). One possible way to map the work of adhesion at the nanoscale is by using the SAM-AFM technique described in section 4.2.2. This technique has proved to be accurate in the analysis of high-resolution images on homogeneous materials, but cannot be applied to analyze images on the scale of some micrometers containing multiple phases, because in this case the error on the amplitude is too large to allow for the back calculation of the work of adhesion.

The project presented in this chapter has been developed during an internship to BASF (Ludwigshafen, Germany), under the supervision of Dr. Peter Baumann. The goal of the project was the development of an easy to use, straightforward technique, that could be applied on a daily-basis by technicians in the laboratory, to map the surface energy of unknown materials, at the microscale or below.

In the BASF laboratory three Bruker Dimension Icon AFMs are available for the measurement, on which it is possible to operate in PeakForce QNM mode (see section 4.2.1). In this mode a cantilever is oscillated well below resonance resulting in a continuous series of force-distance curves. While keeping the peak force constant by direct force control, different material properties can be extracted and quantified from the force-distance curve at each pixel within an image. This imaging mode is particularly stable (if compared with amplitude modulation) and can be used on different imaging-scales (from nanometric to micrometric scan-sizes). The goal of the project was to check whether from the force curves collected in each pixel of the image the surface energy of the material under investigation could be calculated.

## 5.2 State of the art

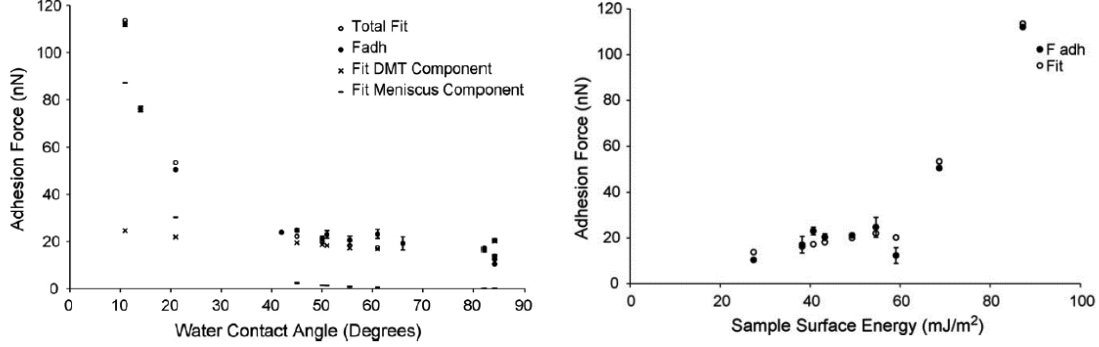


Figure 19 **Summary of the data from Pietak *et al.*<sup>90</sup>** The relationship between the contact angle (left) or the surface energy (right) and the force of adhesion measured by AFM. The data is modeled by decomposing the force into two components: one due to the meniscus and the other one due to DMT adhesion arising from intermolecular attractions. Figures adapted from reference 90, with permission.

In 2007 Pietak *et al.*<sup>90</sup> showed that under atmospheric conditions AFM force curves can be used to locally estimate the water contact angle and surface wettability. This measurement is suitable for complex surfaces that are not easily accessible by the standard contact angle technique.

They measured the force of adhesion on a series of reference samples and plotted the obtained values as a function of the surface energy and the contact angle, as shown in Figure 19. They could successfully fit the obtained data using a model in which the force of adhesion is the sum of two components, one is the adhesion obtained by the Derjaguin-Muller-Toporov (DMT) model of elastic contact, the other one is due to the presence of the water meniscus between the tip and the sample. In fact, the presence of a meniscus is a well-known phenomenon, but there is no established model to describe the force it exerts on the tip. Different empirical expressions have been suggested in the past, Pietak and coworkers chose the one that allowed them to fit better their data:

$$F_{adh} = F_{men} + F_{DMT} = 2\pi R(\gamma_L e^{-b\theta} + 2\sqrt{\gamma_T \gamma_S})$$

where  $\theta$  is the water contact angle,  $\gamma_{S,L,T}$  are the surface energies of the sample, liquid and tip respectively and  $R$  is the radius of the AFM tip. Since in this expression the force of adhesion depends on both  $\theta$  and  $\gamma_S$  and there is no simple relation between those two, the dependence of  $F_{adh}$  on both of them should be fitted simultaneously. By applying this procedure Pietak and coworkers could estimate the surface energy and water contact angle of natural fibers.

## 5.3 Proposed approach

The results presented by Pietak and co-workers show that, on average, the adhesion force is higher on samples having higher surface energy and lower contact angle. In principle, one can consider just one of the two trends and fit it with an empirical expression.

To work on this hypothesis, I have collected multiple images on reference samples, using the PeakForce mode. The final outcome of my internship is the protocol described in section 5.4, containing all the necessary imaging parameters. A discussion about the correct operation procedure and the limits of applicability of the protocol follows, in section 5.5.

## 5.4 Protocol

- Material:
  - Relevant sample (from now on called sample)
  - Minimum two (better three) reference samples, of which the surface energy is known (from now on called references). Self-assembled monolayers (SAMs) prepared on template stripped gold on mica as described below have been used. In principle every flat sample with known surface energy can be used as a reference.
  - Cantilever RTESPA-150 (Bruker)

- Experimental Procedure:

### A. Preparation of reference samples

1. Prepare 1 mM solution of thiols in ethanol. (Thiols that have been successfully used in this project are: octadecylmercaptan, 1-undecanethiol, 11-amino-1-undecanethiol hydrochloride, 11-mercapto-1-undecanol, 11-mercaptopundecanoic acid, 1H, 1H, 2H, 2H-Perfluorodecanethiol.)
2. Using the gold evaporator, deposit 90 nm of gold on freshly cleaved mica. The obtained substrate can be kept in ambient conditions for a long time.
3. Cut the substrate in pieces (about 1.5 cm \* 1.5 cm)
4. Stick each piece on a glass slide (previously cleaned with ethanol) using superglue (The gold should be sandwiched between glass and mica). Apply pressure in order to make the glue film as homogeneous as possible. Leave the glue under pressure to dry for minimum half an hour.
5. When the glue is dry, dip the substrate in ultrapure water in a clean petri dish. After one minute of immersion cleave the mica with the help of tweezers. If necessary proceed layer by layer and immerse the substrate again in ultrapure water. After all the mica has been removed dry the substrate with the air gun.
6. Immediately immerse the substrate in the thiol solution and leave it overnight.
7. The next morning rinse the substrate with ethanol and dry it with the air gun.

### B. Measurement of surface energy

AFM (measurements using a Bruker Dimension ICON AFM in PeakForce-QNM operation mode):

1. Mount your cantilever and calibrate the deflection sensitivity and the spring constant.
2. Image Reference1: check in the camera for a nice, flat area, then start imaging. Adjust the setpoint, in order to keep the deformation between 0,5 and 1 nm. Collect three images in three different areas of the reference, to check the degree of homogeneity. Make sure you press the *autoconfig* button in the software after you have adjusted all the parameters and before the collection of the image. It is recommended to calculate the average force of adhesion immediately after the image has been collected, to have an idea in real time of eventual changes in the tip status. Example of a set of parameters: scan size 250 nm, scan rate 0.8 Hz, PeakForce amplitude 50 nm, PeakForce setpoint 1 nN, Aspect ratio 1 - 3, PeakForce frequency 2 Hz. If on a 250 x 250 nm or 500 x 500 nm a color scale of 5 nm is not enough for the eight channel it means that the imaged area is too rough: move to a different area.
3. Image the sample: adjust the setpoint, in order to keep the deformation between 0,5 and 1 nm. If the sample is composed of areas with different stiffness, multiple set points will be necessary.
4. Repeat the instructions reported in step 2. If the values you obtain are the same as before, move to the next steps, otherwise the tip has changed: change the tip and restart from step 1.
5. Image Reference2, with the same procedure described in step 2.

6. Repeat step 4.
7. Image Reference3, with the same procedure described in step 2
8. Repeat step 4. In this case, even if the tip has changed you can still get a surface energy value for your sample (using the adhesion values collected in points 1 – 6).

#### C. Measurement of surface energy through contact angle

Measure the surface energy of the samples with as many drops as possible using water, diiodo-methane and ethylene glycol on the exact same sample that has been used for the AFM measurement. The drop shape can be fitted either to an ellipse or to a sphere, to obtain the best fitting results. Calculate surface energy using the Owens and Wendt model (section 4.1).

#### D. Data Analysis

Calculate the average force of adhesion on each reference and on the sample.

Fit the force of adhesion vs surface energy points for the references to a line (get the angular coefficient  $m$  and the intercept  $q$ ).

Calculate the surface energy for the sample, according to the following formula:

$$\gamma_s = (F_{adh} - q)/m$$

### 5.5 Applications and limitations

One of the key points of the just presented protocol is the fact that sample deformation should be kept constant during the measurement on all the samples that need to be compared. In fact, a difference in sample deformation implies a difference in the area of contact between the tip and the sample, making impossible any comparison between different data points. An alternative approach would require the knowledge of the effective radius of the tip, and a normalization of the measured force of adhesion by the area of contact. Ideally, the deformation should be kept as small as possible, in order to assure an elastic response of the material. The range 0.5 - 1 nm has been selected in order to enable stable imaging conditions on a variety of samples.

The key observation for the development of the protocol is that the force of adhesion varies linearly with the surface energy (Figure 20). This is consistent with the findings of Pietak *et al.* because the materials I have used have a surface energy smaller than 60 mN/m and the data from Pietak *et al.* look linear in this range of surface energy. It should be stressed that the parameters of the

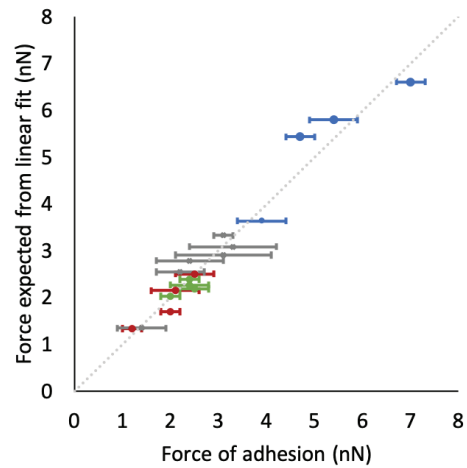


Figure 20 **Visual evaluation of the quality of the linear fit for all the experiments performed with more than three reference samples.** Different measurements (corresponding to different tips being used) are plotted with different colors. For each experiment the  $\gamma_s$  vs  $F_{adh}$  curve has been fitted linearly. The obtained angular coefficient and intercept have been used to predict the expected force of adhesion, knowing the surface energy of the sample. If the assumption of linearity is correct all the points should sit on the dotted line in this plot. In fact, almost all the experimental error bars overlap with the dotted line, confirming the validity of the fit. The plot is also showing the effect of the tip on the measurement: in total six reference samples have been used. All of them have been measured in the experiment reported in grey, a subset of them has been measured in the other cases. In the blue case, the force is systematically higher than in the other cases. This can be due, for example, to a less sharp tip, which has a larger surface of contact.



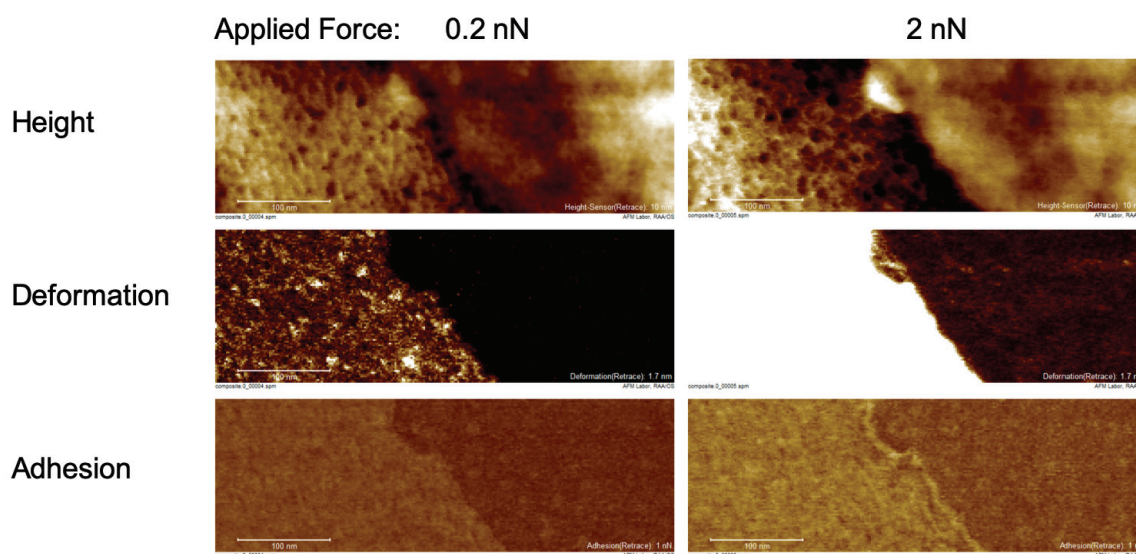


Figure 21 **Measurement of the surface energy of a multicomponent system.** Two images have been obtained with a different set of parameters in order to have the same average deformation in the two cases on the two different components. The applied force is different in the two cases, the color-scales are the same (the difference between black and white is reported on the bottom-right corner of each image). Lower force is needed to measure the component on the left of each image, since it is softer.

linear dependence are influenced by the tip: when using different tips, different values are obtained for the slope and the intercept of the  $\gamma_S$  vs  $F_{adh}$  line. For this reason, the protocol for the measurement of the surface energy by AFM requires the measurement of the adhesion force on reference samples.

Once the parameters of the linear fit have been calibrated for the tip in use, an unknown sample can be characterized. At this point, thanks to the use of the PeakForce mode, it is straightforward to get a map of the surface energy of a multicomponent system. Care must be taken to keep the deformation constant, as mentioned in step 3 of the protocol. In the case of samples composed of two components with very different stiffness (as in the example reported on Figure 21), this requires the collection of multiple images: in the first one the setpoint needs to be optimized in order to have a deformation between 0.5 and 1 nm on the first component, in the second image the optimization of the setpoint should be done on the second component. The force of adhesion should be analyzed for each component on the image that has been optimized for it.

This method has shown to be reliable and could be applied to measure the surface energy of a nanoscale gold surface.<sup>91,92</sup> However, it presents an important limitation: since the meniscus is involved in the measurement of the force and its formation is strongly affected by the humidity in the vicinity of the sample, it is critical to work in an ambient with controlled, or at least constant, humidity. The experimental setup should be properly designed to avoid artifacts in the measurement due to changes in the weather.

In the following table a comparison between the newly developed technique and the SAM-AFM technique described in section 4.2.2 is presented:

	<b>SAM-AFM</b>	<b>New method</b>
<b>Output</b>	work of adhesion	surface energy (eventually contact angle)
<b>Environment</b>	liquid	air
<b>Measurement based on</b>	water structure	contact mechanics and on the formation of the water meniscus
<b>Requirements of the machine</b>	every AFM on which high resolution in liquid can be achieved	Fast and with high resolution on machines equipped with fast force mapping modes. Slow and with lower resolution on every other AFM, by performing regular force maps
<b>Calibration (minimum number of reference samples needed)</b>	1	2
<b>Samples measurable in one day</b>	3	6
<b>Scan size</b>	below 30 nm	whatever (resolution not tested)
<b>Additional requirements for the samples</b>	only hydrophilic samples	tested for surface energies between 10 and 50 mN/m

The possibility to combine the advantages of the two techniques, that is the easiness and stability of the PeakForce, with the advantage of the measurement in liquid, that is not sensitive to external humidity, needs to be further explored.

# Chapter 6 Determination and evaluation of the non-additivity in wetting of molecularly heterogeneous surfaces

## 6.1 Cassie equation and its limitations

The Cassie equation was formulated by Cassie and Baxter in 1944 to describe the wetting of porous surfaces<sup>93–95</sup>. When a drop sits on a porous surface (pores with a size in the micron-range), air is trapped in the pores and so the porous surface is equivalent to a heterogeneous surface composed of two materials, of which one is air. The Cassie equation is therefore used today to describe the wetting of chemically heterogeneous surfaces. It states that the work of adhesion (see section 2.3) on a multicomponent system can be calculated as the average of the work of adhesion of each component:

$$W_{SL} = f_A W_{AL} + f_B W_{BL}$$

where  $f_A$  and  $f_B$  are the surface fractions, respectively of component  $A$  and  $B$  ( $L$  stands for liquid and  $S$  for surface).

Starting from the seventies, an interest in the wetting properties of proteins and complex surfaces has raised. The hydrophobicity of single amino acids has been studied and different hydrophobicity scales have been built to summarize their values. By using the Cassie equation, the overall hydrophobicity of a protein can be estimated by summing the contributions of the amino acids exposed on the surface. Online databases are available to do this kind of calculations.<sup>96</sup>

However, in the last 15 years, several computational studies have appeared suggesting strong effects of neighboring molecules on the interfacial properties.<sup>97–105</sup> In the meantime, experimental evidence of related physical phenomena has been published.<sup>40,41,106–110</sup> In the next sections the main publications questioning the validity of the Cassie equation at the nanoscale will be reviewed.

The main result presented in this chapter is a direct measurement of the non-additivity of wetting properties at the nanoscale, together with the proposition of a non-additive model to predict interfacial properties.

### 6.1.1 Computational studies of water-solid interfaces at the nanoscale

Systematically tuning the properties of heterogeneous surfaces at the nanoscale is very challenging. Computational studies have the advantage that they can in principle access every possible conformation of the surface, including those that cannot be accessed experimentally. Such studies are therefore very useful in this field.

The group of prof. Pablo Debenedetti at Princeton University has been one of the first to address the problem of wetting of heterogeneous surfaces. In 2007 an article was published, addressing the case of water confined between nanoscale surfaces with various patterns of hydrophobicity and hydrophilicity, at different

pressures.<sup>97</sup> The key finding in the article is that, at ambient conditions, the water density on the first hydration layer is considerably higher at a hydrophobic patch surrounded by hydrophilic borders than it is at a purely hydrophobic surface with the same area, highlighting the importance of heterogeneity on hydrophobicity at nanoscopic length scales. The same kind of “hydrophilic invasive” effect is visible in the case of a single hydrophilic molecule in the center of a hydrophobic plate. The conclusion is that the presence of hydrophilic molecules can attenuate the hydrophobicity of neighboring hydrophobic sites. This effect is clearly present on the first hydration layer and quickly disappears in the next layers: only minor differences are visible from the second layer on. Cooling as well as applying high pressure leads to appreciable blurring of the differences in the water densities between different plates.<sup>97,98</sup> The same approach (water confined between nano-surfaces) was used to study proteinaceous surfaces for the first time in 2008.<sup>99</sup> Simulating a flattened protein-surface enabled for the discrimination between wetting phenomena due to the chemical composition on one side from the ones due to the geometrical 3D arrangement of the protein on the other side. The conclusion was that a flattened hydrophobic protein behaves in an intermediate way between an idealized hydrophobic surface and a strongly hydrophilic one. Correspondingly, cavitation is only seen in a very local region of the interface and at short separations approaching the limit of steric accessibility to the solvent.

The group of prof. Shekhar Garde has also been very active in the study of patterned surfaces, pursuing the final goal of understanding and predicting the wetting properties of proteins and biomolecules. Interestingly, while the analysis of Debenedetti focuses on the density of water in the first hydration layer, Garde prefers to characterize the hydrophobicity of a surface by looking at the fluctuations in the density of interfacial water.<sup>100</sup> Despite the difference in methodology, the two approaches lead to the same conclusions: Garde’s simulations show that a single -OH group in a -CH<sub>3</sub> terminated self-assembled monolayer has a more dramatic effect on water in the vicinity compared to that of a single -CH<sub>3</sub> group in an -OH background. For mixed monolayers, this asymmetry leads to a non-linear dependence of hydrophobicity on the surface concentration.<sup>101</sup> Moreover, -CH<sub>3</sub> terminated self-assembled monolayers with an insertion of a fixed number of -OH terminated ligands, display a significantly different strength of adhesion with water, depending on the geometrical arrangement of the ligands. Specifically, -OH groups reduce the overall hydrophobicity more effectively when they are separated by one -CH<sub>3</sub> group. Lower efficiency is observed for -OH clustered together or further apart.<sup>102</sup>

In all the studies reported until here, model surfaces are designed. The simulations assume the surfaces to be fully immersed in water and the water structure at the molecular level is analyzed. A completely different approach to this problem is the one proposed by Wang *et al.*<sup>103</sup>: after designing a model surface they simulate a nanodroplet of water (containing at least 2000 molecules) sitting on it and computationally measure the contact angle. Multiple simulations are performed on idealized surfaces with different concentrations of polar and nonpolar molecules as well as on proteinaceous surfaces. Deviations from the linear dependence of the work of adhesion on the composition of the surface are observed. In the case of idealized surfaces with moderately polar components the linear trend could be restored by considering the composition of the solvent accessible surface rather than the projection of the surface. In the case of prototypical biological surfaces, with irregular patches and strongly contrasting polarities between water and the surface sites, no way could be found to predict the deviations from the linear behavior.

A similar approach was used by Nguyen *et al.*<sup>104</sup> to predict the nanoscale contact angle on striped surfaces composed of gold and silver. In agreement with the studies discussed above, they found that Cassie equation

is not valid at the nanoscale, with a strong influence of the more hydrophilic compound on the total hydrophilicity.

To the best of my knowledge, today, no predictive model exists for the wetting of heterogeneous nano-surfaces and the characterization of the context-dependent hydrophobicity at nanoscale resolution is still a nontrivial task. Up to date, the only solutions existing to predict the hydrophobicity of a protein, without using additive assumptions, consist in the simulation of the water structure around it. As an example, Garde's group suggests to map the hydrophobicity of a protein by estimating the free energy associated to cavity formation near the surface, with more favorable values suggesting the presence of an hydrophobic site.<sup>105</sup>

### 6.1.2 Experimental studies of water-solid interfaces at the nanoscale

To the best of my knowledge, there is no experimental evidence directly supporting the theoretical claims described in the previous section. However, many groups recently published the observation of some phenomena that indirectly confirm what has been predicted by theoreticians.

One of the first experimental papers on the topic was published in 2008 by our group. The solubility of gold nanoparticles coated with a phase separated mixture of ligands was tested in 12 different solvents. The key finding of the study was that, for some of the solvents tested, the saturation concentration did not depend linearly on the composition of the ligand shell. This observation was thought to be associated with steric constraints, but no predictive theory was developed at that time. Also, at that time there was no suggestion for what was the discriminant between solvents that showed a linear dependence and solvents that did not show it.

One year later, using similar nanoparticles, our group could also show that the solid-liquid work of adhesion does not depend linearly on the composition of the ligand shell, if patches smaller than 2 nm are exposed on the surface.<sup>41</sup> In this case the measurement was performed by contact angle and atomic force microscopy (see sections 4.1 and 4.2.2). Bradford *et al.*<sup>106</sup> recently confirmed the observed non-linear dependence of overall hydrophobicity on linear composition, by using, instead, Langmuir films of core-shell gold nanoparticles.

It should be stressed that in the three studies discussed above the morphology of the ligand shell is not known. All the studies observed a non-linear dependence of wetting-related properties on the ligand composition, but the effect of different arrangements of the ligands cannot be inferred from the results, because two parameters (composition and shell morphology) are changed at the same time.

An opposite approach (fixed composition with different arrangement) is used in a study by Ling *et al.*<sup>107</sup>: two polymeric membranes (composed of Nafion) with an identical chemical composition, are shown to interact differently with water. The water structure is characterized by CARS (coherent anti-Stokes Raman scattering spectroscopy), which is a nonlinear analogue of Raman spectroscopy. The difference is supposed to be due to different nanoscale physicochemical properties, such as the distribution of the hydrophilic  $\text{SO}_3^-$  groups on the surface, but also the size and shape of the water channels in the polymeric material. Again, as in the previous cases, more than one parameter is changed at once: this time being the three-dimensional geometry of the surface (roughness and distribution of the channels) and the arrangement of the hydrophilic groups on the surface.

Other experimental approaches have focused more on the effects of the vicinity of charges and hydrophobic groups.

Ma *et al.*<sup>108</sup> published, in early 2015, unexpected results on the modulation of hydrophobic interactions by ions immobilized on the surface as far away as one nanometer. These results demonstrate the importance of nanometer scale chemical heterogeneity on wetting properties and suggest that hydrophobicity is not an intrinsic property of a non-polar domain, but it is strongly modulated by neighboring molecules.

A few months later Chen *et al.* published a complementary result<sup>109</sup>: ionic interactions in the vicinity of an hydrophobic surface are modulated by their sub-nanoscale distance from the surface itself. In other words, the distance of a charged domain from a hydrophobic domain influences the strength of the electrostatic interactions in which the charged domain can be involved.

The vicinity of charged and hydrophobic domains is common on the surface of proteins, this is why both these results are useful to understand phenomena such as the large shifts in  $pK_a$  values observed for amino acids in folded proteins.<sup>110</sup>

### 6.1.3 The goal of this project

As discussed in the previous sections, the fact that the arrangement of molecules on a surface at the nanoscale affects the wetting properties has been predicted by many computational studies and indirectly proven experimentally. However, the technical difficulty to prepare two systems identical in chemical composition and differing only on the arrangement of the molecules prevented a direct measurement of this phenomenon.

The goal of the project described in this chapter is to have, for the first time, a direct measurement of the effect of molecular arrangement on the water structure at the interface (and hence on the wetting properties). For this reason, a model system has been synthesized. The wetting properties have been measured with three different techniques and, finally, a theoretical model has been derived to predict interfacial properties on the molecular level.

The results of this project are described in detail in a paper appeared on PNAS in 2019.<sup>1</sup> My contribution to the work is in the experimental characterization of the water structure (by SFG, contact angle and atomic force microscopy) and in the experimental validation of the proposed model (by contact angle measurements with a variety of solvents). I have contributed to the design of the experiments and the data analysis and interpretation in view of the development and validation of the new model. I will focus in this chapter on the methodology used, the results obtained and their interpretation, without reporting the whole “materials and methods” section from the paper. The interested reader is referred to the main publication.

## 6.2 A model system to study the effects of chemical heterogeneity on interfacial properties

The ideal model system for this study is composed of a set of two materials, having the exact same chemical composition, but different (and known) arrangement of the molecules on the surface.

Our group has previously shown that it is possible to synthesize gold nanoparticles with a mixed-ligand shell out of equilibrium. A thermal treatment (*annealing*) allows to bring the ligand shell to equilibrium.<sup>35,111</sup> Basically, this means that the patches on the ligand shell evolve upon thermal treatment and the particles before and after annealing expose a surface that has the same composition but a different morphology. A system prepared in this way is ideal for our study.

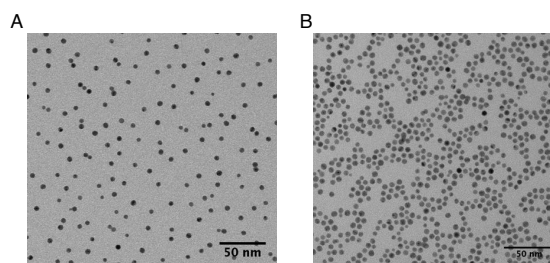


Figure 22 **TEM images of the nanoparticles** before (A) and after (B) annealing. Based on the counting of more than 500 nanoparticles, the distributions of the core diameter are found to be  $5.1 \pm 0.6$  nm and  $5.2 \pm 0.7$  nm for nanoparticles before and after annealing, respectively. Figure reused from reference 1, with permission.

For this reason, we have used nanoparticles coated with a 1:1 binary mixture of 3-mercaptopropionic acid (MPA) and 1-octanethiol (OT). In this way it is possible to have a ligand shell exposing hydrophilic (MPA) and hydrophobic (OT) patches. Particles covered with the same pair of ligands showed, previously, non-linear dependence of the solubility limit from the composition<sup>40</sup> and they were, therefore, expected to have a non-additive solid-liquid work of adhesion ( $W_{SL}$ ). A big batch of nanoparticles was synthesized, with the ligand shell out of equilibrium. Part of it was subsequently annealed in order to change the morphology of the patches.

Both nanoparticles were characterized, to make sure that the only difference between them was the morphology of the ligand shell. As visible in Figure 22 and Figure 23A the annealing does not affect the core size. NMR and TGA confirm that the two sets of nanoparticles have the same average ligand composition and ligand density (Figure 23B and C). Infrared spectroscopy confirms that the protonation of the MPA ligand is the same in the two cases (both spectra show only a peak at  $\sim 1,600$   $\text{cm}^{-1}$  corresponding to the asymmetric stretching of the deprotonated carboxylic group, Figure 23D).

Contrarily to all the previously mentioned techniques, clear differences between the two nanoparticles are visible in the SANS spectra (Figure 23E). In the low  $q$  region the spectra collected before and after annealing overlap, confirming that the two particles have the same core size. At higher  $q$ , the scattering curves do not overlap with each other, showing that the ligand shell is different in the two cases. By simultaneously fitting two spectra of the same particles collected in two different solvents the models shown in Figure 23F have been derived. The most stable conformation for these nanoparticles is the one obtained after annealing, showing thinner, stripe-like, patches. For this reason, from now on, the particles before annealing will be named *patchy* and the ones after annealing *stripe-like*. By quantifying the characteristic length scales of the patches from the SANS modeling, we find that the average MPA domain thickness is  $2.1 \pm 0.6$  nm for the patchy nanoparticles and  $1.3 \pm 0.3$  nm in the stripe-like case.

A confirmation of the differences in the shell morphology before and after annealing can be obtained by SFG. In fact, one can use this technique to measure the degree of order of the molecules in the ligand shell (see section 4.3, in particular Figure 14). The ligand MPA in this case is deuterated and only the conformation of the OT is probed. The SFG spectra (Figure 24) collected on films of nanoparticles drop-casted on a  $\text{CaF}_2$  surface (and immersed in  $\text{D}_2\text{O}$ , as shown in Figure 25A) display a different relative amplitude of the two modes between  $2800$  and  $2900\text{ cm}^{-1}$  indicating that the average ligand conformation on the nanoparticles is different. The stripe-like nanoparticles have less stretched OT chains in the ligand shell. This is compatible

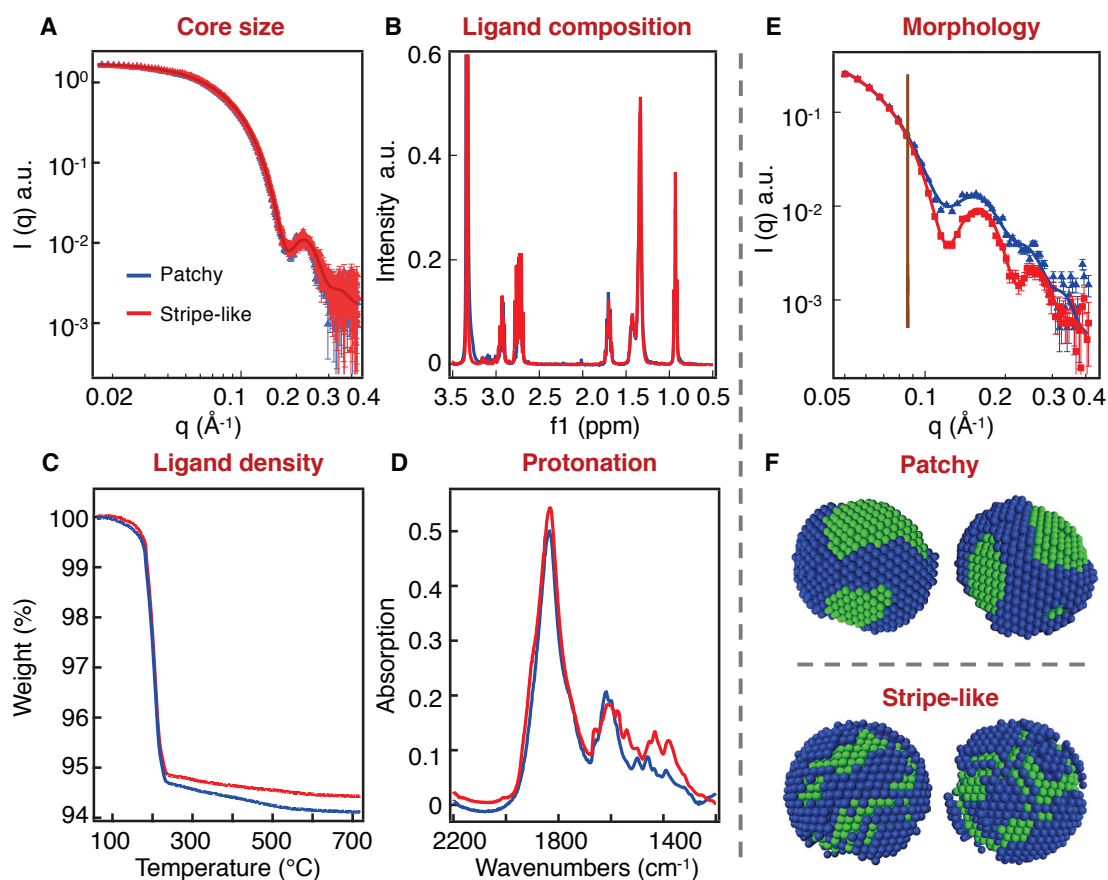


**Figure 23 Characterization of the MPA-OT nanoparticles.** In all plots the blue and red lines refer, respectively, to nanoparticles before and after annealing. Note that for all measurements but SANS the two curves practically overlap with each other. (A) SAXS data on both nanoparticles measured using ethanol as solvent. A fit, assuming a Gaussian distribution of the size, gives a core diameter of  $4.9 \pm 0.6\text{ nm}$ . (B) NMR spectra of the ligands detached from the core via an iodine decomposition. The measured ligand ratio is approximately  $\text{MPA:OT} = 55:45$ . (C) TGA plots for both particles showing that the ligand density is unaffected by annealing. Note that in TGA the experimental error is considered to be larger than 5%. (D) Fourier transformed infrared spectroscopy (FTIR) measurements taken from nanoparticle films in attenuated total reflection mode. The spectra show that MPA ligands are mainly deprotonated on both nanoparticles. (E) SANS spectra of nanoparticles taken in tetrahydrofuran- $\text{d}_8$ . The overlap in the low- $q$  region (below  $0.083\text{ \AA}^{-1}$  corresponding to the overall size of the nanoparticles in real space, as indicated by the vertical line) shows that the two nanoparticles have the same radius of gyration. The scattering at higher  $q$  range is the only characterization that shows a significant difference for the two nanoparticles, indicating a difference in the shape of nanoparticles (i.e. patchiness of the ligand shell). (F) Low-resolution models for the nanoparticles obtained by fitting the curves shown in D and the ones collected in chloroform- $\text{d}$  (dots are the experimental measures, and lines are the fits). In the SANS model, the blue beads stand for OT ligands while the green ones are MPA ligands. We should point out that the nanoparticles characterized in A, D and E are coated with OT and a deuterated version of MPA, for technical requirements of the techniques used. These nanoparticles are identical to the ones described in the other panels. Figure reused from reference 1, with permission.



with the SANS model because more degrees of freedom for the arrangement of the chains are available if the patches are thinner (the ligands are less packed), while OT chains are more ordered if patches are bigger because the alkyl chains interact with each other via hydrophobic interactions.

To summarize, all the characterizations performed confirmed that these two nanoparticles are exactly the same except for the arrangement of the ligands in the ligand shell. They are therefore a perfect model system for our study. Every detectable difference in the water structure around them can be, in fact, associated with the arrangement of molecules in the ligand shell.

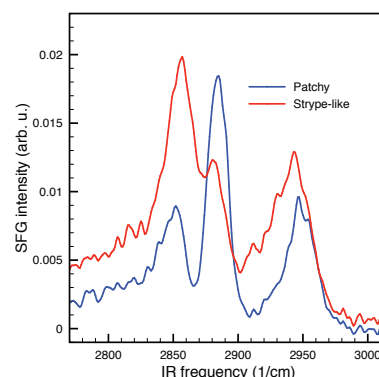


Figure 24 **SFG spectra for the nanoparticles (CH region)**. The amplitude ratio of the symmetric methylene ( $\sim 2850\text{ cm}^{-1}$ ) and the symmetric methyl ( $\sim 2880\text{ cm}^{-1}$ ) stretch vibrational modes are significantly different for the patchy and stripe-like particles.

### 6.3 Experimental measurements of the water structure

Once the characterization of the nanoparticles was done, we could move on to characterize the water structure around them.

SFG spectroscopy was used to characterize the time-averaged structure of interfacial water around the nanoparticles. Films of nanoparticles were produced on clean  $\text{CaF}_2$  surfaces by drop-casting.  $\text{D}_2\text{O}$  was added in the cuvette and the spectra of the interfacial water were recorded. The setup is schematically represented in Figure 25, together with all the spectra collected. The spectra have two main features: a peak at  $\sim 2,375\text{ cm}^{-1}$  and a peak at  $\sim 2,530\text{ cm}^{-1}$ , corresponding respectively to interfacial water that have stronger and weaker hydrogen bonds. The ratio between the two peaks is the relevant outcome for the measurement: it tells that the hydrogen bonding network around the two nanoparticles is significantly different. In the case of stripe-like nanoparticles the ratio of the  $2,530\text{ cm}^{-1}$  band to the  $2,375\text{ cm}^{-1}$  band is larger than that for the patchy nanoparticles. An oversimplified interpretation of these data is that water molecules are less structured near the stripe-like nanoparticles than near the patchy ones.

Once the difference in the water structure was determined we moved on to check whether this difference would lead to a difference in the work of adhesion for the two nanoparticles.

We measured the contact angle of water with films of nanoparticles deposited on glass slides. To avoid artifacts due to uncomplete formation of the layer of particles, for every sample we deposited multiple-layers of nanoparticles (by the Langmuir-Blodgett technique). The work of adhesion was calculated from the contact angle data by the Young-Dupré equation, using  $72\text{ mN/m}$  for the surface tension of water. The values obtained are reported in the following table. The error reported on the contact angle is the standard deviation of the measured values, while the error on  $W_{\text{SL}}$  is obtained by propagating the one on the contact angle.

Sample	Contact Angle	Work of adhesion ( $W_{SL}$ )
Patchy nanoparticles	$76 \pm 3^\circ$	$89 \pm 4$ mN/m
Stripe-like nanoparticles	$85 \pm 3^\circ$	$79 \pm 4$ mN/m
MPA nanoparticles	$38 \pm 1^\circ$	$128 \pm 1$ mN/m
OT nanoparticles	$106 \pm 5^\circ$	$52 \pm 6$ mN/m

To make sure that the roughness of the surface did not influence the results obtained by contact angle we decided to cross-validate the measurement by the AFM technique described in section 4.2.2. It should be stressed that this technique is based on different working principles than contact angle measurements, and measures  $W_{SL}$  at the single-nanoparticle level. In order to do that, high resolution images of the nanoparticles need to be collected, such as the representative ones reported in Figure 27. Data analysis was performed on single particles cropped from the images.

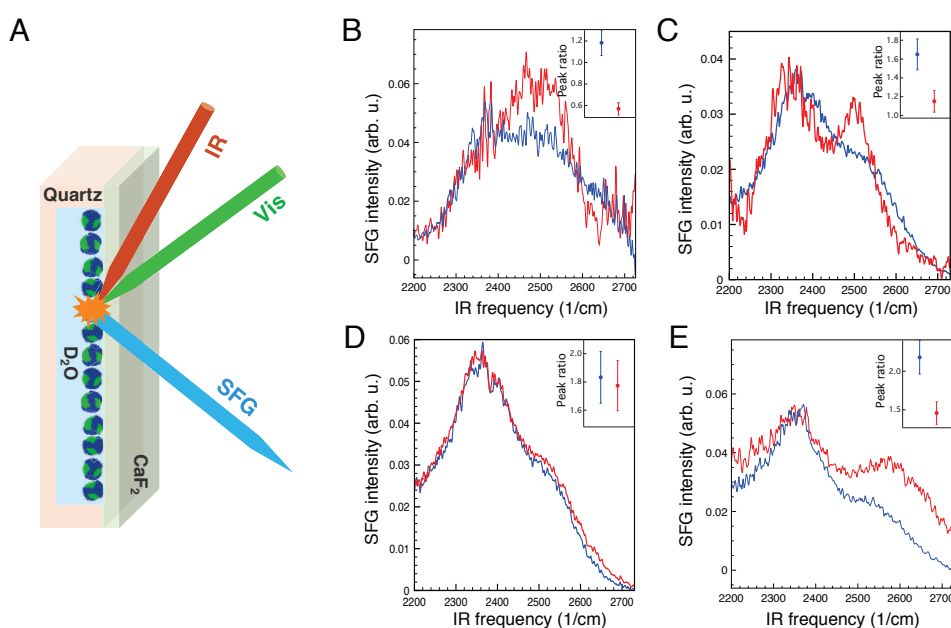


**Figure 25 SFG characterization of the interfacial water structure.** (A) Schematic of the SFG setup. The IR and visible beam are focused on the same spot of the sample. The SFG signal is generated. (B-E) SFG spectra in the water region, as recorded in four different measurements (Blue: patchy nanoparticles, red: stripe-like nanoparticles) and associated amplitude ratio of the peaks due to the strong H-bond and the weak H-bond (insets). To avoid any error from laser fluctuations on different days, we choose to report our data separately. We calculated the peak to peak ratio error of the SFG scattering setup on 10 spectra of different samples of sodium dodecylsulfate stabilized hexadecane nano-emulsions and the deviation from spectrum to spectrum is less than 10 %. This value is used as an error for the values reported on the graph. We have never observed an increase in the ratio of the H-bonds peaks for the annealed sample. The fact that during one experiment (D) we did not observe any difference between the two sets of nanoparticles can be explained by the fact that annealing may not have worked perfectly on that occasion. Since in the formation of the film it is likely that similar nanoparticles will assemble together, it is possible that in this case the laser was focused on an area composed of nanoparticles that were not affected by annealing. All the spectra have been normalized on the peak at  $\sim 2350$   $\text{cm}^{-1}$  to facilitate the visual comparison. Figures adapted from reference 1, with permission.

As described in section 4.2.2, this technique does not provide an absolute measurement, but needs to be calibrated. We used a film of MPA protected gold nanoparticles as a calibration system for the measurement of the  $W_{SL}$  for the patchy nanoparticles. The value of the work of adhesion calculated for these particles was then used as a calibration system for the stripe-like ones.

To get a reliable comparison of different samples (and hence a good calibration), the exact same free amplitude was kept while scanning different samples (differences  $\leq 0.05$  nm where considered negligible), meanwhile the working amplitude was kept as constant as possible. Furthermore, images were compared only if collected in the same day and with the same tip. Each experiment was reproduced twice. A minimum of five nanoparticles per sample were analyzed.

For every experiment the average value of  $W_{SL}$  on different particles and its standard deviation  $\sigma$  was calculated. 5 mN/m were added to each standard deviation in order to consider the error associated with the calibration ( $\sigma^* = \sigma + 5$  mN/m). The average value for different experiments has been calculated and the final standard deviation has been obtained by propagating the  $\sigma^*$  of the single experiments.

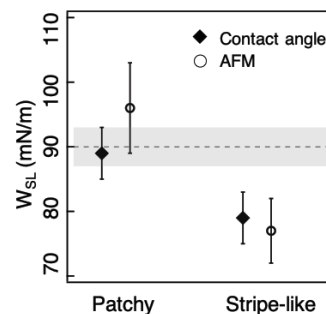


Figure 26  $W_{SL}$  for the two sets of nanoparticles, as measured by two independent techniques. The measurements show significant differences. The dotted line represents the additive average for the  $W_{SL}$  of the two mono-ligand nanoparticles measured using contact angle. The grey band is the error in the measurement of the additive average.

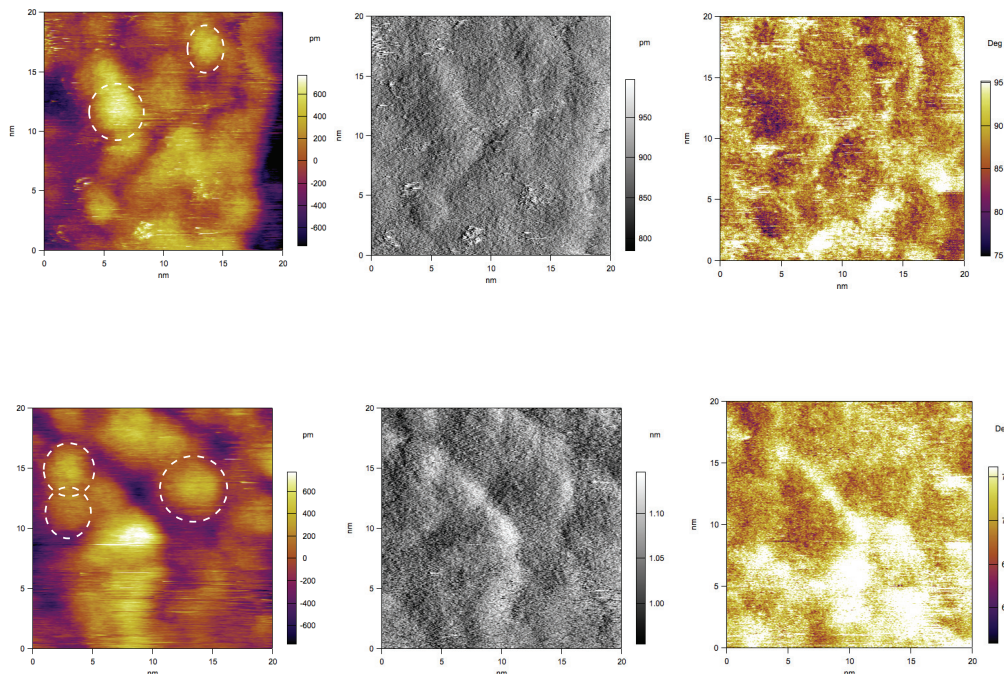


Figure 27 **Representative SAM-AFM images** (from left to right: height, amplitude and phase channels) collected on patchy nanoparticles (top) and on stripe-like nanoparticles (bottom). Circles indicate single particles that have been used for the calculation of  $W_{SL}$ . The value of the free phase of oscillation was  $95^\circ$  for the image on top and  $76^\circ$  for the one on the bottom. Figure reused from reference 1, with permission.

The results obtained are compared to the ones obtained from contact angle in Figure 26. Averaging the results from the two independent techniques we can conclude that the difference between the  $W_{SL}$  on the two nanoparticles is  $15 \pm 7$  mN/m ( $\sim 17\%$  of the expected additive value), the stripe-like nanoparticles being more hydrophobic.

The experimental evidence provided so far shows that the hydrophobicity of the nanoparticles depends on the morphology of the self-assembled monolayer in a nonadditive way, and that the effect is connected to the time-averaged structure of interfacial water.

### 6.3.1 Control measurements on additional sets of nanoparticles

Performing the whole characterization described above for a batch of nanoparticles is a very-demanding task. For this reason, a full set of data have been collected only for one batch of nanoparticles. However, partial sets of data have been obtained on two other batches, confirming the results presented until here. In both cases a detailed characterization of the ligand shell by SANS is missing.

On a second set of MPA-OT nanoparticles with ligand ratio 70:30 (as obtained by NMR) and core size  $4.1 \pm 0.5$  nm (as obtained by TEM) contact angle values have been obtained. These measurements confirm the fact that the wetting of the nanoparticles is affected by the shell morphology (assuming it has changed upon annealing).

Sample	Contact Angle	Work of adhesion
Before annealing	$72 \pm 2^\circ$	$94 \pm 3$ mN/m
After annealing	$83 \pm 1^\circ$	$81 \pm 1$ mN/m
Difference	$11 \pm 1^\circ$	$13 \pm 1$ mN/m

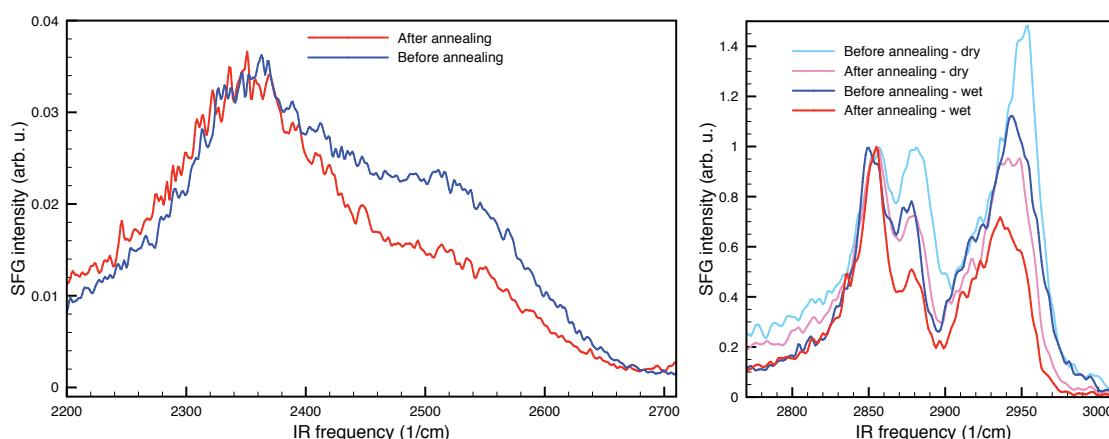


Figure 28 **Additional SFG measurements.** The spectra collected on the frequencies associated to the molecular vibrations of water (left) show a clear difference between the particles before and after annealing. The spectra collected on the CH region (right) show that the morphology of the ligand shell is different before and after annealing (the ligands being more disordered after annealing). An additional measurement has been performed on these nanoparticles: the CH spectra has been collected also in the dry state, showing that the ligands get more disordered when water is added (both before and after annealing). All the water spectra have been normalized on the peak at  $\sim 2350$  ( $1/\text{cm}$ ) to facilitate the visual comparison. The same has been done for the peak at  $\sim 2850$  ( $1/\text{cm}$ ) in the CH case.

On a third set of MPA-OT nanoparticles with ligand ratio 40:60 (as obtained by NMR) and core size  $5.0 \pm 0.5$  nm (as obtained by TEM) SFG measurements have been performed. Figure 28 shows the results of the measurements. Again, the ligands look more disordered after annealing and the water structure on the two nanoparticles is different. These nanoparticles show the opposite trend for the water peaks than the ones described above. Since the ligand morphology is not known an interpretation of such opposite trend cannot be performed.

## 6.4 Computational study of the interfacial properties

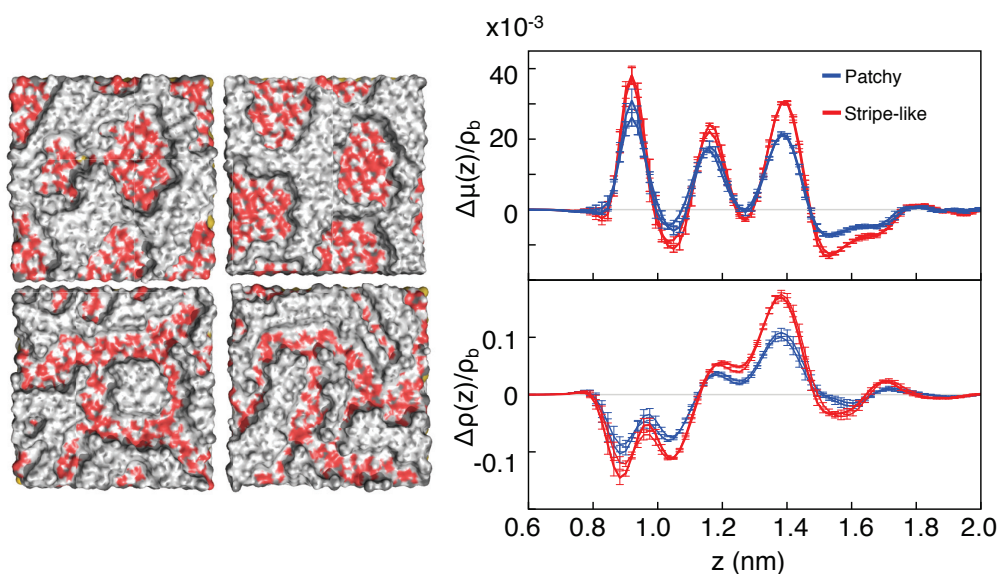


Figure 29 **Molecular dynamic simulations of self-assembled monolayers together with water.** The four simulated surfaces are shown on the left-hand side (red: oxygen, grey: carbon, white: hydrogen). The two surfaces on the top resemble the patchy nanoparticles, while the two on the bottom the stripe-like ones. On the right-hand side the excesses for  $\mu$  and  $\rho$  are plotted. It is clear that the time-averaged structure of interfacial water is influenced by the patchiness.

In order to capture the relationship between the surface morphology and the time-averaged structure of the interfacial water, we performed large-scale molecular-dynamics simulations of self-assembled monolayers composed of mixtures of OT and MPA (in its protonated form) together with water. We generated four configurations (Figure 29) that are consistent with the ligand distributions seen on the patchy (two of them) and stripe-like (the other two) surfaces. It is found that water on top of the patchy and stripe-like configurations exhibits a complex behavior: on average, the water dipoles point toward the surface on top of the MPA patches and lie parallel to the surface on top of the OT patches. The dipoles point out from the surface at the interface between OT and MPA. A larger number of dipoles pointing out from the surface are found on the stripe-like morphology because, in this case, the MPA-OT interfaces are closer to each other.

The integrated dipole orientation density  $\mu$  together with the water density profile  $\rho$  for the four morphologies are then calculated to analyze the surface-induced water ordering. The theoretical  $\mu$  and  $\rho$  profiles based on an additive assumption are also calculated by simulating pure OT and MPA surfaces. The differences between  $\mu$  and  $\rho$  for the surfaces of interest and the ones calculated from the additive assumption are then plotted as a function of the distance from the surface (Figure 29). One can see that the



dipole and density profiles above the surfaces do not follow a purely additive behavior and that there are significant differences between the different morphologies: stripe-like surfaces showing higher deviations from the additive assumption.

## 6.5 Development of a new model

To propose a quantitative model for these non-additive effects, we began by performing molecular dynamics simulations of a series of *trench* configurations corresponding to self-assembled monolayers composed of rectangular OT and MPA regions of varying width. The boundary between the two types of ligand is expected to be responsible for the non-additive behavior. Figure 30 shows the density of water in a cut across trenches of varying sizes, where it can clearly be seen that the structure of water at the boundaries of the trenches is very similar for all trenches that are more than one molecule thick. On the contrary the water density on single-molecule thick trenches is significantly different from the other cases. Overall, these observations suggest that the water density on a ligand is affected primarily by its first-nearest neighbors. However, these systems contain only straight boundaries between ligands of different types, and do not provide an exhaustive list of possible nearest-neighbor configurations, limiting the power of a model based on this kind of systems to predict the results of a general surface.

For this reason, we then generated a set of simulation surfaces in which the ligands in each site were chosen randomly. Assuming that the contribution of a particular ligand to the non-additivity depends only on the identities of its first-nearest neighbors, and treating the long-range structure as a mean field, each ligand on a surface was classified according to the identities and dispositions of its first-nearest neighbors. Figure 31A illustrates, with four examples, the definition of a particular ligand environment. Using the excess terms for

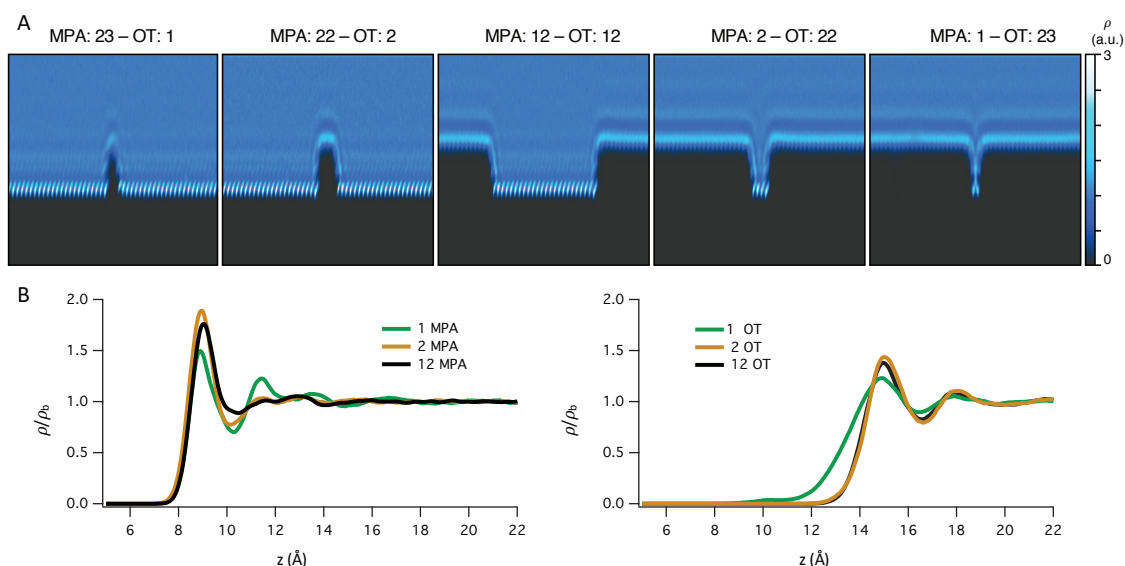


Figure 30 **Molecular dynamics simulations of water on trench configurations.** (A) Water density in a cut across trenches of varying size. Ligands occupy the black area of the pictures (shorter ligands are MPA, longer ligands are OT). (B) Cross-section of the density of water on a cut across the center of the trench. The thickness of each trench is mentioned in the legend (number of molecules). It is visible that, both for MPA trenches and OT trenches, the one-molecule thick trench shows a different density, while starting from trenches composed of two molecules the density on the center of the trench is almost constant. Figure adapted from reference 1, with permission.

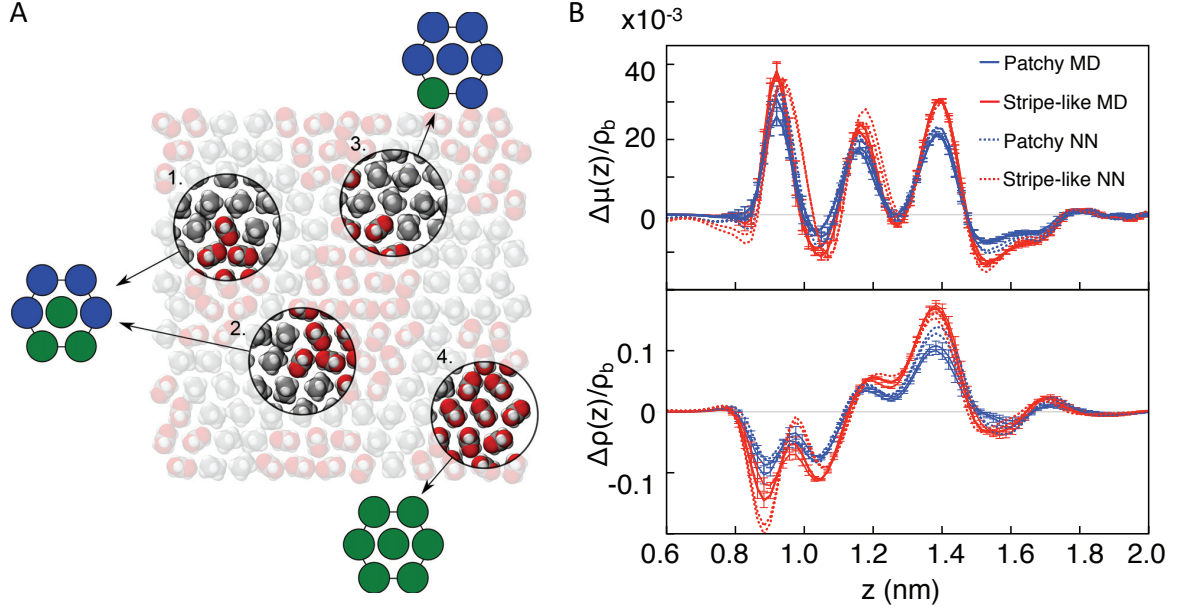


Figure 31 **Nearest-neighbor model**. (A) Classification scheme: patterns 1 and 2 are equivalent by rotational symmetry, with an MPA molecule at the center, surrounded by 2 other MPA molecules next to each other; pattern 3 has an OT molecule at the center with 5 other OT molecules surrounding it; pattern 4 has an MPA molecule surrounded by 6 other MPA molecules, and does not contribute to the excess term. (B) Surface excess  $\Delta\rho$  and  $\Delta\mu$  of the patchy and stripe-like surfaces as calculated from molecular dynamic simulations (MD, continuous line) and by summing the contributions of the nearest neighbors obtained by the linear regression model (NN, dotted line), for the four surfaces.

the density of water and the dipole moment for these randomly generated surfaces, we built a linear regression model, in which an excess quantity for an arbitrary surface is predicted as

$$\Delta f(z) = \sum n_i f_i(z)$$

where  $f = \mu$  or  $\rho$ ,  $n_i$  is the number of ligands of type  $i$ , and  $f_i(z)$  is a function to be fitted. This is analogous to the cluster expansion models that are used to describe the thermodynamic properties of multi-component alloys.<sup>112,113</sup> Here, we use this approximation to model excess terms associated with a particular distribution of ligands. We found, in this way, two important effects. First, the asymmetry between the two ligand types: the excess term associated with a single MPA molecule surrounded by six OT molecules is significantly different from that associated with one OT molecule surrounded by six MPA molecules. The excesses are smaller in the second case, in agreement with what found by Garde and coworkers.<sup>101</sup> Second, the fact that the excess terms are not determined only by the number of nearest neighbors of a certain kind but also on their arrangement (with patchy patterns usually being associated with smaller excesses).

Figure 31B shows the predictions of this model for the surface excesses of the patchy and stripe-like systems. The good match between the excess values resulting from the simulations with the ones resulting from the predictions derived from the new equation indicates that the first nearest neighbors are sufficient to determine the excess term associated with a single molecule in the self-assembled monolayer.

Therefore, we expect the work of adhesion between the surface and a solvent not to be affected by the surface heterogeneity when the solvent molecules are larger than the intermolecular distance in the self-

Table 1 Values of surface tension, density, molar weight, effective volume ( $V_{\text{eff}}$ ) and measured contact angle ( $\theta$ ) of various solvents on the two nanoparticle films.

Solvents	Surface tension (mN/m)	Density (g/ml)	Molar weight (g/mol)	$V_{\text{eff}}$ ( $\text{\AA}^3$ )	$\theta_{\text{Patchy}}$ ( $^\circ$ )	$\theta_{\text{Stripe-like}}$ ( $^\circ$ )
Water <sup>22</sup>	72.8	1.00	18.0	30.0	$70.1 \pm 2.7$	$78.6 \pm 2.9$
Dichlorobenzene <sup>22</sup>	33.6	1.31	147.0	187.0	$30.8 \pm 0.8$	$36.1 \pm 2.0$
Chloroform <sup>22</sup>	27.5	1.49	119.4	133.0	$16.6 \pm 1.7$	$16.8 \pm 2.4$
Ethylene glycol <sup>22</sup>	47.7	1.11	62.1	92.6	$52.2 \pm 2.3$	$64.9 \pm 3.3$
DMSO <sup>22</sup>	44.0	1.10	78.1	118.0	$44.7 \pm 3.8$	$52.0 \pm 3.7$
Perfluorodecalin <sup>114</sup>	19.0	1.91	462.1	402.3	$25.0 \pm 1.3$	$27.7 \pm 3.0$
5CB <sup>115</sup>	27.9	1.00	249.4	411.0	$46.3 \pm 2.2$	$50.0 \pm 1.8$
Glycerol <sup>22</sup>	63.4	1.25	92.1	122.4	$71.2 \pm 4.1$	$87.2 \pm 4.5$
Hexadecane <sup>114</sup>	27.5	0.77	226.4	486.6	$14.7 \pm 2.2$	$25.5 \pm 2.6$
Isopropanol <sup>22</sup>	23.0	0.79	60.1	127.2	0	$6.8 \pm 3.3$
Formamide <sup>116</sup>	58.9	1.13	45.0	66.0	$46.1 \pm 2.0$	$51.6 \pm 2.7$
Perfluorohexane <sup>114</sup>	11.7	1.67	338.0	336.4	$4.8 \pm 1.4$	$5.8 \pm 2.6$

assembled monolayer (because, in this case, a single solvent molecule interacts with more than one molecule on the surface at the same time). To test this prediction, we measured  $W_{\text{SL}}$  for the films of nanoparticles described above for a series of solvents. Every time a new film was produced, its contact angle with water was measured, to make sure the roughness was constant and not affecting the measurement. All the contact angle data, as well as the solvent properties, are listed in Table 1 ( $\theta=0^\circ$  is approximated for solvents that wet almost completely the nanoparticle film).

As reported in Table 1 and shown in Figure 33A, some solvents have the same  $W_{\text{SL}}$  for the patchy and stripe-like nanoparticles, while others behave as water, showing different  $W_{\text{SL}}$ . To rationalize these results along the lines of our new model, we calculated the effective molecular volume ( $V_{\text{eff}}$ ) of all the solvents by dividing their molecular weight by the product of the solvent density and the Avogadro number. We plotted the differences in  $W_{\text{SL}}$  ( $\Delta W_{\text{SL}}$ ) against  $V_{\text{eff}}$  and the results were striking (Figure 33B). Solvents whose  $V_{\text{eff}}$  is above  $\sim 125 \text{ \AA}^3$  (corresponding to an effective diameter of  $\sim 6 \text{ \AA}$ , comparable with the intermolecular distance in the self-assembled monolayer, which is  $\sim 5 \text{ \AA}$ ) show a  $\Delta W_{\text{SL}}$  that is almost independent of  $V_{\text{eff}}$  and smaller than 5%. Solvents with  $V_{\text{eff}}$  below  $\sim 125 \text{ \AA}^3$  have larger  $\Delta W_{\text{SL}}$  with large variations among them. These results confirm the predictive power of our model. We have tried to correlate the large variations at low  $V_{\text{eff}}$  to the properties of the solvents to no avail. The most likely explanation is that  $W_{\text{SL}}$  is affected by many properties of the solvent



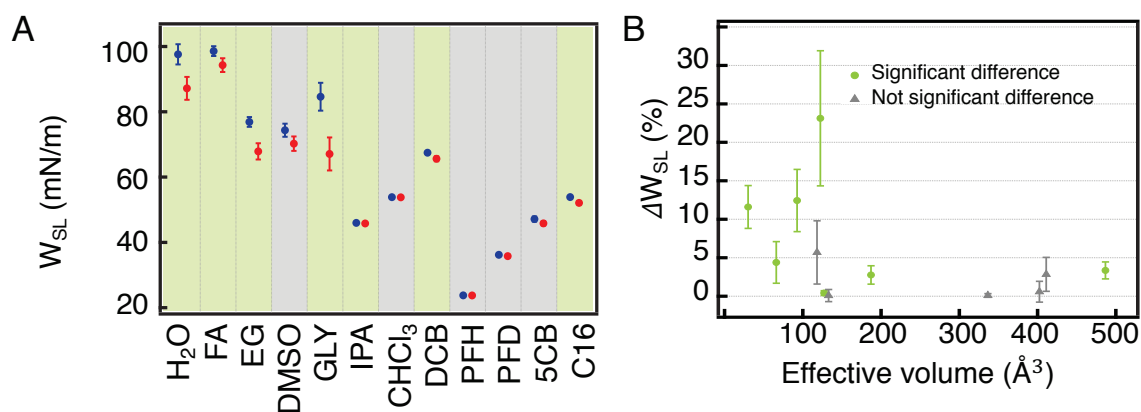


Figure 33 **Experimental validation of the proposed model.** (A)  $W_{SL}$  values of the patchy (blue) and stripe-like (red) nanoparticles in various solvents. The green shadings indicate solvents in which the  $W_{SL}$  shows significant differences (Student's  $t$  test assuming equal variances,  $P = 0.05$ ) for the 2 nanoparticles. The grey shadings indicate that the null hypothesis ("the 2 nanoparticles have the same work of adhesion") cannot be rejected. (The solvents used are: water (H<sub>2</sub>O), formamide (FA), ethylene glycol (EG), dimethyl sulfoxide (DMSO), glycerol (GLY), isopropanol (IPA), chloroform (CHCl<sub>3</sub>), dichlorobenzene (DCB), perfluorohexane (PFH), perfluorodecalin (PFD), 4-Cyano-4'-n-pentylbiphenyl (5CB) and hexadecane (C16).) (B) Dependence of the differences in  $W_{SL}$  for the two films on the effective volume of the solvent molecules. The color of the points is the same as the one of the shadings in (B) and relates to the significance of the differences in  $W_{SL}$ . Figures adapted from reference 1, with permission.

(such as its polarity, polarizability, etc.) but thus far we could not find a single predictive property for its magnitude.

To further confirm our hypothesis on the size of the molecules of the solvents, we have reviewed previously published data<sup>40</sup>, where the saturation concentration of nanoparticles similar to the ones studied here was evaluated in a large number of solvents. As discussed in section 6.1.2, this study reported a non-monotonic dependence of the solubility limit on the ligand shell composition for a subset of solvents, while another subset provided solubility data that could be simply explained in terms of average hydrophobicity of the ligand shell of the nanoparticles. The paper provided no explanation on whether a solvent was part of one or the other subset. Re-evaluating those data, we find that the subset of solvent that showed a non-monotonic dependence of the saturation concentration on the composition of the ligand shell are those having  $V_{eff}$  smaller than  $\sim 130$  Å<sup>3</sup>, in agreement with our new  $W_{SL}$  data and proposed explanation (Figure 32).

## 6.6 Conclusions and outlook

We measured the work of adhesion and time-averaged structure of interfacial water on two sets of nanoparticles differing only for the arrangement of the ligands in the ligand shell. The measurements presented in this chapter prove that the local arrangement of surface groups plays a crucial role in the determination of the solid-liquid work of adhesion and consequently of the surface wetting properties of the surface. Thanks to molecular dynamics simulations a predictive model for the interfacial properties is presented, it shows that wetting can be estimated with a sufficient degree of precision by considering for each molecule on the surface also its nearest-neighbors.

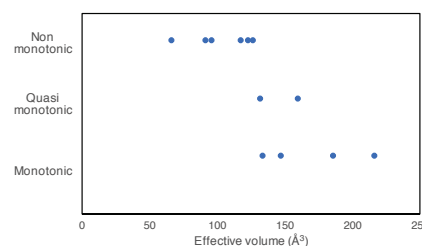


Figure 32 **Re-analysis of the saturation concentration of similar MPA-OT nanoparticles** as previously reported<sup>40</sup>. The solvents are classified into three categories depending on whether the nanoparticles show monotonic dependence of the saturation concentration on the ligand shell composition. The solvents are then ordered according to their effective volume ( $V_{eff}$ ). In general, solvents that show non-monotonic saturation concentration have smaller  $V_{eff}$ , while solvents that show a monotonic trend for the saturation concentration have larger  $V_{eff}$ . Figures adapted from reference 1, with permission.

Extending these findings to more complex scenarios, such as biological systems and proteins, requires significant challenges both at the experimental and theoretical level. The addition to the model of a term associated with long-range structures on the surface (which are now included as a mean-field) could be a possible first step. Moreover, complex surfaces are composed of a large number of components, while in our model system there are only two components. We believe the approach proposed here could be easily extended to the description of multicomponent surfaces, the only problem being the huge amount of computing resources required and the associated large number of experimental data needed to validate the calculations.

To summarize, the concepts and techniques introduced here lay the foundations for further studies and for a deeper understanding of the interplay between the chemical nature and the geometric arrangement of molecular units at the interface.

# Chapter 7 Understanding and screening hydrophobic interactions

## 7.1 Introduction

As described in section 2.4.3, hydrophobic surfaces and particles attract each other when immersed in water. This attraction is called hydrophobic interaction and its mechanism of action is not fully understood yet. However, it is possible to stabilize suspensions of hydrophobic nanoparticles: the most used stabilization technique is the addition of certain molecules, called *surfactants*.

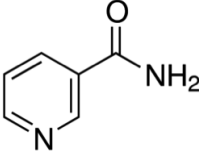
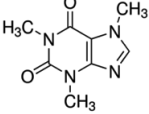
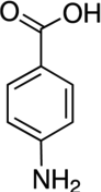
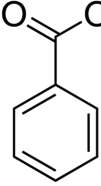
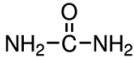
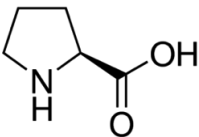
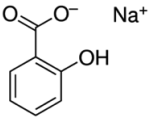
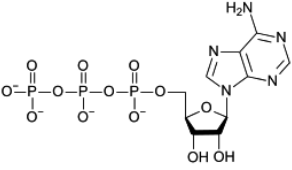
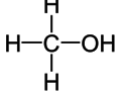
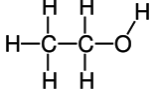
Surfactants are molecules that have a chemical structure composed of two different functional groups with different affinity with the same solvent molecule. In the case in which the solvent is water, in the standard terminology the *head* refers to the hydrophilic group and the *tail* to the hydrophobic one (often an alkyl chain with 8-22 carbons).<sup>117,118</sup> The properties and applications of surfactants are determined by the balance between the hydrophilic and hydrophobic portions of the molecules. They range from production processes such as the recovery and purification of raw materials in the petroleum and mining industries, to enhancing the quality of finished products such as paints, foods, pharmaceuticals and cosmetics.<sup>118</sup> When surfactants are dissolved in water above a critical concentration (CMC, *critical micelle concentration*) they spontaneously self-assemble into micelles (small aggregates in which the hydrophobic tails are hidden inside the aggregate and the heads are exposed to the water). Likewise, surfactants self-assemble around hydrophobic compounds, the tail pointing towards the compound and the head being exposed to the water. In this way the solubility of the complex (composed by the compound and the surfactants surrounding it) is crucially enhanced. Thanks to the same self-assembly mechanism at an air-water interface the surface tension of water decreases when surfactants are added to it.

Much less clear is the mechanism of action of smaller molecules to stabilize suspensions of hydrophobic particles. However, the possibility to use small molecules to solubilize hydrophobic compounds has been known for almost a century and this kind of molecules are broadly used in many industrial preparations, especially in the formulation of drugs.<sup>119</sup> A non-exhaustive summary of molecules known for this kind of behavior is listed in Table 2.

Even if most of these molecules are amphiphilic, they are too small to be considered surfactants and they do not form micelles. The mechanism by which these small molecules are able to decrease the hydrophobic attraction is not clear.<sup>119–123</sup> It may even be not the same for all molecules.<sup>124</sup>

Recently, the possibility that this mechanism acts also on the stabilization of biological fluids has been suggested. In fact, in most biological fluids a high concentration of macromolecules (mainly proteins) is present. Most of those molecules expose on the surface hydrophobic and hydrophilic patches. The hydrophobic surface exposed can be as high as 65% of the total solvent accessible surface area.<sup>125</sup> Nevertheless proteins remain functional at high concentrations, they do not misfold and unwanted aggregation is rarely observed. The recent finding that ATP can prevent the formation of protein aggregates

Table 2 Non-exhaustive list of small molecules known for their ability to stabilize suspension of hydrophobic particles.

Nicotinamide <sup>126,127</sup>	Caffeine <sup>126</sup>	Para-aminobenzoic acid (vitamin H <sub>1</sub> ) <sup>126</sup>	Sodium benzoate <sup>120-122,126</sup>	Urea <sup>120,124,126,127</sup>
				
L-proline <sup>128</sup>	Sodium salicylate <sup>120,122</sup>	Adenosine triphosphate (ATP) <sup>129</sup>	Methanol <sup>108,130</sup>	Ethanol <sup>130</sup>
				

and even dissolve previously formed ones<sup>129</sup> reveals a possible function of this molecule that was previously unknown. This finding may explain why the concentration of ATP in the cell is orders of magnitudes higher than the one needed for energetic purposes: ATP may help to avoid unwanted protein aggregation in the cytoplasmic environment.<sup>131</sup> In fact, the density of macromolecules is extremely high in the cytoplasm and proteins can occupy up to 35 % of the volume of the cell.<sup>132-135</sup> The fact that proline shows a similar stabilization effect on proteins<sup>128</sup> suggests that also single amino acids can play a similar role in the cytoplasmic environment. Based on the results on ATP and proline, it is reasonable to believe that the stability of proteins in highly concentrated fluids is guaranteed by the presence of small molecules, not only ATP and proline but also other free amino acids and metabolites.

However, the study of biological fluids is very challenging, mainly because of their variety and complexity. Even in the case in which suspensions of single proteins are separately considered, a lot of attention should be taken to guarantee that the native folding is maintained. Changes in pH or temperature, for example, can induce misfolding or unfolding, making the interpretation of experimental data very complex.

Gold nanoparticles (see Chapter 3) are a good model system to study this kind of phenomena.<sup>136</sup> They can be synthesized with a size comparable to the one of proteins and the properties of their surface can be designed in order to expose patches similar to the ones exposed on proteins. In this context, the synthesis method developed by Dr. Yang Ye and coworkers<sup>137</sup> is ideal for this study because it enables the preparation of large batches of monodisperse oleylamine coated gold nanoparticles, that can be divided into smaller batches. On each of this smaller batches a ligand exchange reaction can be performed in order to obtain different nanoparticles with the same core size but different surface properties.

The results presented in this chapter have been collected in the frame of a broad project with a series of long-term goals. First, we want to study the stabilization effect due to the addition of small molecules in suspension of gold nanoparticles. By studying the stabilization effect associated with a variety of additives we aim at building a library of stabilizing molecules, together with a library of destabilizing molecules and one of molecules that do not affect the stability. These libraries can be useful to understand the role of the molecular structure on the stabilizing effect.

Once the effect of the addition of single molecules on the suspensions of nanoparticles is known, the effect of addition of combinations of stabilizing and destabilizing molecules can be studied. In fact, in real biological fluids a variety of small molecules is present, in combination with large macromolecules.

At the same time, the fact that the interparticle interactions in a variety of systems are studied here, may allow for a deeper understanding of the nature (origin and length-scale) of hydrophobic interactions.

## 7.2 Effect of the addition of small molecules on hydrophobic interactions

Multiple batches of gold nanoparticles have been synthesized to address the previously listed open questions. The main techniques we have used to characterize the interparticle interactions are UV-vis spectroscopy, introduced in section 4.4, and SAXS, introduced in section 4.5.

In Figure 34 some representative spectra of gold nanoparticles collected in water are reported. They show the effect on interparticle interactions associated to a difference in the relative ratio of the ligands in the ligand shell and the effect of the concentration of the nanoparticles in suspension on the spectra. As clearly visible in the spectra, and discussed in section 4.5, repulsion between nanoparticles results in a peak in the low  $q$  region. This peak is due to a conserved interparticle distance in the spectrum. By increasing the concentration of the nanoparticles, this peak moves to higher  $q$  values, corresponding to a smaller interparticle distance. On the contrary, if attraction between nanoparticles exists, the spectra show a negative slope in the low- $q$  region.

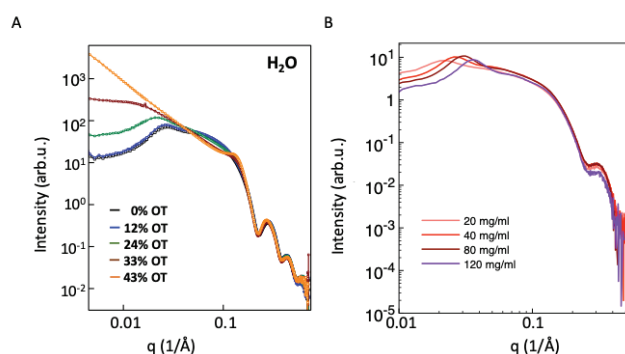
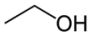
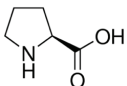
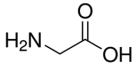
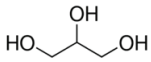
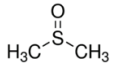
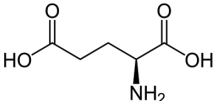
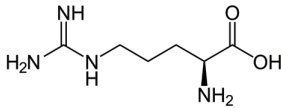
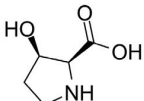
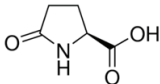


Figure 34 **Representative SAXS spectra of nanoparticles in water** (A) Effect of ligand composition. Different nanoparticles having the same gold core but a different ligand shell. The ligands in the shell are MUS and OT. The OT percent for each batch is shown in the legend. Particles with 12 % OT show repulsive interaction analogous to the all-MUS ones. Increasing the hydrophobic content (OT) results in less repulsion and more attraction. At the limit of 43% OT, fractal aggregation is observed (aggregates of multiple sizes are present in the sample, as indicated by the linearity of the spectrum in the low- $q$  region). (B) Effect of the concentration of nanoparticles. Spectra have been collected on the same batch of nanoparticles (28% OT, core diameter  $3.8 \pm 0.5$  nm) at different concentrations. Increasing the concentration, the peak at low  $q$  moves to higher  $q$  values, because the particles get closer in real space.

The list of ligands used in this study can be found in the following table. MUS has been chosen as hydrophilic ligand (negatively charged), OT and brOT as hydrophobic ones. Two hydrophobic ligands have been used to vary the morphology of the ligand shell. In fact, brOT is supposed to generate a random ligand shell when in combination with MUS, while ligand phase separation can happen when linear OT is used.<sup>44</sup>

Name	Acronym	Chemical structure
11-mercaptoundecane-1-sulfonate	MUS	<chem>CCCCCCCCCCCCS(=O)(=O)O</chem>
1-octanethiol	OT	<chem>CCCCCCCCS</chem>
3-methyl-7-methyl-octanethiol	brOT	<chem>CCCC(C)CC(C)CS</chem>

A summary of all the small molecules tested is reported in the following table. The color code is the following: green – stabilizing, yellow – no effect, red – destabilizing. The experimental data supporting this classification are listed in the next paragraphs. The solubility limit is reported in the table because it gives an idea of the range of concentrations that can be tested in the different cases. It should be stressed that different numbers are given in different references for the solubility limit of amino acids. Here, the value reported on PubChem (at 25°C) is shown, as an indication. We have observed that in certain cases we could easily dissolve quantities above this value (i.e. in the case of proline) or that precipitation was observed while working at the reported value (i.e. in the case of glycine).

Name (CAS number)	Chemical structure	Concentration tested	Solubility limit
Ethanol (64-17-5)		10 % - 20 %	miscible
L-proline (147-85-3)		162 mg/ml 230 mg/ml	162 mg/ml
Glycine (56-40-6)		125 mg/ml	249 mg/ml
Glycerol (56-81-5)		20 %	miscible
Dimethyl sulfoxide - DMSO (67-68-5)		10 % - 20 %	miscible
L-glutamic acid (56-86-0)		9 mg/ml	9 mg/ml
L-arginine (74-79-3)		182 mg/ml	182 mg/ml
Cis-L-3-hydroxyproline (567-35-1)		8 mg/ml	8 mg/ml
L-pyroglutamic acid (98-79-3)		258 mg/ml 4 mg/ml	258 mg/ml

### 7.2.1 Stabilizing molecules

Three different stabilizing molecules have been studied, all being capable to stabilize MUS:OT and MUS:brOT nanoparticles. A small stabilization effect has been observed also on all-MUS nanoparticles. In fact, even if in the case of all-MUS nanoparticles the interaction is mainly repulsive, some attractive forces are present, mainly because of the contribution of the hydrophobic alkyl-chains. These small attractive forces can be reduced by adding certain molecules.

The results presented here show that this screening of the interparticle attraction takes place regardless of the morphology of the ligand shell (because many ligand ratios and two different hydrophobic ligands have been tested).

Each molecule will be discussed individually in the following paragraphs.

#### Ethanol

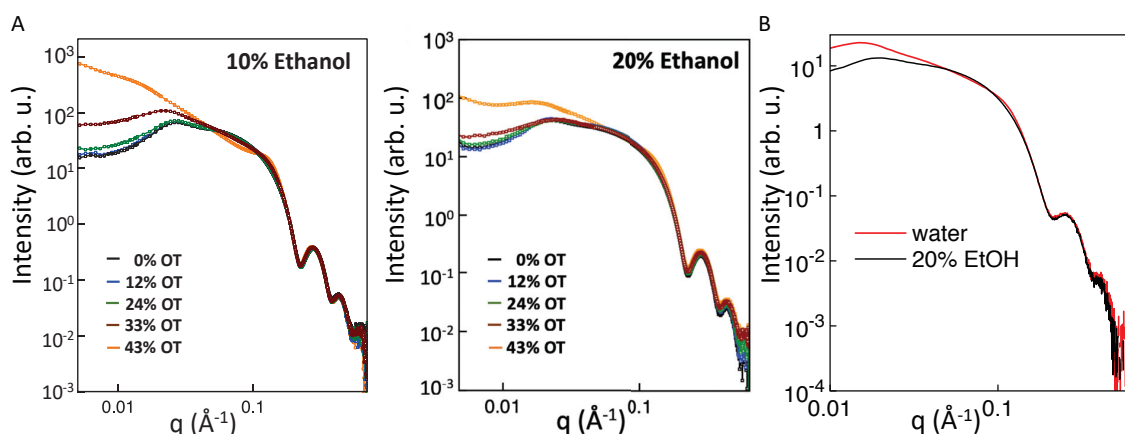


**Figure 35 Results on water-ethanol mixtures.** (A) Effect of the addition of ethanol (10% and 20%) on different MUS:OT nanoparticles. The OT concentration in the ligand shell is labelled in the legend. The plots should be compared to the ones collected in water (Figure 34). Addition of ethanol results in reduced attraction between nanoparticles. (B) Effect of ethanol addition on MUS:brOT nanoparticles (13% brOT, core diameter  $4.3 \pm 0.6$  nm). Also in this case, the addition of ethanol reduces the interparticle attraction.

The same series of batches of nanoparticles measured in water (Figure 34A), has been analyzed also in water ethanol mixtures (Figure 35A). The so obtained spectra show a clear decrease in the hydrophobic attraction between the nanoparticles, to the point that particles with a small amount of OT (below 25%) behave like pure-MUS nanoparticles when the amount of ethanol in the liquid mixture is 20%.

In Figure 35B the results obtained on a batch of MUS:brOT nanoparticles are presented. The stabilization effect is clearly visible also in this case, confirming the idea that the stabilization effect is not associated to a specific morphology of the ligand shell.

#### L-Proline

Addition of proline results in a decrease in the hydrophobic interactions. It is found that addition of 230 mg/ml of proline has a similar effect to the one due to addition of 10% ethanol (Figure 36A).

Confirming the findings on water-ethanol mixtures about the similar behavior of MUS:OT and MUS:brOT nanoparticles, also in the case of the addition of proline a decrease in the interparticle attraction is observed in both cases (Figure 36).

As visible in Figure 37, proline shows a small stabilization effect also on all-MUS nanoparticles. This phenomenon can be explained by the presence of the hydrophobic 11-carbon long alkyl chain in the MUS molecule.

### Glycine

Glycine is the smallest amino acid, however it shows some clear stabilization effect on gold nanoparticles, similar to the one of proline (Figure 37). While in the case of proline and ethanol amphiphilicity can be invoked as a possible explanation for the mechanism of action, this is not obvious in the case of glycine, since its lateral group is composed by a single hydrogen atom.

As in the case of proline and visible in Figure 37, glycine shows a small stabilization effect also on all-MUS nanoparticles. This phenomenon can be explained by the presence of the hydrophobic 11-carbon long alkyl chain in the MUS molecule.

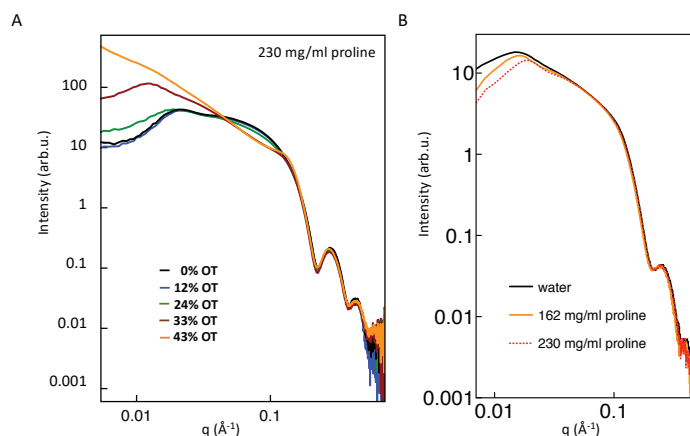


**Figure 36 Effect of addition of proline on interparticle interactions.** (A) Effect of addition of proline on different MUS:OT nanoparticles. The OT concentration in the ligand shell is labelled in the legend. The plots should be compared to the ones collected in water (Figure 34) and in water-ethanol mixtures (Figure 35). (B) Effect of proline addition on MUS:brOT nanoparticles (13% brOT, core diameter  $4.3 \pm 0.6$  nm). Also in this case the addition of proline reduces the interparticle attraction.

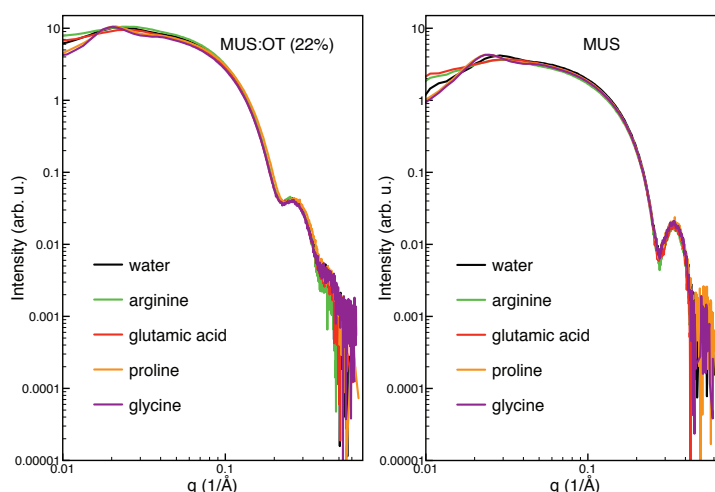


**Figure 37 Effect of addition of four different amino acids on interparticle interactions.** The case of MUS:OT nanoparticles and all-MUS nanoparticles are reported. In both cases proline and glycine have a stabilizing effect, while arginine and glutamic acid destabilize the suspension. The two batches of nanoparticles are not directly comparable in this case, because the size and polydispersity are different: the core diameter is  $4.0 \pm 0.6$  nm in the mixed ligand case and  $3.1 \pm 0.3$  nm in the mono-ligand case.



## 7.2.2 Molecules without any effect on the interactions

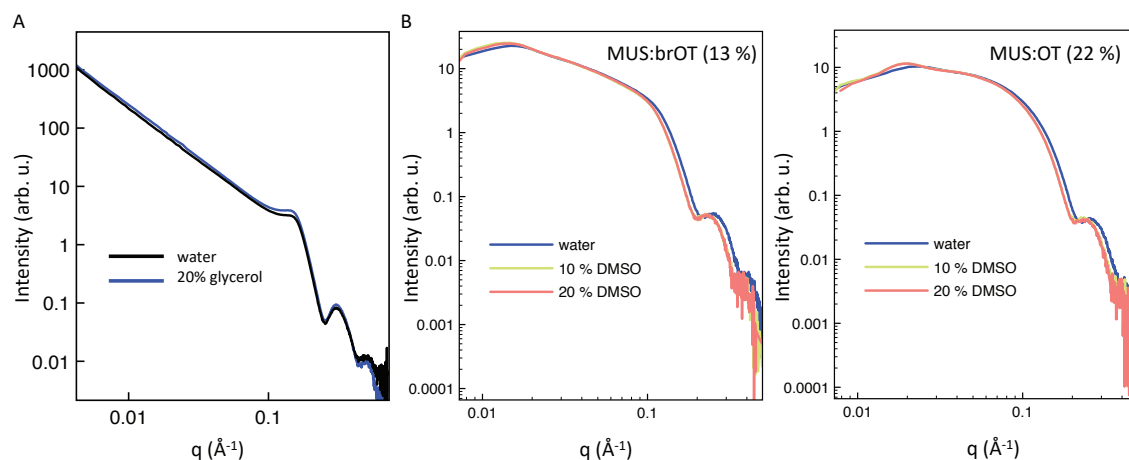


Figure 38 **Effect of the addition of two molecules with no effect on interparticle interactions.** (A) Addition of glycerol does not alter the interparticle interactions in the case of MUS:OT nanoparticles (OT  $\sim 40\%$ ). (B) Addition of DMSO does not significantly alter the interparticle interactions (tested both on MUS:OT and MUS:brOT nanoparticles). In both the cases the small shift in the water spectra is due to a wrong calibration of the sample-detector distance, which results in an error in the calculation of  $q$ . This experimental error does not affect the overall shape of the spectrum.

Two different molecules have been found that do not affect the interactions between the nanoparticles.

### Glycerol

As shown in Figure 38A glycerol does not affect the interparticle interactions on aggregating systems. This molecule is not amphiphilic and neutral: this may explain why it does not have any particular effect on the observed interactions

### Dimethyl sulfoxide

As shown in Figure 38B, addition of DMSO does not affect interparticle interactions on two different batches of nanoparticles. On the contrary of glycerol, DMSO is slightly amphiphilic. However, amphiphilicity is not functional, in this case, for the stabilization phenomena.

### 7.2.3 Destabilizing molecules

Different destabilizing molecules have been studied. In most of the cases the destabilization effect can be associated to the screening of the charge of the particles, due to the charge of the additives.

#### L-arginine

As visible in Figure 37, the addition of arginine destabilizes the suspension of negatively charged nanoparticles. This phenomenon can be explained by the fact that arginine is positively charged when dissolved in water. We believe that the addition of arginine alters the double layer, screening the negative charge of the particles. In fact, the destabilization is clearly visible in the case of all-MUS nanoparticles, but it is negligible in the case of MUS:OT (22 %) nanoparticles, consistently with the fact that the overall negative charge of the latter is smaller.

#### L-glutamic acid

The destabilization due to the addition of glutamic acid to suspension of nanoparticles is clearly visible in Figure 37 (more evident for all-MUS nanoparticles) and brings to precipitation of both the suspensions of nanoparticles in 2-5 days, if stored in a vial.

Glutamic acid, when dissolved in water, dissociates into glutamate anion  $\text{Glu}^-$  and  $\text{H}^+$ . The free  $\text{H}^+$  can protonate the sulfonate groups of MUS ligands, effectively screening electrostatic repulsion between the nanoparticles. This phenomenon explains the destabilizing effect observed in SAXS.

We have decided to compare this precipitation phenomenon with the precipitation induced by simple acids (which can be observed already one day after the addition of the acid).

Figure 39 shows the shift over time in the plasmon resonance of the suspension of nanoparticles, as measured by UV-vis spectroscopy (see section 4.4), after the addition of acids. It is clear that the kinetics of the precipitation in the case of glutamic acid significantly differs from the one of ionic acids (at the same pH). This result suggests that the presence of the glutamate anion influences the kinetics of the precipitation. One possible explanation is that glutamate anion is screening the attraction between the nanoparticles. Similar data have been obtained also in the case of brOT nanoparticles (not shown). On the contrary, we did not observe precipitation if NaCl (at the same molarity as HCl) was added to the suspension, confirming the idea that in the case of acids precipitation is due to protonation of MUS ligands.

#### Cis-L-3-hydroxyproline and L-pyroglutamic acid

Even if both these molecules resemble L-proline, they both induce precipitation of suspension of MUS:OT nanoparticles. No spectra have been collected because the precipitation was clearly visible by eye inspection of the sample.

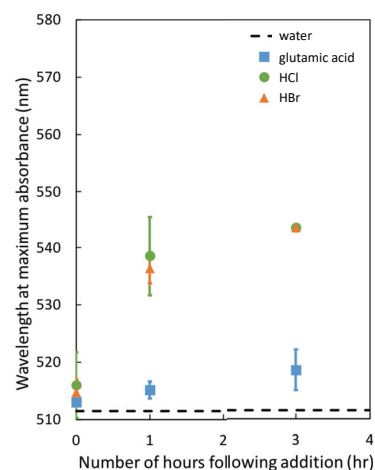


**Figure 39 Time evolution of the surface plasmon resonance for suspensions of nanoparticles upon addition of acids.** The wavelength associated to the maximum absorbance is plotted as a function of time.

## 7.2.4 Mixtures of molecules

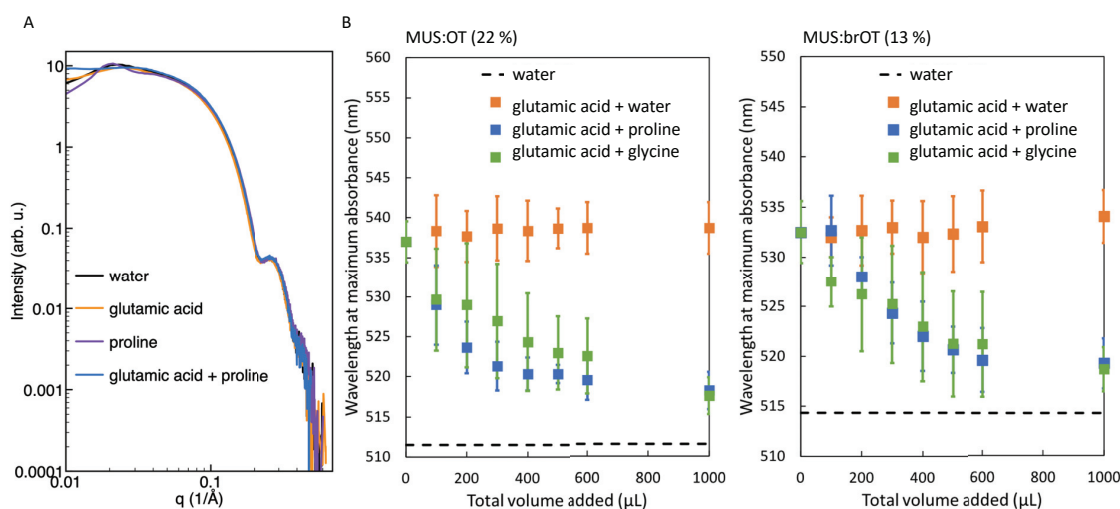


Figure 40 **Effect of mixtures of molecules on the stability of suspensions of nanoparticles.** (A) SAXS spectra obtained after addition of proline, glutamic acid and a combination of both. The flattening of the spectrum in the low- $q$  region may indicate that the particles are in a non-interaction regime (ideal gas state). (B) Restabilization effect due to addition of proline and glycine to aggregated nanoparticles (aggregation induced by glutamic acid). For technical requirements of the machines, the concentrations of nanoparticles used in A and B are different: 20 mg/ml in the SAXS case and 0.2 mg/ml in the UV-vis case.

The effect of addition of combinations of amino acids has been tested. As visible in Figure 40A, the SAXS spectrum collected on MUS:OT nanoparticles, with simultaneous addition of glutamic acid and proline is qualitatively similar to the spectrum of non-interacting particles (flat curve in the low- $q$  region). This observation suggests that proline may stabilize the nanoparticles even in presence of glutamic acid. In fact, no precipitation was observed in vials containing nanoparticles and a mixture of both amino acids.

To confirm this possibility, the ability of stabilizing amino acids to redisperse previously aggregated nanoparticles have been tested by UV-vis spectroscopy. Precipitation was induced in suspensions of nanoparticles by the addition of glutamic acid. After the precipitation, two-minute sonication was performed to redisperse the nanoparticles and UV-vis spectra were collected (Figure 40B). Solutions of stabilizing amino acids have been added to the UV-vis cuvette and new spectra have been collected one minute after addition. As visible in Figure 40B the addition of stabilizing amino acids resulted in redispersion of the aggregates. A control measurement was performed by adding ultrapure water to the UV-vis cuvette, to make sure the redispersion was not due to dilution effects. As clearly visible in Figure 40B dilution is not sufficient to redisperse the aggregates.

### 7.3 Examples of applications to food science

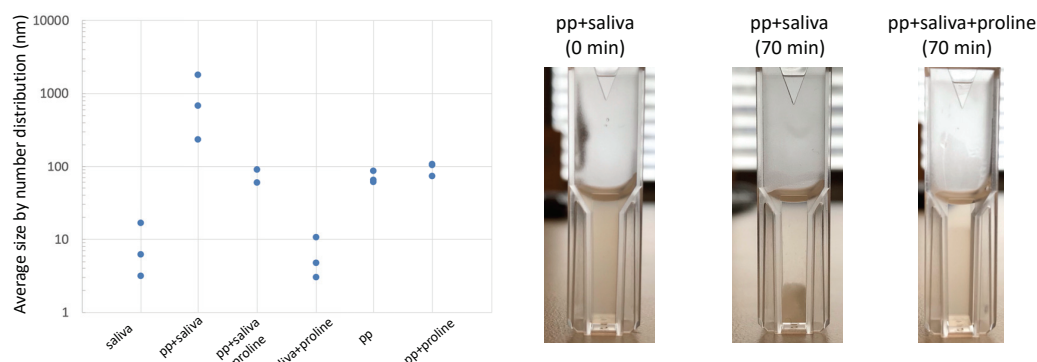


Figure 41 **Stabilization effect of proline on mixtures of saliva and pea protein.** DLS results on mixtures of saliva, pea protein (pp) and proline. Aggregation is visible in the pp+saliva mixture. On the contrary, pp+saliva+proline shows similar size as the pp and pp+proline samples. The size distribution for saliva is not affected by the addition of proline. As clearly visible in the pictures, 70 minutes after preparation of the samples, precipitation is evident in the pp+saliva sample, while only a small gradient in the color is visible in the case of pp+saliva+proline, indicating higher stability of this suspension.

Astringency is a feeling of dryness and roughness, perceived in the mouth and caused by certain foods, such as black tee, quince and unripe persimmon. It is due to aggregation of glycoproteins, naturally present in saliva, due to their interaction with molecules contained in the astringent food. This phenomenon is well-known and problematic (for the unpleasant feeling) in the case of soy milk.<sup>138,139</sup>

Since we found that proline decreases the hydrophobic interactions between nanoparticles, we have decided to test it on mixtures of pea-protein (pp) and saliva to check whether it can decrease aggregation and therefore the astringent feeling.

First, we performed DLS measurements on mixtures of pea protein (5 mg/ml), saliva and proline (80 mg/ml). The results are shown in Figure 41. The goal of these experiments was to obtain a qualitative measurement of protein aggregation in the mixtures. In the calculations of the size distribution, the solvent has been considered pure water in all the cases, neglecting differences in density. We believe this is a valid approximation because our control measurements do not show significant differences in the size distributions (the size distributions for saliva and saliva+proline are not significantly different and the same is valid also for the size distributions of pp and pp+proline). The bigger size of particles measured in the case of pp+saliva is an indication of protein aggregation. The fact that the pp+saliva+proline sample shows a similar distribution to the pp sample indicates that proline is effectively stabilizing the mixture. The same effect is confirmed by the pictures of the samples taken immediately after preparation and 70 minutes later: precipitation is clearly visible in the case of pp+saliva, while only a small gradient in the color is visible in the case of pp+saliva+proline.

We then moved to sensory experiments. We collected a variety of non-diary milk products and we added different amounts of proline. The taste of proline is salty and sour,<sup>140</sup> therefore care should be taken in choosing the right amount to add to the non-diary milks in order to avoid an unpleasant taste. We found that 5 mg/ml proline is the highest concentration that does not result in an unpleasant feeling, when added to soy-milk. In a sensory panel composed of 10 volunteers, who blindly tested soy-milk with and without proline, 8 considered the milk with proline less astringent than the original one.

We believe these results are promising and show one possible industrial application of the screening of hydrophobic interactions by small molecules.

## 7.4 Conclusions and outlook

The results presented in section 7.2 show that it is possible to change the interparticle interactions by adding small molecules to the suspension. In particular, we have shown that the stability of the suspensions can be increased by addition of certain stabilizing molecules (such as ethanol, L-proline and glycine).

The molecular structure required for the stabilization effect is not known yet. In fact, the amphiphilic nature of the molecule has shown not to be a good indicator to predict a stabilizing behavior (i.e. glycine stabilizes, without being amphiphilic, while DMSO does not stabilize, even if it is amphiphilic).

In the future, the addition of small molecules should be tested on hydrophilic charge-neutral nanoparticles (to exclude the electrostatic repulsion) and on nanoparticles that do not contain any hydrophobic group in the ligand shell, as a control.

We have started a collaboration with the group of Stefano Vanni (university of Fribourg) to test the possibility to fit the SAXS spectra collected and extract the interaction potential between the nanoparticles. The advantage of having collected spectra for a variety of systems may allow us to estimate the decay length of hydrophobic interactions. Furthermore, if an exponential decay for hydrophobic forces is assumed,<sup>12</sup>

$$F(r) = F_0 e^{-\frac{r}{\lambda}},$$

we may be able to determine whether the screening is affecting the decay length of the interaction ( $\lambda$ ) or, instead, the interaction coefficient ( $F_0$ ).

## 7.5 Materials and methods

### SAXS

SAXS measurements were performed using Rigaku BioSAXS 2000. Soda lime glass capillaries with inner diameter 1.0 mm and wall thickness of 0.1 mm were used for the measurements (Hampton research). The acquisition time was of minimum half an hour for each sample. The spectra of the solvent were collected in the same conditions and subtracted from the spectrum collected for the suspensions of nanoparticles to get the spectrum of the nanoparticles alone.

### DLS

All the DLS data have been collected on a Nano ZetaSizer machine from Malvern. Disposable cuvettes have been used.

### UV-vis

UV-Vis spectroscopy was performed on nanoparticles (0.2 mg/mL in concentration) on a PerkinElmer Lambda 25 UV/Vis spectrometer. Measurements were performed on a wavelength window of 400–700 nm using a scan speed of 240 nm/min. Disposable cuvettes were used for all measurements. Wavelength of maximum absorbance was determined by directly finding the local maximum of the resonance peak.

### Saliva collection protocol

In the morning, whole mouth saliva was collected by 1 or 2 healthy subjects, whom did not eat, brush their teeth or drink anything but water for one hour preceding the session. 5 mL of saliva from each subject was collected on ice in a 50 mL falcon tube containing 2 mL milliQ water, by spitting resting saliva for maximum 30 minutes, following the steps described below:

- Before collection, rinse the mouth 3 times using water from the glass. To complete 1 rinse, use a sip of water to wash every part of your mouth and then swallow the water. Repeat 3 times.
- After rinsing the mouth, spit twice into the sink.
- To collect saliva, close the lips, and allow saliva to be produced for 2-5 minutes.
- Using small movements, position the saliva in the front part of the mouth.
- Expectorate the saliva into the container until you reach the volume indicated by the mark.

The collected saliva was pooled and centrifuged in 50 mL Eppendorf's at 11500 rpm for 30 minutes at 4°C. The supernatant was pooled and kept on ice. DLS measurements were performed within one hour.

### Chemicals

All chemicals were purchased except for MUS and brOT, which were synthesized following protocols previously reported by our group.<sup>44,141</sup>

1-octanethiol, ethanol, L-proline, HCl, HBr, glycine, DMSO were purchased from Sigma Aldrich, Glycerol from Fluka. L-glutamic acid from Apollo Scientific, L-arginine from ABCR chemicals, Cis-L-3-hydroxyproline from Santa Cruz Biotechnology and L-Pyroglutamic acid was purchased from Flurorochem.

The pea protein extract Peazazz from Burcon was used in the DLS experiments together with human derived saliva.

## Chapter 8 Conclusions and outlook

Complex surfaces exposing a variety of surface groups are extremely common in biological systems: as an example we have considered proteins, which have a solvent accessible surface composed of hydrophilic and hydrophobic domains. The hydration of proteins is crucial for their folding and functionality, however the hydration of proteins is not fully understood yet. In this thesis I have presented new results on the interactions of water with this kind of complex surfaces.

Gold nanoparticles have been used as a model system throughout this thesis. Their solvent accessible surface can be engineered to mimic the surface of proteins, producing particles that expose hydrophilic and hydrophobic domains of different sizes and shapes on their surface.

We have measured the time-averaged structure of the interfacial water and the solid-liquid work of adhesion on two batches of identical nanoparticles that differ only in the arrangement of molecules in the ligand shell (Chapter 6). They show significant differences, thus confirming the hypothesis that the arrangement of the ligands plays a significant role in the determination of the time-averaged structure of the interfacial water and therefore on the interfacial properties. A predictive model for the interfacial properties has been developed, which shows that the arrangement of the nearest neighbors at the molecular level is sufficient to estimate the interfacial properties of the overall surface.

Protein stability is not guaranteed simply by the water structure in the first hydration layers: long-range interactions are important to guarantee that proteins in suspension do not aggregate. To address this problem, the stability of suspensions of amphiphilic nanoparticles has been studied (Chapter 7) and the possibility to decrease the hydrophobic attraction by adding small molecules has been investigated. We found that certain small molecules, such as ethanol, L-proline and glycine can help the dispersion of gold nanoparticles.

We believe that these results represent an important step forward in the study of the interaction of water with complex surfaces. In fact, from our results we can infer that to estimate the overall hydrophobicity of a protein one needs to know the arrangement of the exposed amino acids: the common approach that calculates the overall hydrophobicity simply as the average of the hydrophobicities of the individual amino acids is thus not accurate. On the other side we found that protein stability in highly concentrated biological fluids is likely to be mediated by the presence of small molecules, such as free amino acids.

The results presented in chapter 7, however, are still preliminary: additional experimental work is required to fully understand the mechanism of action of this stabilization phenomena. A non-exhaustive list of promising further developments is presented below:

- The data collected on interparticle interactions can be very useful to improve our basic understanding of hydrophobic interactions: extracting an experimental potential from the recorded SAXS spectra may allow for an experimental determination of the decay length and intensity of hydrophobic attraction. The fitting of spectra collected at different temperatures can allow for an experimental determination of the temperature dependence of hydrophobic interactions, allowing

for the discrimination of entropy driven phenomena. For the completeness of the study additional systems of nanoparticles may be used, with a ligand shell composed of a variety of ligands: hydrophobicity can be reduced by choosing ligands with shorter alkyl chains, and electrostatic repulsion can be avoided by selecting uncharged ligands.

- To unravel the mechanism of action of the stabilization it would be useful to understand whether the stabilization is due to a difference in the water structure in the bulk or rather to an accumulation of small molecules at the water-nanoparticle interface. Small angle neutron scattering measurements should allow for the detection of differences in the concentrations of small molecules in the bulk and at the interface. By performing neutron scattering experiments on suspensions of nanoparticles with the addition of different concentrations of small molecules one should be able to recognize an eventual correlation between the accumulation at the interface and the stabilization effect. These studies on the concentration dependence of the stabilization effect should help to understand the mechanism behind it.
- To understand the biological relevance of the results obtained, additional measurements can be performed. The first improvement would be to perform the experiments under buffered conditions: in this way electrostatic effects due to charged amino acids can be avoided and all the amino acids can be tested in their zwitterionic form. This measurement would allow for a better understanding of the effect of molecular structures on stabilization phenomena. The effect of combination of different amino acids and metabolites should be tested to mimic, for example, the intracellular environment. Once these combinations have been tested on model systems such as nanoparticles, one can move to the analysis of the behavior of known proteins in suspension. The scattering contrast of proteins being low, this kind of experiment can be performed only at a synchrotron facility.



# References

1. Luo, Z. *et al.* Determination and evaluation of the nonadditivity in wetting of molecularly heterogeneous surfaces. *PNAS* (2019) doi:10.1073/pnas.1916180116.
2. Ball, P. Water as an Active Constituent in Cell Biology. *Chem. Rev.* **108**, 74–108 (2008).
3. Ball, P. Water — an enduring mystery. *Nature* **452**, 291–292 (2008).
4. Ohmine, Iwao. & Tanaka, Hideki. Fluctuation, relaxations, and hydration in liquid water. Hydrogen-bond rearrangement dynamics. *Chem. Rev.* **93**, 2545–2566 (1993).
5. Chaplin, M. Water structure and science. <http://www1.lsbu.ac.uk/water/index.html>.
6. Ball, P. Water in biology. <http://waterinbiology.blogspot.com/>.
7. International Association for the Properties of Water and Steam. <http://www.iapws.org/index.html>.
8. Jha, A. *The Water Book*. (Headline, 2016).
9. Ball, P. *H2O: A Biography of Water*. (Hachette UK, 2015).
10. Fishman, C. *The Big Thirst: The Secret Life and Turbulent Future of Water*. (Free Press, 2011).
11. Soper, A. K. The radial distribution functions of water and ice from 220 to 673 K and at pressures up to 400 MPa. *Chemical Physics* **258**, 121–137 (2000).
12. Israelachvili, J. N. *Intermolecular and surface forces*. (Elsevier, Acad. Press, 2011).
13. Keutsch, F. N. & Saykally, R. J. Water clusters: Untangling the mysteries of the liquid, one molecule at a time. *Proceedings of the National Academy of Sciences* **98**, 10533–10540 (2001).
14. Southall, N. T., Dill, K. A. & Haymet, A. D. J. A View of the Hydrophobic Effect. *J. Phys. Chem. B* **106**, 521–533 (2002).
15. Lum, K., Chandler, D. & Weeks, J. D. Hydrophobicity at Small and Large Length Scales. *J. Phys. Chem. B* **103**, 4570–4577 (1999).
16. Chandler, D. Interfaces and the driving force of hydrophobic assembly. *Nature* **437**, 640–647 (2005).

17. Godawat, R., Jamadagni, S. N. & Garde, S. Characterizing hydrophobicity of interfaces by using cavity formation, solute binding, and water correlations. *Proceedings of the National Academy of Sciences* **106**, 15119–15124 (2009).
18. Roke, S. New light on hidden surfaces.
19. Cardon, M. The Devil and the Surfaces. *The Shot Peener* (2006).
20. Höfer, U. Self-Trapping of Electrons at Surfaces. *Science* **279**, 190–191 (1998).
21. Pontikis, V. Surface Reconstruction. in *Encyclopedia of Materials: Science and Technology* (eds. Buschow, K. H. J. et al.) 9052–9057 (Elsevier, 2001). doi:10.1016/B0-08-043152-6/01633-8.
22. Shen, J. *et al.* Liquid Phase Exfoliation of Two-Dimensional Materials by Directly Probing and Matching Surface Tension Components. *Nano Lett.* **15**, 5449–5454 (2015).
23. Fukuma, T. Water distribution at solid/liquid interfaces visualized by frequency modulation atomic force microscopy. *Sci Technol Adv Mater* **11**, (2010).
24. Wetting. <http://web.mit.edu/nnf/education/wettability/wetting.html>.
25. Silvera Batista, C. A., Larson, R. G. & Kotov, N. A. Nonadditivity of nanoparticle interactions. *Science* **350**, 1242477–1242477 (2015).
26. Derjaguin, B. V., Churaev, N. V. & Muller, V. M. *Surface Forces*. (Springer US, 1987). doi:10.1007/978-1-4757-6639-4.
27. Meyer, E. E., Rosenberg, K. J. & Israelachvili, J. Recent progress in understanding hydrophobic interactions. *Proceedings of the National Academy of Sciences* **103**, 15739–15746 (2006).
28. Janeček, J. & Netz, R. R. Interfacial Water at Hydrophobic and Hydrophilic Surfaces: Depletion versus Adsorption. *Langmuir* **23**, 8417–8429 (2007).
29. Despa, F. & Berry, R. S. The Origin of Long-Range Attraction between Hydrophobes in Water | Elsevier Enhanced Reader. *Biophysical Journal* **92**, 373–378 (2007).
30. Despa, F., Fernandez, A. & Berry, R. S. Dielectric Modulation of Biological Water. *PHYSICAL REVIEW LETTERS* **4** (2004).

31. Rajamani, S., Truskett, T. M. & Garde, S. Hydrophobic hydration from small to large lengthscales: Understanding and manipulating the crossover. *Proceedings of the National Academy of Sciences of the United States of America* **102**, 9475–9480 (2005).
32. Commission Recommendation of 18 October 2011 on the definition of nanomaterial Text with EEA relevance. <http://data.europa.eu/eli/reco/2011/696/oj/eng> (2011).
33. Zheng, N., Fan, J. & Stucky, G. D. One-Step One-Phase Synthesis of Monodisperse Noble-Metallic Nanoparticles and Their Colloidal Crystals. *Journal of the American Chemical Society* **128**, 6550–6551 (2006).
34. Yang, Y., Serrano, L. A. & Guldin, S. A Versatile AuNP Synthetic Platform for Decoupled Control of Size and Surface Composition. *Langmuir* **34**, 6820–6826 (2018).
35. Luo, Z. *et al.* Quantitative 3D determination of self-assembled structures on nanoparticles using small angle neutron scattering. *Nature Communications* **9**, 1343 (2018).
36. Luo, Z. *et al.* Mass spectrometry and Monte Carlo method mapping of nanoparticle ligand shell morphology. *Nature Communications* **9**, 1–9 (2018).
37. Uzun, O. *et al.* Water-soluble amphiphilic gold nanoparticles with structured ligand shells. *Chem. Commun.* 196–198 (2008) doi:10.1039/B713143G.
38. Singh, C. *et al.* Entropy-Mediated Patterning of Surfactant-Coated Nanoparticles and Surfaces. *Phys. Rev. Lett.* **99**, 226106 (2007).
39. Singh, C. Computational studies of surfactant self-assembly on nanostructured surfaces.
40. Centrone, A. *et al.* The role of nanostructure in the wetting behavior of mixed-monolayer-protected metal nanoparticles. *PNAS* **105**, 9886–9891 (2008).
41. Kuna, J. J. *et al.* The effect of nanometre-scale structure on interfacial energy. *Nat Mater* **8**, 837–842 (2009).
42. Cagno, V. *et al.* Broad-spectrum non-toxic antiviral nanoparticles with a virucidal inhibition mechanism. *Nature Materials* **17**, 195–203 (2018).

43. Huang, R., Carney, R. P., Stellacci, F. & Lau, B. L. T. Colloidal Stability of Self-Assembled Monolayer-Coated Gold Nanoparticles: The Effects of Surface Compositional and Structural Heterogeneity. *Langmuir* **29**, 11560–11566 (2013).
44. Verma, A. *et al.* Surface Structure-Regulated Cell Membrane Penetration by Monolayer Protected Nanoparticles. *Nat Mater* **7**, 588–595 (2008).
45. Ertem, E., Diez-Castellnou, M., Ong, Q. K. & Stellacci, F. Novel Sensing Strategies Based on Monolayer Protected Gold Nanoparticles for the Detection of Metal Ions and Small Molecules. *Chem Rec* **18**, 819–828 (2018).
46. Ong, Q., Luo, Z. & Stellacci, F. Characterization of Ligand Shell for Mixed-Ligand Coated Gold Nanoparticles. *Acc. Chem. Res.* **50**, 1911–1919 (2017).
47. Marbella, L. E. & Millstone, J. E. NMR Techniques for Noble Metal Nanoparticles. *Chem. Mater.* **27**, 2721–2739 (2015).
48. Dongargaonkar, A. A. & Clogston, J. D. Quantitation of Surface Coating on Nanoparticles Using Thermogravimetric Analysis. in *Characterization of Nanoparticles Intended for Drug Delivery* (ed. McNeil, S. E.) 57–63 (Springer, 2018). doi:10.1007/978-1-4939-7352-1\_6.
49. Rulison, C. So you want to measure surface energy. *A tutorial designed to provide basic understanding of the concept solid surface energy, and its many complications*, TN306/CR 1–16 (1999).
50. Zisman, W. A. Relation of the Equilibrium Contact Angle to Liquid and Solid Constitution. in *Contact Angle, Wettability, and Adhesion* (ed. Fowkes, F. M.) vol. 43 1–51 (AMERICAN CHEMICAL SOCIETY, 1964).
51. Owens, D. K. & Wendt, R. C. Estimation of the surface free energy of polymers. *Journal of Applied Polymer Science* **13**, 1741–1747 (1969).
52. Surface Tension Components and Molecular Weight of Selected Liquids. [https://www.accudynetest.com/surface\\_tension\\_table.html?rd=self&](https://www.accudynetest.com/surface_tension_table.html?rd=self&).
53. Binnig, G., Quate, C. F. & Gerber, Ch. Atomic Force Microscope. *Phys. Rev. Lett.* **56**, 930–933 (1986).
54. Burnham, N. A., Colton, R. J. & Pollock, H. M. Interpretation of force curves in force microscopy. *Nanotechnology* **4**, 64–80 (1993).

- 
55. Garcia, R. & Perez, R. Dynamic atomic force microscopy methods. *Surface science reports* **47**, 197–301 (2002).
56. Chen, X. *et al.* Optimizing phase imaging via dynamic force curves. *Surface Science* **460**, 292–300 (2000).
57. Lantz, M., Liu, Y. Z., Cui, X. D., Tokumoto, H. & Lindsay, S. M. Dynamic force microscopy in fluid. *Surf. Interface Anal.* **27**, 354–360 (1999).
58. Radmacher, M. Measuring the elastic properties of biological samples with the AFM. *IEEE Engineering in Medicine and Biology Magazine* **16**, 47–57 (1997).
59. Zhang, X. *et al.* Probing double layer structures of Au (111)–BMIPF<sub>6</sub> ionic liquid interfaces from potential-dependent AFM force curves. *Chem. Commun.* **48**, 582–584 (2012).
60. Fukuma, T. & Garcia, R. Atomic- and Molecular-Resolution Mapping of Solid–Liquid Interfaces by 3D Atomic Force Microscopy. *ACS Nano* **12**, 11785–11797 (2018).
61. Zlatanova, J., Lindsay, S. M. & Leuba, S. H. Single molecule force spectroscopy in biology using the atomic force microscope. *Progress in biophysics and molecular biology* **74**, 37–61 (2000).
62. Samorì, B., Zuccheri, G. & Baschieri, P. Protein Unfolding and Refolding Under Force: Methodologies for Nanomechanics. *ChemPhysChem* **6**, 29–34 (2005).
63. Helenius, J., Heisenberg, C.-P., Gaub, H. E. & Muller, D. J. Single-cell force spectroscopy. *Journal of Cell Science* **121**, 1785–1791 (2008).
64. Voïtchovsky, K. Anharmonicity, solvation forces, and resolution in atomic force microscopy at the solid–liquid interface. *Phys. Rev. E* **88**, 022407 (2013).
65. Voïtchovsky, K., Kuna, J. J., Contera, S. A., Tosatti, E. & Stellacci, F. Direct mapping of the solid–liquid adhesion energy with subnanometre resolution. *Nature Nanotechnology* **5**, 401–405 (2010).
66. Miller, E. J. *et al.* Sub-nanometer Resolution Imaging with Amplitude-modulation Atomic Force Microscopy in Liquid. *JoVE (Journal of Visualized Experiments)* e54924–e54924 (2016) doi:10.3791/54924.
67. Van Cleef, M., Holt, S. A., Watson, G. S. & Myhra, S. Polystyrene spheres on mica substrates: AFM calibration, tip parameters and scan artefacts. *Journal of Microscopy* **181**, 2–9 (1996).

- 
68. Bonanni, B. & Cannistraro, S. Gold nanoparticles on modified glass surface as height calibration standard for atomic force microscopy operating in contact and tapping mode. *J. Nanotechnol. Online* (2005).
69. FraxedasCalduch,Jordi, Perez-Murano,Francesc, Staufer,Urs & RullTrinidad, Enrique. METHOD FOR MONITORING RADIUS AND SHAPE VARIATIONS OF ATOMIC FORCE MICROSCOPE CANTILEVER TIPS AND DEVICE THEREOF.
70. Maragliano, C., Glia, A., Stefancich, M. & Chiesa, M. Effective AFM cantilever tip size: methods for *in-situ* determination. *Measurement Science and Technology* **26**, 015002 (2015).
71. Lambert, A. G., Davies, P. B. & Neivandt, D. J. Implementing the Theory of Sum Frequency Generation Vibrational Spectroscopy: A Tutorial Review. *Applied Spectroscopy Reviews* **40**, 103–145 (2005).
72. Roke, S. & Gonella, G. Nonlinear Light Scattering and Spectroscopy of Particles and Droplets in Liquids. *Annual Review of Physical Chemistry* **63**, 353–378 (2012).
73. Kawai, T., Neivandt, D. J. & Davies, P. B. Sum Frequency Generation on Surfactant-Coated Gold Nanoparticles. *J. Am. Chem. Soc.* **122**, 12031–12032 (2000).
74. Tourillon, G. *et al.* Total internal reflection sum-frequency generation spectroscopy and dense gold nanoparticles monolayer: a route for probing adsorbed molecules. *Nanotechnology* **18**, 415301 (2007).
75. Weeraman, C., Yatawara, A. K., Bordenyuk, A. N. & Benderskii, A. V. Effect of Nanoscale Geometry on Molecular Conformation: Vibrational Sum-Frequency Generation of Alkanethiols on Gold Nanoparticles. *J. Am. Chem. Soc.* **128**, 14244–14245 (2006).
76. Perakis, F. *et al.* Vibrational Spectroscopy and Dynamics of Water. *Chem. Rev.* (2016) doi:10.1021/acs.chemrev.5b00640.
77. Du, Q., Superfine, R., Freysz, E. & Shen, Y. R. Vibrational spectroscopy of water at the vapor/water interface. *Physical Review Letters* **70**, 2313 (1993).
78. Du, Quan, Freysz, Eric & Shen, Y. Ron. Surface Vibrational Spectroscopic Studies of Hydrogen Bonding and Hydrophobicity. *Science* **264**, 826–828 (1994).
79. Tyrode, E. & Liljeblad, J. F. D. Water Structure Next to Ordered and Disordered Hydrophobic Silane Monolayers: A Vibrational Sum Frequency Spectroscopy Study. *J. Phys. Chem. C* **117**, 1780–1790 (2013).

- 
80. Smolentsev, N., Smit, W. J., Bakker, H. J. & Roke, S. The interfacial structure of water droplets in a hydrophobic liquid. *Nature Communications* **8**, 15548 (2017).
81. Bonn, M., Nagata, Y. & Backus, E. H. G. Molecular Structure and Dynamics of Water at the Water–Air Interface Studied with Surface-Specific Vibrational Spectroscopy. *Angewandte Chemie International Edition* **54**, 5560–5576 (2015).
82. Amendola, V. & Meneghetti, M. Size Evaluation of Gold Nanoparticles by UV–vis Spectroscopy. *J. Phys. Chem. C* **113**, 4277–4285 (2009).
83. Svergun, D. I. & Koch, M. H. J. Small-angle scattering studies of biological macromolecules in solution. *Rep. Prog. Phys.* **66**, 1735–1782 (2003).
84. Li, T., Senesi, A. J. & Lee, B. Small Angle X-ray Scattering for Nanoparticle Research. *Chem. Rev.* **116**, 11128–11180 (2016).
85. Rieker, T., Hanprasopwattana, A., Datye, A. & Hubbard, P. Particle Size Distribution Inferred from Small-Angle X-ray Scattering and Transmission Electron Microscopy. *Langmuir* **15**, 638–641 (1999).
86. Breßler, I., Kohlbrecher, J. & Thünemann, A. F. SASfit: a tool for small-angle scattering data analysis using a library of analytical expressions. *J Appl Cryst* **48**, 1587–1598 (2015).
87. Kohlbrecher, J. & Studer, A. Transformation cycle between the spherically symmetric correlation function, projected correlation function and differential cross section as implemented in SASfit. *J Appl Cryst* **50**, 1395–1403 (2017).
88. Tomaszewska, E. *et al.* Detection Limits of DLS and UV-Vis Spectroscopy in Characterization of Polydisperse Nanoparticles Colloids. *Journal of Nanomaterials* vol. 2013 e313081 <https://www.hindawi.com/journals/jnm/2013/313081/> (2013).
89. Panáček, A. *et al.* Silver Colloid Nanoparticles: Synthesis, Characterization, and Their Antibacterial Activity. *J. Phys. Chem. B* **110**, 16248–16253 (2006).
90. Pietak, A., Korte, S., Tan, E., Downard, A. & Staiger, M. P. Atomic force microscopy characterization of the surface wettability of natural fibres. *Applied Surface Science* **253**, 3627–3635 (2007).

- 
91. Park, W., Müller, S., Baumann, R.-P., Becker, S. & Hwang, B. Surface energy characterization of nanoscale metal using quantitative nanomechanical characterization of atomic force microscopy. *Applied Surface Science* **507**, 145041 (2020).
  92. Park, W. *et al.* Corrigendum to “Surface energy characterization of nanoscale metal using quantitative nanomechanical characterization of atomic force microscopy” [Appl. Surf. Sci. 507 (2020) 145041]. *Applied Surface Science* 145784 (2020) doi:10.1016/j.apsusc.2020.145784.
  93. Cassie, A. B. D. & Baxter, S. Wettability of porous surfaces. *Transactions of the Faraday Society* **40**, 546–551 (1944).
  94. Cassie, A. B. D. Contact angles. *Discussions of the Faraday Society* **3**, 11–16 (1948).
  95. Milne, A. J. B. & Amirfazli, A. The Cassie equation: How it is meant to be used. *Advances in Colloid and Interface Science* **170**, 48–55 (2012).
  96. ProtScale Tool - References. <https://web.expasy.org/protscale/protscale-ref.html>.
  97. Giovambattista, N., Debenedetti, P. G. & Rossky, P. J. Hydration Behavior under Confinement by Nanoscale Surfaces with Patterned Hydrophobicity and Hydrophilicity. *The Journal of Physical Chemistry C* **111**, 1323–1332 (2007).
  98. Giovambattista, N., Rossky, P. J. & Debenedetti, P. G. Effect of Temperature on the Structure and Phase Behavior of Water Confined by Hydrophobic, Hydrophilic, and Heterogeneous Surfaces <sup>†</sup>. *The Journal of Physical Chemistry B* **113**, 13723–13734 (2009).
  99. Giovambattista, N., Lopez, C. F., Rossky, P. J. & Debenedetti, P. G. Hydrophobicity of protein surfaces: Separating geometry from chemistry. *Proceedings of the National Academy of Sciences* **105**, 2274–2279 (2008).
  100. Patel, A. J. *et al.* Sitting at the Edge: How Biomolecules use Hydrophobicity to Tune Their Interactions and Function. *The Journal of Physical Chemistry B* **116**, 2498–2503 (2012).
  101. Acharya, H., Vembanur, S., N. Jamadagni, S. & Garde, S. Mapping hydrophobicity at the nanoscale: Applications to heterogeneous surfaces and proteins. *Faraday Discussions* **146**, 353–365 (2010).



- 
102. Xi, E. *et al.* Hydrophobicity of proteins and nanostructured solutes is governed by topographical and chemical context. *PNAS* **114**, 13345–13350 (2017).
103. Wang, J., Bratko, D. & Luzar, A. Probing surface tension additivity on chemically heterogeneous surfaces by a molecular approach. *PNAS* **108**, 6374–6379 (2011).
104. Nguyen, C. T., Barisik, M. & Kim, B. Wetting of chemically heterogeneous striped surfaces: Molecular dynamics simulations. *AIP Advances* **8**, 065003 (2018).
105. Patel, A. J. & Garde, S. Efficient Method To Characterize the Context-Dependent Hydrophobicity of Proteins. *The Journal of Physical Chemistry B* **118**, 1564–1573 (2014).
106. Bradford, S. M., Fisher, E. A. & Meli, M.-V. Ligand Shell Composition-Dependent Effects on the Apparent Hydrophobicity and Film Behavior of Gold Nanoparticles at the Air–Water Interface. *Langmuir* **32**, 9790–9796 (2016).
107. Ling, X., Bonn, M., Parekh, S. H. & Domke, K. F. Nanoscale Distribution of Sulfonic Acid Groups Determines Structure and Binding of Water in Nafion Membranes. *Angew. Chem. Int. Ed.* **55**, 4011–4015 (2016).
108. Ma, C. D., Wang, C., Acevedo-Vélez, C., Gellman, S. H. & Abbott, N. L. Modulation of hydrophobic interactions by proximally immobilized ions. *Nature* **517**, 347–350 (2015).
109. Chen, S. *et al.* Subnanoscale hydrophobic modulation of salt bridges in aqueous media. *Science* **348**, (2015).
110. Isom, D. G., Castañeda, C. A. & Cannon, B. R. Large shifts in pKa values of lysine residues buried inside a protein. *Proceedings of the National Academy of Sciences* **108**, 5260–5265 (2011).
111. Luo, Z., Hou, J., Menin, L., Ong, Q. K. & Stellacci, F. Evolution of the Ligand Shell Morphology during Ligand Exchange Reactions on Gold Nanoparticles. *Angewandte Chemie International Edition* **56**, 13521–13525 (2017).
112. Liu, J. Z., van de Walle, A., Ghosh, G. & Asta, M. Structure, energetics, and mechanical stability of Fe–Cu bcc alloys from first-principles calculations. *Phys. Rev. B* **72**, 144109 (2005).

- 
113. Díaz-Ortiz, A., Dosch, H. & Drautz, R. Cluster expansions in multicomponent systems: precise expansions from noisy databases. *J. Phys.: Condens. Matter* **19**, 406206 (2007).
114. Luís, A. *et al.* Influence of Nanosegregation on the Surface Tension of Fluorinated Ionic Liquids. *Langmuir* **32**, 6130–6139 (2016).
115. Gannon, M. G. J. & Faber, T. E. The surface tension of nematic liquid crystals. *Philosophical Magazine A* **37**, 117–135 (1978).
116. Jańczuk, B., Wójcik, W. & Zdziennicka, A. Determination of the components of the surface tension of some liquids from interfacial liquid-liquid tension measurements. *Journal of Colloid And Interface Science* **157**, 384–393 (1993).
117. Sakamoto, K., Lochhead, R. Y., Maibach, H. I. & Yamashita, Y. *Cosmetic Science and Technology / ScienceDirect*. (Elsevier, 2017).
118. Myers, D. *Surfactant Science and Technology*. (John Wiley & Sons, Ltd, 2005). doi:10.1002/047174607X.
119. Kumar, V. S., Raja, C. & Jayakumar, C. A REVIEW ON SOLUBILITY ENHANCEMENT USING HYDROTROPIC PHENOMENA. *International Journal of Pharmacy and Pharmaceutical Sciences* **6**, 7.
120. Shimizu, S. & Matubayasi, N. The origin of cooperative solubilisation by hydrotropes. *Physical Chemistry Chemical Physics* **18**, 25621–25628 (2016).
121. Hopkins Hatzopoulos, M. *et al.* Are Hydrotropes Distinct from Surfactants? *Langmuir* **27**, 12346–12353 (2011).
122. Booth, J. J., Abbott, S. & Shimizu, S. Mechanism of Hydrophobic Drug Solubilization by Small Molecule Hydrotropes. *J. Phys. Chem. B* **116**, 14915–14921 (2012).
123. Eastoe, J., Hatzopoulos, M. H. & Dowding, P. J. Action of hydrotropes and alkyl-hydrotropes. *Soft Matter* **7**, 5917 (2011).
124. Shimizu, S. & Matubayasi, N. Hydrotropy: Monomer–Micelle Equilibrium and Minimum Hydrotrope Concentration. *J. Phys. Chem. B* **118**, 10515–10524 (2014).

- 
125. Lijnzaad, P., Berendsen, H. J. C. & Argos, P. Hydrophobic patches on the surfaces of protein structures. *Proteins: Structure, Function, and Bioinformatics* **25**, 389–397 (1996).
126. Dhapte, V. & Mehta, P. Advances in hydrotropic solutions: An updated review. *St. Petersburg Polytechnical University Journal: Physics and Mathematics* **1**, 424–435 (2015).
127. J. Booth, J., Omar, M., Abbott, S. & Shimizu, S. Hydrotrope accumulation around the drug: the driving force for solubilization and minimum hydrotrope concentration for nicotinamide and urea. *Physical Chemistry Chemical Physics* **17**, 8028–8037 (2015).
128. Fisher, M. T. Proline to the rescue. *PNAS* **103**, 13265–13266 (2006).
129. Patel, A. *et al.* ATP as a biological hydrotrope. *Science* **356**, 753–756 (2017).
130. Yaacobi, M. & Ben-Naim, A. Hydrophobic interaction in water-ethanol mixtures. *J Solution Chem* **2**, 425–443 (1973).
131. Rice, A. M. & Rosen, M. K. ATP controls the crowd. *Science* **356**, 701–702 (2017).
132. Brown, G. C. Total cell protein concentration as an evolutionary constraint on the metabolic control distribution in cells. *Journal of Theoretical Biology* **153**, 195–203 (1991).
133. Minton, A. P. The Influence of Macromolecular Crowding and Macromolecular Confinement on Biochemical Reactions in Physiological Media. *J. Biol. Chem.* **276**, 10577–10580 (2001).
134. Ellis, R. J. & Minton, A. P. Protein aggregation in crowded environments. *Biological Chemistry* **387**, 485–497 (2006).
135. Ellis, R. J. Macromolecular crowding: obvious but underappreciated. *Trends in Biochemical Sciences* **26**, 597–604 (2001).
136. Kotov, N. A. Inorganic Nanoparticles as Protein Mimics. *Science* **330**, 188–189 (2010).
137. Yang, Y., Serrano, L. A. & Guldin, S. A Versatile AuNP Synthetic Platform for Decoupled Control of Size and Surface Composition. *Langmuir* **34**, 6820–6826 (2018).
138. Chien, J. T. & Snyder, H. E. Detection and Control of Soymilk Astringency. *Journal of Food Science* **48**, 438–440 (1983).

139. Courregelongue, S., Schlich, P. & Noble, Ann. C. Using repeated ingestion to determine the effect of sweetness, viscosity and oiliness on temporal perception of soymilk astringency. *Food Quality and Preference* **10**, 273–279 (1999).
140. Schiffman, S. S. & Dackis, C. Taste of nutrients: Amino acids, vitamins, and fatty acids. *Perception & Psychophysics* **17**, 140–146 (1975).
141. Guven, Z. P. *et al.* Synthesis and Characterization of Amphiphilic Gold Nanoparticles. *JoVE (Journal of Visualized Experiments)* e58872 (2019) doi:10.3791/58872.



# List of publications

During my PhD I have been working on the following publications:

- Du H, Steinacher M, Borca C, Huthwelker T, Murello A, Stellacci F, Amstad E *Amorphous CaCO<sub>3</sub>: Influence of the Formation Time on Its Degree of Hydration and Stability*. Journal of the American Chemical Society **140**, 14289–14299 (2018).
- Luo Z\*, Murello A\*, Wilkins DM\*, Kovacik F, Kohlbrecher J, Radulescu A, Okur HI, Ong QK, Roke S, Ceriotti M, Stellacci F *Determination and evaluation of the nonadditivity in wetting of molecularly heterogeneous surfaces*. Proceedings of the National Academy of Science **116** (51), 25516-25523 (2019).
- Park W, Müller S, Baumann RP, Becker S, Hwang B, Murello A, Stellacci F *Corrigendum to “Surface energy characterization of nanoscale metal using quantitative nanomechanical characterization of atomic force microscopy” [Appl. Surf. Sci. 507 (2020) 145041]*. Applied Surface Science **512** 145784 (2020).

\* these authors contributed equally to this work

**Publications reported in bold are a direct result of this thesis.**

# Curriculum Vitae

## PERSONAL INFORMATION

Anna Murello

📍 Rte de la Maladière 16, 1022 Chavannes-près-Renens VD, CH

☎ +41 76 8238918 +39 334 9551839

✉ [anna.murello@epfl.ch](mailto:anna.murello@epfl.ch)

📅 Date of birth 13/03/1991

🇮🇹 Nationality Italian | 🇮🇹 Mother tongue Italian | 🌐 Other languages English (C1), French (C1)

## EDUCATION

- |           |   |
|-----------|---|
| 2015-now  | <p><b>PhD in materials science &amp; engineering</b></p> <p>Marie-Curie fellow (iSwitch ITN, grant agreement No. 642196)</p> <p>EPFL, Lausanne, CH</p> <ul style="list-style-type: none"><li>• Thesis title: "Water interactions with complex surfaces" (Supervisor: Francesco Stellacci)</li></ul>   |
| 2013-2015 | <p><b>Laurea magistrale in fisica (master degree in physics)</b></p> <p><b>curriculum: applied physics</b></p> <p>Alma Mater Studiorum Università degli studi di Bologna, IT</p> <ul style="list-style-type: none"><li>• Thesis title: "AFM force spectroscopy study of the conformational space and the aggregative processes of prion proteins" (Supervisors: Giampaolo Zuccheri and Bruno Samori)</li><li>• Final mark: 110/110 cum laude</li></ul>                  |
| 2010-2013 | <p><b>Laurea triennale in fisica (bachelor degree in physics)</b></p> <p>Università degli studi di Trieste, IT</p> <ul style="list-style-type: none"><li>• Thesis title: "Study of adhesion forces between living cells and nanostructured substrates" (Supervisor: Marco Lazzarino, TASC)</li><li>• Internship: "Scientific visualization of data through the software ParaView" (Supervisor: Edoardo Milotti, INFN)</li><li>• Final mark: 110/110 cum laude</li></ul> |
| 2005-2010 | <p><b>Maturità scientifica PNI (high school degree)</b></p> <p>Liceo scientifico Marinelli, ITIS Linussio, Codroipo, UD (IT)</p> <ul style="list-style-type: none"><li>• Final mark: 100/100 cum laude</li></ul>  |

- Publications**
- Raspadori A., Vignali V., Murello A., Giachin G., Samori B., Tanaka M., Bustamante C., Zuccheri G., Legname G. Single molecule AFM-force spectroscopy characterization of the conformational heterogeneity of the prion protein and its initial states of aggregation. *Submitted*.
  - Park W., Müller S., Baumann R.P., Becker S., Hwang B., Murello A., Stellacci F. (2020) Corrigendum to "Surface energy characterization of nanoscale metal using quantitative nanomechanical characterization of atomic force microscopy" [Appl. Surf. Sci. 507 (2020) 145041]. *Applied Surface Science* 512 145784.
  - Luo Z.\*, Murello A.\*, Wilkins, D. M.\*, Kovacic F., Kohlbrecher J., Radulescu A., Okur H. I., Ong Q. K., Roke S., Ceriotti M., Stellacci F. (2019) Determination and evaluation of the non-additivity of molecularly heterogeneous surfaces. *Proceeding of the National Academy of Science*, 116 (51), 25516-25523.
  - Du H. Steinacher M., Borca C., Huthwelker T., Murello A., Stellacci F., Amstad E. (2018) CaCO<sub>3</sub>: Influence of the Formation Time on Its Degree of Hydration and Stability. *Journal of the American Chemical Society*, 140 (43), 14289-14299.
  - Andolfi L., Murello A., Cassese D., Ban J., Dal Zilio S., Lazzarino M. (2017) High aspect ratio silicon nanowires control fibroblast adhesion and cytoskeleton organization. *Nanotechnology*, 28(15) 155102.
  - Murello A., Milotti E. (2014). Using a free software tool for the visualization of complicated electromagnetic fields. *European Journal of Physics*, 35(1), 015014.

\* equal contributions

- Poster presentations**
- Understanding proteins interactions. A. Murello, Z. Han, Z. Luo, F. Stellacci. EDMX Research Day. 29<sup>th</sup> November 2019. Lausanne, Switzerland.
  - Understanding proteins interactions. A. Murello, Z. Han, Z. Luo, F. Stellacci. Bioinspired Materials Conference. 20<sup>th</sup>-25<sup>th</sup> October 2019. Monte Verità, Switzerland.
  - Understanding and screening hydrophobic interactions. A. Murello, Z. Luo, Y. Ye, S. Guldin, F. Stellacci. Gordon Research Conference on Self-Assembly and Supramolecular Chemistry. 19<sup>th</sup>-24<sup>th</sup> May 2019. Les Diablerets, Switzerland.
  - Understanding and screening hydrophobic interactions. A. Murello, Z. Luo, Y. Ye, S. Guldin, F. Stellacci. Gordon Research Seminar on Self-Assembly and Supramolecular Chemistry. 18<sup>th</sup>-19<sup>th</sup> May 2019. Les Diablerets, Switzerland.
  - Wetting properties of heterogeneous surfaces at the nanoscale. A. Murello, Z. Luo, D. M. Wilkins, F. Kovacic, J. Kohlbrecher, A. Radulescu, H. I. Okur, Q. K. Ong, S. Roke, M. Ceriotti, F. Stellacci. Graduate School of Excellence Materials Science in Mainz (MAINZ) Summer School "Investigating Solid-Liquid Interfaces – Complementary Theoretical and Experimental Approaches". 11<sup>th</sup>-15<sup>th</sup> June 2018. Mainz, Germany.
  - *Interfacial energy of heterogeneous surfaces at the nanoscale*. A. Murello, Z. Luo, D. M. Wilkins, F. Kovacic, J. Kohlbrecher, A. Radulescu, N. Nianias, H. I. Okur, N. Smolentsev, Q. Ong, M. Ceriotti, S. Roke, F. Stellacci. EDMX Research Day 2017. 9<sup>th</sup> June 2017. Lausanne, Switzerland.
  - *Interfacial energy of heterogeneous surfaces at the nanoscale*. A. Murello, Z. Luo, N. Nianias, F. Kovacic, F. Stellacci. Summer School on Molecular Design and Synthesis. 13<sup>th</sup>-15<sup>th</sup> September 2016. Freiburg, Germany.
  - *Nanostructures strongly influence cell adhesion behavior*. A. Murello, L. Andolfi, D. Cassese, S. Dal Zilio, M. Lazzarino Winter Enrichment Program 18<sup>th</sup>-23<sup>th</sup> January 2014. KAUST, Saudi Arabia.
- Talks**
- Wetting properties of molecularly heterogeneous surfaces. A. Murello, Z. Luo, D. M. Wilkins, F. Kovacic, J. Kohlbrecher, A. Radulescu, H. I. Okur, Q. K. Ong, S. Roke, M. Ceriotti, F. Stellacci. 36<sup>th</sup> SAOG Meeting. 30<sup>st</sup> January 2020. Fribourg, Switzerland.
  - *Non-additive model for wetting of heterogeneous structures at the nanoscale*. A. Murello, Z. Luo, D. M. Wilkins, F. Kovacic, J. Kohlbrecher, A. Radulescu, H. I. Okur, Q. K. Ong, S. Roke, M. Ceriotti, F. Stellacci. Swiss Physical Society (SPS) Annual Meeting 2018. 28<sup>th</sup>-31<sup>st</sup> August 2018. Lausanne, Switzerland.
  - *Wetting Behaviour on Heterogeneous Surfaces at the Nanoscale*. A. Murello, Z. Luo, D. M. Wilkins, F. Kovacic, J. Kohlbrecher, A. Radulescu, N. Nianias, H. I. Okur, N. Smolentsev, Q. Ong, M. Ceriotti, S. Roke, F. Stellacci. 21<sup>st</sup> Edition of the Swiss Soft Days (SSD 21). 8<sup>th</sup> September 2017. Lausanne, Switzerland.



Teaching and  
outreach activities

- Teaching assistant for the bachelor course “Thermodynamics for materials science” at EPFL (2016, 2017 and 2018)
- Supervision of 3 bachelor students and 5 master students in the context of internships or semester projects (2016-2020)
- Facilitator at two “We Scientist 2035” workshops (7<sup>th</sup> February 2019 at the University of Lausanne and 16<sup>th</sup> July 2019 at EPFL)
- Responsible for outreach activities addressed to high school students on the EPFL campus and at high schools in Ticino (multiple times a year between 2016 and 2020)
- Tutor for disabled and dyslexic students at the University of Bologna (2014-2015)

Scholarships

- Merit-based scholarship given by the “Collegio universitario Luciano Fonda” for the bachelor degree in physics at the University of Trieste (three years).

